Modeling and Characterization of Phase Change Material Thermal Energy Storage for Electronics Cooling

by

Jack Prout

A thesis submitted in partial fulfillment of
the requirements for the degree of

Master of Science

(Mechanical Engineering)

at the

UNIVERSITY OF WISCONSIN-MADISON

2026

Date of final oral examination: April 30, 2026

The dissertation is approved by the following members of the Defense Committee:
Allison J. Mahvi, Assistant Professor, Mechanical Engineering
Michael J. Wagner, Assistant Professor, Mechanical Engineering
Greg F. Nellis, Professor, Mechanical Engineering

Dedicated to Mom and Dad

ACKNOWLEDGMENTS

I would like to thank my advising Professors Allison Mahvi and Mike Wagner. You both have been so helpful as teachers and mentors. I have learned a lot in the past two years and all of that has been supported by your knowledge and attention. It feels our weekly meetings got me through the degree at some points, so I am very grateful for the discussions we had. An additional thank you goes to Greg Nellis for being on my thesis defense committee along with Allison and Mike. There is a lot of information here, so I hope you find some of it interesting.

Thank you to everyone in the LET+S lab for their unwavering technical and moral support, especially as thoughtful reviewers of all the presentations I have given in the past two years. It has been great getting to share my work with you and learn about the interesting projects you are all working on. I would also like to thank all the students in the SEL for making a welcoming and talented environment that has continued to motivate me over the past two years.

I would also like to acknowledge the monetary support from the Office of Naval Research. I feel very fortunate for the time and resources I have had to work on this project.

ABSTRACT

Phase Change Materials (PCMs) are widely used in thermal energy storage (TES) devices due to their high energy density, but their performance is limited by thermal conductivity. Incorporating high conductivity material enhances the heat transfer ability at the cost of reduced storage capacity. This tradeoff is explored via three investigations of PCM heat sinks for electronics cooling applications. First, a parametric study of fin pitch and boundary condition was performed on a parallel fin test section to observe how these parameters impact PCM melting behavior. Experimental data was leveraged to compare three PCM melting models of increasing fidelities: the 1-D EMA, the 2-D Conduction, and the 2-D Convection. Results show that increasing heat flux and fin pitch lead to stronger convective currents, with velocities rising from near-zero at the 3-mm fin pitch to 4.5 mm/s at the 12-mm fin pitch. Conditions with strong natural convection also exhibited non-linear base temperature profiles, indicating shifts in the main heat transfer mechanisms. This was reflected in the model agreements, with the 1-D EMA model being reliable only at the 3-mm fin pitch, while the 2-D Convection model remained accurate throughout. The second study applied the Interfacial Filtering Structural Optimization (IFSO) method with a 2-D Conduction model to modify the 12-mm pitch fin geometry. The resulting geometry was then 3-D printed for testing. Experimental results of the optimized design yielded a 12.1% reduction in the maximum device temperature. Finally, the results from the two experimental studies were added to a literature survey to demonstrate PCM design principles through the lens of energy and power density maximization. The aspect ratio and device architecture were noted as critical design parameters, while the Ragone framework situated the parallel fin test section as a well-designed device compared to other studies.

TABLE OF CONTENTS

ACKNOWLEDGMENTS ii

ABSTRACT iii

TABLE OF CONTENTS iv

LIST OF TABLES vii

LIST OF FIGURES viii

LIST OF SYMBOLS AND ABBREVIATIONS xii

CHAPTER 1: INTRODUCTION 1

1.1 Evaluation of Modeling Methods for Finned PCM Composites 3

1.1.1 Strategies for conductivity enhancement 3

1.1.2 Heat transfer characterization 5

1.1.3 Significance 7

1.2 Topology Optimization and Additive Manufacturing of PCM Enclosures 8

1.2.1 Background 8

1.2.2 Significance 10

1.3 Capacity Versus Power Analysis 11

1.3.1 Trends in PCM heat sink literature 11

1.3.2 Ragone framework 12

1.3.3 Significance 13

1.4 Research Questions and Outline 14

CHAPTER 2: EXPERIMENTAL METHODS 15

2.1 Test Sections 15

2.1.1 Modular parallel fin test section (PFTS) 15

2.1.3 Metal foam test section (MFTS) 19

2.2 Experimental Facilities 20

2.2.1 Constant temperature flow loop 21

2.2.2 Constant heat flux setup 22

2.3 Instrumentation 23

2.3.1 Temperature 23

2.3.2 Image analysis of phase front 24

2.3.3 Particle Image Velocimetry (PIV) 26

CHAPTER 3: MODELING METHODS 30

3.1 1-D Conduction Model 30

3.2 2-D Conduction Model 32

3.3 2-D Convection Model 34

3.4 Heated Surface Boundary Condition 35

CHAPTER 4: PCM MELT DYNAMICS AND MODEL EVALUATION 38

4.1 Phase Front Dynamics 38

4.2 Characterization of Buoyancy Driven Phenomenon 41

4.3 Test Section Performance 46

4.4 Model Evaluation 50

4.5 Conclusions from Melt Dynamics and Modeling Work 56

CHAPTER 5: TOPOLOGY OPTIMIZATION 60

5.1 Optimized Design 60

5.2 Experimental Results 62

5.3 Conclusions from Topology Optimization 67

CHAPTER 6: ENERGY AND POWER CAPACITY ANALYSIS 68

6.1 Data Preparation 68

6.2 Evaluation of Present Work 69

6.3 Benchmarking Against Surveyed Literature 75

CHAPTER 7: CONCLUSION 83

REFERENCES 86

APPENDIX A: EMA M ODELING APPROACH 96

APPENDIX B: TRANSIENT BOUNDARY CONDITION ESTIMATION 98

CAPPENDIX C: CONTACT RESISTANCE ESTIMATION 100

APPENDIX D: DESCRIPTION OF UPPER BOUND ON 2-D MELTING 105

APPENDIX E: DESCRIPTION OF 3-D CIRCULATION PATTERNS 107

APPENDIX F: LOCAL EVALUATION OF THE 2-D CONVECTION MODEL 109

APPENDIX G: PARALLEL FIN TEST PROCEDURE 113

APPENDIX H: PIV DATA ANALYSIS AND RESULTS 122

LIST OF TABLES

Table 1: Material properties of the working PCM, HCM, and walls.. 16

Table 2: ERG Aerospace metal foam properties.. 19

Table 3: PCM settling time (min) and liquid fraction (%) when discharged with a constant heat flux boundary condition.. 48

Table 4: Model to experiment base temperature error at the melt time. 50

Table 5: Summary of model computational time, limiting flaws, and recommended use cases. Note that the compute time was recorded for the 12-mm 120-W case................. 58

Table 6: List of literature gathered for Ragone analysis 77

Table 7: Heater Capacity Validation at the 3-mm fin pitch.. 98

Table 8: Discharge times after fitting a fin contact resistance to the 3-mm fin pitch tests........ 100

LIST OF FIGURES

Figure 1: Temperature rise versus heat input for representative heat sinks. PCM TES devices start fully frozen, or in the “charged” state. 1

Figure 2: A Ragone plot shows the relation between power and energy density for an energy storage technology [67]... 13

Figure 3: Images of the parallel fin test section (PFTS) configured to the **(a)** 12-mm fin pitch and **(b)** 3-mm fin pitch. 16

Figure 4: Global domain and unit cell of the optimization problem. 17

Figure 5: Plastic 3D printed IFSO designs from **(a)** TKDS, **(b)** TPMS, and **(c)** PF seeds. 18

Figure 6: IFSO Test Section fabricated with metal additive manufacturing. 19

Figure 7: Metal foam test section composed of two Duocell metal foam block and a similar PCM containment method. 20

Figure 8: Constant temperature flow loop **(a)** diagram and **(b)** close-up image of thermal plate (gray) with the TOTS and insulation box. 21

Figure 9: A diagram **(a)** and photo **(b)** of the constant heat flux experimental setup................. 23

Figure 10: Thermocouple instrumentation placements shown via **(a)** a dimensioned diagram and **(b)** an image for the 12 mm PFTS configuration... 24

Figure 11: Liquid fraction image processing approach for the 9-mm fin pitch test section showing the progression from **(a)** raw to **(b)** binarized and finally **(c)** masked images. 25

Figure 12: Image analysis setup with PIV camera in position.. 27

Figure 13: Experimental boundary condition transience for **(a)** constant temperature and **(b)** constant heat flux boundary conditions 36

Figure 14: Images of the melting process at $F_{liquid} = 0.55 \pm 0.02$ with key dimension labels at **(a)** 3 mm, **(b)** 6 mm, **(c)** 9 mm, and **(d)** 12 mm fin pitches. 39

Figure 15: Melting dynamics descried with **(a)** deviation from 1-D melting across all boundary conditions, bounded by ideal cases, and **(b)** images of the 12-mm PCM phase front before and during the transition to 1-D melting (device melted with 35 ºC base temperature). The melt height vs. time for the **(c)** 6-mm and **(d)** 12 mm-fin pitches is also shown when the test sections are melted with a 35 ºC base temperature. 40

Figure 16: Local velocity measurements compared between **(a)** 6-mm and **(b)** 12-mm fin pitches at four stages in the melting process with a 45 ºC boundary condition. Streamlines are indicated in white with color-coded fluid velocity. 42

Figure 17: Local temperature distributions compared between **(a)** 6-mm and **(b)** 12-mm fin pitches at four stages in the melting process at a 45 °C boundary condition........ 43

Figure 18: Maximum measured PCM velocity vs liquid fraction with aluminum fins spaced 6-12 mm apart. The results are shown for two types of boundary conditions: a range of constant base temperatures (top panel) and a range of constant heat fluxes (bottom panel). Error bars indicate a 95% confidence interval for the maximum velocity observed at each liquid fraction. 45

Figure 19: Base plate temperature vs time for constant heat flux tests. Results show increasingly non-linear profiles at higher fin pitches. Asterisks mark when the PCM has fully melted.. 46

Figure 20: PCM melt times for tests discharged at a constant temperature boundary condition with volume fractions of PCM listed for each pitch. 49

Figure 21: Base temperature comparisons between the three developed models and the experimental results at four operating conditions that represent a broad range of melting mechanisms. Hollow dots designate the visually observed detachment time; solid dots designate the fully melted time. 51

Figure 22: Base temperature model error and model discharge rates for constant heat flux tests mapped over the experimental campaign. Colors of the large dots indicate the 2-D convection model error while the colors of the small dots indicate the 1-D EMA model error. 54

Figure 23: Constant temperature discharge-time error for the 1-D EMA and 2-D convection models with respect to the Rayleigh Number (Ra). Model uncertainty is calculated with respect to the camera interframe rate. 55

Figure 24: Design evolution **(a)** and **(b)**, performance **(c)** and **(d)**, and local fields **(e)** of the IFSO optimization using a 3-D conduction-based model.................................... 61

Figure 25: Snapshots of the experimental melting process for (a-d) PFTS, and (e-h) TOTS. 63

Figure 26: Experimental performance comparison of (a) base temperature and (b) liquid fraction between the IFSO and PF designs. 64

Figure 27: Temperature and SOC response of PFTS and MFTS at 40 and 80 W. 70

Figure 28: Device utility plot for the PFTS and MFTS devices. It denotes the maximum latent capacity with the bar height, and the achieved storage fraction as a function of

power and cutoff temperature with the contour plot inside of the bar. X-marks in the metal foam bar indicate conditions that were not tested but where the storage fraction is inferred. 71

Figure 29: Ragone plot of the PFTS, MFTS, and IFSO device evaluated at a cutoff temperature 18 ºC above the melting temperature (36 ºC for hexadecane). 73

Figure 30: Ragone plot of in-house devices evaluated at a cutoff temperature 10 ºC above the melting temperature (28 ºC). 74

Figure 31: Data collection and manipulation from the study Temel et al (2023) [75]. Plots (a) and (b) show plots of liquid fraction and base temperature directly from the paper. Plot (c) shows base temperature and liquid fraction data refitted into a modified temperature response plot. 76

Figure 32: Data collection and manipulation from the study Fu et al (2021) [59]. Plots **(a)** and **(b)** show plots of melt speed and base temperature directly from the paper. Plot **(c)** shows base temperature and liquid fraction data refitted into a modified temperature response plot. 76

Figure 33: Specific energy density against specific power density, normalized by ΔH, for a selection of finned PCM heat sinks. 78

Figure 34: The PFTS benchmarked against available metal foam and CCM papers. The marker color is scaled by the device aspect ratio, defined as device width divided by its height. 79

Figure 35: Device utility plot of the 3-mm PFTS alongside other devices from literature. Note that each bar has a unique heat flux range. 81

Figure 36: Effective enthalpy versus temperature relationship for the 3 mm and 12 mm fin pitch, bounded by the pure material profiles. 97

Figure 37: Base temperature profiles after applying the fitted heater capacity for two 12-mm and two 3-mm tests. 99

Figure 38: Base temperature profiles after applying the fitted contact resistances to the convection model. 101

Figure 39: Experimental setup of the fin contact resistance measurement. (a) shows a closeup of the thermocouple positions and the heater-fin system. (b) shows the power supply and fan. 102

Figure 40: Curve fitting to characterize fin performance with experimentally measured temperature distributions. 104

Figure 41: Estimated contact resistance from the single-fin experiment at four heat input rates. 104

Figure 42: Illustration of the upper bound in 2-D melt dynamics. 106

Figure 43: Local comparison of PCM composite temperatures between the experiment and the 2-D convection model. THe bottom row corresponds to thermocouples 13 mm from the base-PCM interface. 110

Figure 44: Local phase front at four instances in the time compared between the experiment and the 2-D convection model (shown in green). 112

Figure 45: Imaging rate, proxied by average particle motion, for a set of image frames taken with the Basler Pylon software. **(a)** shows a histogram of the number of frames grouped by mean velocity. **(b)** shows a frame-by-frame history of the calculated mean velocity 123

Figure 46: Frame rate between images for a group of 60 images taken with the parallel-processed python script. 124

Figure 47: Image Selection and Import 125

Figure 48: Selecting a region of interest using the example of the 12 mm 120 W test. 126

Figure 49: Image masking to occlude the solid PCM from PIV analysis. 127

Figure 50: Select PIV analysis settings and preview the analysis on the current frame. 128

Figure 51: Calibrate the velocity vectors using an image taken for the specified test. 129

Figure 52: Local velocity estimates taken with PIV. Note the changing scale in the color bar. 149

LIST OF SYMBOLS AND ABBREVIATIONS

Abbreviations

TES	Thermal Energy Storage
PCM	Phase Change Material
HCM	High Conductivity Material
EMA	Effective Medium Approximation
TO	Topology Optimization
IFSO	Interface Filtering Structural Optimization
FoM	Figure of Merit
CCM	Close Contact Melting
PFTS	Parallel Fin Test Section
PF	Parallel Fin
MF	Metal Foam
TOTS	Topology Optimized Test Section
TKDS	tetralkaidecahedron
TPMS	Triply Periodic Minimal Surface
MFTS	Metal Foam Test Section
PIV	Particle Image Velocimetry
LED	Light Emitting Diode
FFT	Fast Fourier Transform
AR	Aspect Ratio
CFD	Computational Fluid Dynamics
SOC	State of Charge

Symbols

T	Temperature [ºC]
K	Conductivity [W/m-K]
C	Heat Capacity [J/K]
C	Specific Heat Capacity [J/kg-K]
F	Liquid Fraction [-]
ΔH	Latent Heat of Fusion [J/kg]
St	Stokes Number [-]
t	Time [s]
U_o	Characteristic Velocity [m/s]
d_p	Particle Diameter [m]
Re	Reynolds Number [-]
w	Width [m]
th_f	Fin Thickness [m]
P_f	Fin Pitch [m]
i	Iteration variable 1 [-]
j	Iteration variable 2 [-]
x	Distance (first direction) [m]
y	Distance (second direction [m]
$\boldsymbol{n}$	Normal Vector [-]
$\boldsymbol{u}$	Fluid Velocity Vector [m/s]
$\boldsymbol{g}$	Gravity Vector [m/s^2]

p	Pressure [N/m]
A_m	Mushy Zone Constant [-]
$\dot{q}$``	Incident Heat Flux [W/m^2]
Co	Courant Number [-]
$\dot{P}_e$	Electrical Power Supply [W]
m	Mass [kg]
L	Length of Solid PCM [m]
N	Number of (nodes, measurements…) [-]
Ra	Rayleigh Number [-]

Greek Symbols

ρ	Density [kg/m^3]
Φ	Volume Fraction [-]
Δ	Change in
Ω	Computational Region
Γ	Region Interface
∇	Divergence
β	Coefficient of Thermal Expansion [1/K]
ε	Small value to avoid division by zero
δ	Difference from 1-D melting behavior
υ	Viscosity [Pa-s]
α	Thermal Diffusivity [m^2/s]
η	Fin efficiency [-]

Subscripts

max	Maximum allowable with regards to base temperature
Melt	Melt temperature
ts	Test Section
Solid	Solid PCM
Liquid	Liquid PCM
p	Particle
o	Relaxation (Time)
PCM	Phase Change Material
HCM	High Conductivity Material
eff	Effective (Medium)
b	Base
s	Solidus
l	Liquidus
c	PCM to HCM Interface
ref	Reference value
h	Heater
ch	Channel
1D	1-Dimensional
n	Normalized
final	Final base temperature
PF	Parallel Fin Improvement
IFSO	Interface-Filtering Structural Optimization Improvement

CHAPTER 1: INTRODUCTION

Thermal energy storage (TES) has emerged as a valuable technology for managing transient thermal loads in a variety of applications, including shifting electricity generation and usage for building HVAC equipment [1, 2] and regulating temperature in transient electronic systems [3]. Temperature regulation is increasingly important with the downscaling of electronics components seen in next generation electric vehicles, data centers, and personal devices. Thermal storage relies on energy-dense materials capable of storing and releasing large amounts of heat. Phase change materials (PCMs), which store latent energy through the melting and freezing process, are a popular option for TES heat sink devices because they can store thermal energy at a nearly constant temperature. The temperature at which it melts/freezes can be manipulated by material engineering, making PCM storage adaptable to a variety of design requirements. The TES process is shown in Fig. 1 as a qualitative plot of temperature as a function of heat stored between latent and sensible materials.

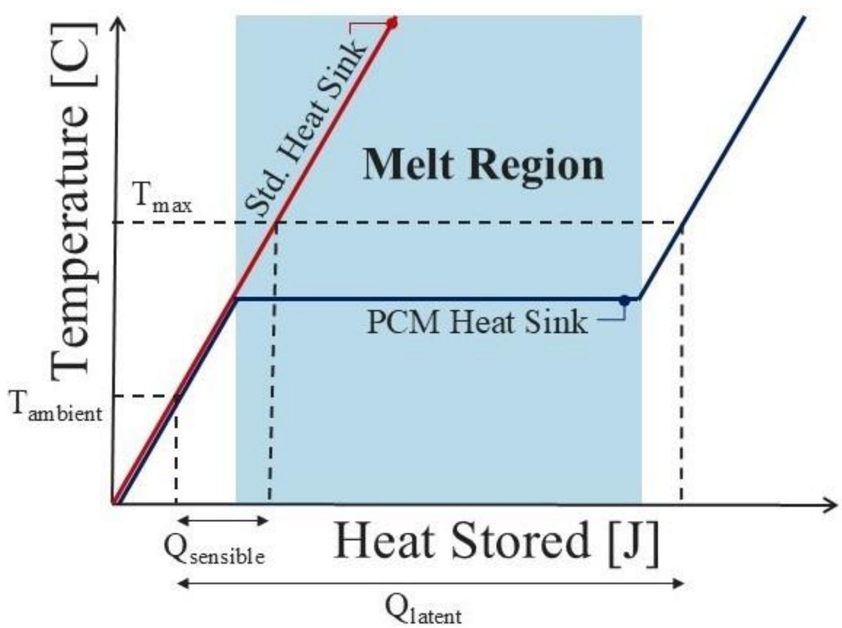

Figure 1: Temperature rise versus heat input for representative heat sinks. PCM TES devices start fully frozen, or in the "charged" state.

Fig. 1 demonstrates that PCMs have significantly higher storage capacities than sensible storage materials when a device must remain below some cutoff temperature (T_{max}). Consequently, organic PCM heat sinks have been integrated into defense, aerospace, and building technologies [4]. However, one major limitation of PCMs is their low thermal conductivity. This slows the rate of device charging and discharging, making it difficult to dissipate large amounts of heat quickly. A major focus of current research involves designing PCM devices with conductivity enhancers to eliminate this shortcoming. However, methods to do so, such as including high conductivity materials (HCMs), come at the cost of reduced energy storage capacity.

The tradeoff between thermal conductivity and storage capacity is a central concern for PCM heat sink research and design. It is also a complex relationship dependent on multiple physical mechanisms that are difficult to neatly represent. Furthermore, the aspects of this relationship change with device size, timescale, and heat sink design, making a universal solution intractable.

Instead, there are multiple pathways to address the conductivity (or power) versus energy capacity tradeoff through modeling and design methods. This work addresses three of those pathways. The first is understanding PCM melt dynamics and its impact on modeling accuracy. This can inform model selections so that the most efficient model is applied to a design problem. However, models with high computational speeds may only be reliable under certain melting conditions, so a part of building efficient models is outlining when and how they become inaccurate. With this knowledge, fast and reliable models can be deployed to parameterize PCM heat sink problems that solve for the correct balance of thermal conductivity and storage capacity.

The second is generating topology optimization (TO) methods so that computer algorithms can automatically address the tradeoff through preset objectives. For this method, formulating the optimization problem and objective are critical steps in designing for optimal energy capacity and power. Capturing the necessary heat transfer mechanisms in the optimizer model is also vital to generating a useful design.

The third is reframing existing PCM heat sink research into a capacity versus power narrative. This method contextualizes disparate devices into a framework that allows comparisons across device architectures, sizes, and timescales. In addition, this framework enables case studies that inform good PCM heat sink design principles while adding clarity to PCM TES research writ large.

Each of these approaches will be applied to a general PCM melting problem without a specific use-case in mind. The three pathways will be addressed separately in this thesis, although they all leverage the same experimental and numerical methods for data collection. A deeper description of the motivations and goals for each approach is presented in the following sections.

1.1 Evaluation of Modeling Methods for Finned PCM Composites

The first pathway aims to improve understanding of PCM melting mechanisms in common PCM heat sink architectures through experimental observations, then use that understanding to inform when higher order models can be used. The work described in this section and in Chapters 2, 3 and 4 has been submitted for publication in the Journal of Energy Conversion and Management.

1.1.1 Strategies for conductivity enhancement

To address the low conductivity of PCMs, high conductivity materials (HCMs) are frequently added to PCM enclosures that increase the rate of heat transfer. HCMs improve the effective thermal conductivity of the phase change composite, but reduce the PCM volume, and therefore storage capacity. HCMs have been added to PCMs in many forms with the goal of maximizing the heat transfer enhancement while balancing the storage capacity. Using HCMs also keeps the device completely passive, meaning the device requires no external power or signals. Commonly studied HCMs include conductive nanoparticles [5], compressed expanded graphite [6-9] metal foams [10], and metal fins [11, 12].

Carbon or metal nanoparticles are dispersive additives that can be used on their own or with metal foams or fins. While nanoparticle infusion increases the PCM effective conductivity, agglomeration over frequent cycling has been observed to diminish its enhancement capabilities [13]. Foams and solid finned structures show a more favorable tradeoff between conductivity and capacity than nanoparticles with little observed degradation [14, 15]. Hybrid deployment of nanoparticles in fins can be less effective than fins alone in cases where natural convection is prominent [16]. This does not mean nanoparticles are always ineffective, but macroscopic structures appear to have better enhancement effects than nanoparticles.

These findings encourage the use of graphite or metal structures in PCM composites. Although porous HCM materials such as compressed expanded graphite and metal foams are promising additives, there are still manufacturing, degradation and cost barriers that need to be resolved before they are widely adopted [17-20]. Literature on the comparison between metal foams and fins has not reached a consensus on which HCM structures are more effective [17, 21-23]. For example, some results indicate metal fins can reduce melting time by 68.4% compared to copper foam [24], but others show that metal fins using 26% more volume have a 69% longer melt time than metal foams [25]. This suggests that the relative worths of these enhancement structures are case dependent. Unless metal foams are shown to consistently outperform fins in a variety of use conditions, the economic and manufacturing benefits of metal fins currently make it a strong option for commercial applications.

The advantages of finned TES devices have prompted research into fin configurations and geometries to optimize the heat transfer rate and storage capacity for different applications. Cylindrical or annular PCM containers are most commonly studied for heat exchange with a heat transfer fluid [12], while rectangular enclosures are the most practical for electronics cooling applications [26]. Regardless of container type, the most common research approach is to vary multiple geometric parameters and determine the optimal fin configuration for a given boundary condition.

In electronics cooling, the fin spacing, orientation, and shape are the most investigated parameters. Safari et al. shows that a rectangular container with vertical planar fins reduces the discharge time by up to 92% compared to an empty PCM bath [26], and that parallel fins can outperform pin-fin and perforated-fin HCMs in horizontal and vertical orientations. Similar studies on planar fin PCM composites have found that parameters that increase surface area, such as fin height and number of fins, improve the effective thermal conductivity considerably, while fin thickness had nearly no influence [27, 28].

1.1.2 Heat transfer characterization

These and other studies give insight into the key heat transfer processes in HCM/PCM composites. Conduction is the main mode of heat transfer during early-stage melting when solid PCM is near HCM structures. As more PCM melts and the space that liquid PCM occupies grows, temperature gradients can arise within the liquid PCM, inducing density-driven natural convection [27, 29]. The effect of natural convection is highly dependent on HCM volume fraction and container geometry, where higher HCM volumes that obstruct fluid streamlines will diminish natural convection [28, 30]. This is most succinctly conveyed by Safari et al., who showed that the natural convection heat transfer is inversely proportional to the number of fins in a PCM composite

[27]. The presence of natural convection is also dependent on the heating load applied to the device, where higher heat fluxes drive larger temperature differences in the liquid PCM [31, 32]. Together, these studies highlight the importance of natural convection in finned PCM composites and identify the key design parameters that influence its intensity. However, a refined relation between fin pitch and natural convection enhancement, and an explanation of the driving factors, remains unclear for experimentally tested enclosures.

Several heat transfer models have been developed to predict TES performance, building on experimental observations across various device configurations. The simplest models assume conduction is the dominant heat transfer mechanism and treat the PCM composite as a homogeneous material with properties equal to the volume-weighted average of the PCM and HCM [33]. These effective medium approximation (EMA) models generally work well when the HCM and PCM are in close proximity, either when fin pitches are very small or the PCM is impregnated into a metal or graphite foam [13, 33]. Their main advantage is computational speed, making them amenable to parametric design and optimization problems [34-37].

The EMA assumptions typically break down when the HCM material is more physically separated within the device (greater than 2 mm spacing according to [38]). Although there have been some limited attempts to add corrections to EMA models to account for non-homogeneous properties [39] and natural convection [39, 40], these corrections are generally geometry-specific and not broadly applicable across possible configurations. Alternatively two-dimensional conduction models that consider the HCM and PCM properties separately [14] and computational fluid mechanics models that consider natural convection in the liquid PCM [41-43] are often leveraged to better predict performance. Although potentially more accurate, these models are much more computationally expensive, making them ill-suited for design optimization or evaluating complex boundary conditions over long time scales. To our knowledge, current literature has not experimentally investigated how fin spacing governs the transition from conduction-dominated to convection-dominated melting over a comprehensive set of testing conditions, and how that transition impacts the utility of different fidelity modeling methods. Furthering the understanding of lamellar PCM composite melting through experimental and numerical comparison should inform what mechanisms are important for a given design, and thus what modeling method is most appropriate to use.

1.1.3 Significance

This work addresses a gap in literature by experimentally and computationally investigating the conditions under which non-homogeneous material properties and convection effects begin to influence the melting behavior of composite PCM materials. Specifically, we examine a common representative case: a rectangular container filled with straight HCM fins and PCM, uniformly heated from the bottom. Our experiments reveal that non-homogeneous properties lead to predictable 2-D melting behavior, where the higher-thermal-conductivity HCM causes the PCM to melt away from the fins rather than solely away from the bottom surface. Simultaneously, we quantify the liquid PCM velocity profiles which inform the relative importance of natural convection effects.

The experimental results are compared to 1-D conduction-based, 2-D conduction-based, and 2-D convection-based models. The comparisons offer insight into the conditions under which each modeling simplification is justified. They also illustrate the relative importance of different heat transfer mechanisms across a breadth of boundary conditions. Our goal is to evaluate the predictive accuracy of models with different levels of fidelity so that future researchers can select the appropriate model for more detailed optimization and design work or consider design strategies that leverage prevailing heat transfer mechanisms.

1.2 Topology Optimization and Additive Manufacturing of PCM Enclosures

The second pathway experimentally tests topology optimized PCM composite heat sinks to demonstrate their effectiveness in improving device performance. It also discusses how the inclusion of buoyancy driven physics changes the optimization results, and what that reveals about the impact of natural convection on the power versus energy capacity tradeoff. The work described in this section and in Chapter 4 are included in a paper submitted for publication in the Journal of Energy Storage. Tianye Wang developed the model and optimization approach and we collaborated on the optimization objective function. I fabricated the physical device and performed all experimental validation and data analysis on the optimized design.

1.2.1 Background

Investigations into parallel fin PCM composites have found that increasing the surface area can significantly enhance heat transfer [28, 29]. These findings motivated work with high-surface-area fractal fins, which can outperform rectangular fins with the same amount of HCM volume [44-47].

High surface area fractal structures can be designed using algorithmic optimization. At a high level, these programs are given an initial condition and some optimization objective, called the objective function. The model then repeatedly solves the PCM composite melting problem with small perturbations to the HCM structure. The sensitivity of the objective function is calculated with respect to each perturbation, which then informs the algorithm where HCM should be placed in future iterations. This process continues until adding or subtracting HCM fails to substantially improve the optimization objective. At this point, the optimization method has converged, and a final design is achieved.

Two optimization methods are investigated throughout this project: standard Topology Optimization, and Interface-Filtering Structural Optimization (IFSO). Standard TO uses a density-based approach to change the relative amount of PCM or HCM in every node across the entire domain. It has been used repeatedly across many different domains, including PCM composite structures [48-51]. TO uses a driving function to sharpen the relative density to be either fully PCM or HCM over successive iterations until it has converged.

While TO starts with a uniform PCM density field, the IFSO method starts with an initial seed, such as a parallel fin HCM geometry in a PCM enclosure. This initial seed allows for IFSO to only perturb the density field along the PCM/HCM interface. Because of this, IFSO converges faster than TO but requires more user input.

Both IFSO and TO are valuable methods for achieving optimal PCM composite design. And in the case of TO, numerous studies have demonstrated that the method can enhance PCM heat sink performance [48-51]. However, these studies and others like them typically assume that PCM melting is conduction-dominated and consequently ignore natural convection in their numerical physics solvers.

To our knowledge, the current PCM optimization literature lacks discussion of the importance of natural convection in two major ways. First, as discussed in Section 1.1.2, natural convection can have a large impact on heat transport for widely spaced PCM volumes. This means that conduction-based optimizers ignore a potentially important heat transfer mechanism, which can lead to sub-optimal results. Experimental verification can alleviate these concerns by comparing the actual heat sink performance to the model predictions to confirm that the dominant heat transfer mechanisms have been captured, but this step is often skipped in computational optimization studies.

Second, natural convection can be leveraged as a mechanism to increase heat transfer without reducing device capacity. Rather than being a source of error, natural convection may improve optimization effectiveness if the numerical solvers include buoyancy driven flow in the governing equations. This can be tested by comparing a conduction-based and a convection-based optimization results for the same operating conditions, but it also requires experimental testing to validate the results.

1.2.2 Significance

This work provides experimental validation of topology optimized designs to evaluate the effectiveness of the IFSO method under conditions where natural convection is prevalent. This work addresses a gap in literature by applying a novel optimization method to a multi-mechanistic heat transfer problem. Experimental testing of the emergent design opens a discussion on the value of considering natural convection when optimizing thermal storage devices.

A unit-cell based parallel fin design seed was used to initialize the IFSO method with an isoflux boundary condition applied to the device base. The IFSO design was manufactured using Direct Metal Laser Sintering, so additional constraints were added to the IFSO method for printability. The specified design problem was compared to an existing parallel fin device in a compatible experimental facility. Our tests verify that a significant performance improvement predicted by the model is matched experimentally. Additionally, these tests demonstrate the importance of natural convection on the testing results. This work motivates future exploration of convection-based PCM TES optimization, while also signaling that a conduction-based approach may perform similarly to convection-based optimizations at a fraction of the computational time.

1.3 Capacity Versus Power Analysis

The third pathway towards improving PCM-based TES design involves observing device performance from a device-level perspective to enable comparisons across PCMs, HCMs, and other device characteristics. It leverages a literature review to highlight common trends in PCM heat sink design while also providing useful tools for visualizing performance.

1.3.1 Trends in PCM heat sink literature

Researchers have tested performance for many HCMs, including parallel, perforated, and pin fins, metal foams, and lattice structures [52-57]. Despite the quantity of work that has been completed in this effort, it is still unclear from literature whether certain HCM forms are superior to others. This is in large part due to the variability in testing conditions and procedures, reported data, and device constructions that make comparisons between studies difficult. The most common figures of merit (FoMs) are melt fraction versus time and base temperature versus time. These are great for observing differences across a narrow set of design changes, but these FoMs lack the context to compare across different devices. For example, it is difficult to compare two different test sections using those FoMs if they were tested at different powers or with different PCMs. Put plainly, the number of parameters that change across studies makes it difficult to determine if an individual PCM device is “good” or “bad” for a given application. From this, one can observe how individual investigations into a narrow set of geometries may ignore the complexity of the design problem and ultimately yield little useful information.

A similar concern persists when investigating the amount of HCM to be added to a PCM device. For a device with a fixed volume, the amount of HCM added must be compensated by removing PCM, thereby reducing the device energy capacity. However, if not enough HCM is added, heat dissipation will be too slow and large temperature gradients will cause high surface temperatures. This manifestation of the power versus energy capacity tradeoff is frequently overlooked in discussion about HCM form and quantity [58].

Another common strategy to increase power capacity for PCM heat sinks is to use close contact melting (CCM) [59-62]. This method maintains a consistent melt layer thickness between the solid PCM and the heated surface through gravitational or applied pressure. CCM is a recent introduction to PCM heat sink design, but it struggles with the same restrictions as HCM devices. Adding more mass presses the solid PCM closer to the heated surface, improving temperature control at the cost of additional height and weight to the system. This additional height represents available volume that could be used for storing PCM and increasing the device capacity. CCM devices are a good example of how the energy-power tradeoff extends to all PCM design. Furthermore, it motivates a more systematic analysis of this tradeoff that can include disparate heat sink architectures in a unified framework.

1.3.2 Ragone framework

To have a more systematic approach, it is important to clearly define the design problem. In essence, every PCM heat sink must withstand some specified heat load while maintaining a temperature below some cutoff value. Once the device temperature is above this cutoff value, the PCM heat sink is no longer providing useful energy storage. With these constraints, designers may try to optimize around other parameters. For instance, the device volume might be fixed, so the designer maximizes the total energy capacity (to increase operational time). Conversely, the operational time might be fixed, allowing for a design around minimizing the device footprint. This can be generalized by setting the goal of maximizing both energy density and power density for a given cutoff temperature. This formulation explicitly acknowledges the energy-power tradeoff via its two-dimensional figure of merit, while also simplifying the design constraints to a temperature cutoff and a power requirement.

Energy density versus power density is not a new concept for energy storage devices, with its inception and extensive use coming from electrochemical battery research. The Ragone plot, shown in Fig. 2, is the most common format for visualizing this design problem. It has received recent attention for PCM applications because of the parallels between electrochemical and phase change energy storage [63-65]. Despite its growing value in PCM research, it has not yet been used to review PCM heat sink technologies or provide comparisons across different enhancement methods. Instead, it has been limited to material research or singular device level investigations [34-36, 63, 66].

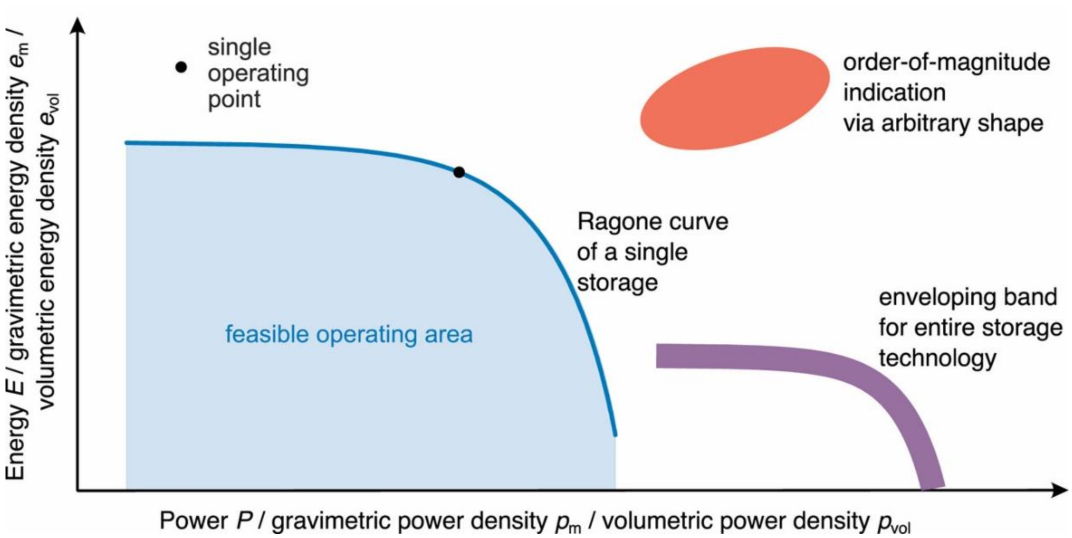

Figure 2: A Ragone plot shows the relation between power and energy density for an energy storage technology [67].

1.3.3 Significance

The current lack of a comprehensive design framework for PCM heat sinks motivated a larger-scale literature comparison of energy and power densities between devices. The goal is to provide insight into appropriate geometries and designs under specific operating conditions. The

Ragone framework also highlights the necessity of clear design objectives for effectively sizing PCM devices. In that respect, this work demonstrates how high-level device evaluations can be expanded to other HCM structures and architectures while maintaining a consistent basis for comparison. This analysis aims to motivate the adoption of the Ragone framework for future studies that wish to contextualize their work in terms that can be applied to a broad set of potential PCM heat sink solutions.

1.4 Research Questions and Outline

This thesis investigates three main questions for PCM TES design: (1) how does melting behavior change for PCM composites of varying fin spacing and heat input, and how do different melting mechanics impact modeling accuracy; (2) how can topology optimization be used to improve device performance, and (3) what does the Ragone framework reveal about PCM design trends, and how can it be used for expansive PCM analysis.

Chapter 2 discusses the test sections and experimental methods used for various tests. Chapter 3 outlines the three numerical models that were used during investigations on melting dynamics and topology optimization. Chapter 4 focuses on results from experiments on melting behavior and numerical modeling accuracy. Chapter 5 discusses the performance of topology optimized designs, including the experimental validation of a TO device. Chapter **Error! Reference source not found.** focuses on a device-level analysis that compares the in-house test sections against other devices in literature using the Ragone framework. Finally, the thesis is concluded in Chapter 7, with references and supplemental appendices attached to the end.

CHAPTER 2: EXPERIMENTAL METHODS

This work investigates the melting behavior of PCM composite heat sinks under various thermal boundary conditions. The following section describes the experimental setup, including the procedures for applying constant heat flux and constant temperature boundary conditions. It also details the measurement techniques used to characterize PCM melting dynamics, TO evaluation, and metal foam testing.

2.1 Test Sections

Three test sections were designed and manufactured to investigate the questions outlined in Section 1.4. These include the parallel fin, topology optimized, and metal foam test section.

2.1.1 Modular parallel fin test section (PFTS)

A configurable test section was developed to evaluate the performance of straight lamellar fins submerged in a rectangular PCM bath. The test section, shown in Fig. 3, was designed to accommodate a varying number of 1-mm thick fins spaced 3, 6, 9, and 12 mm apart, corresponding to PCM volume fractions of 65.7, 82.9, 88.5, and 91.3%, respectively. These spacings were selected to explore the impact of natural convection in PCM composites with different characteristic length scales. All fins extended beyond the PCM fill height, following evidence from prior studies that longer fins improve heat transfer performance [29].

Fins are inserted by pressing 1-mm thick 6061 aluminum plates into milled slots at the base of the test section. To ensure vertical alignment and minimize thermal contact resistance, two combs were fastened into the test section to apply a downward force on the fins during testing. Each comb contains regularly spaced Buna N O-rings, which thermally insulate the comb from the rest of the assembly and help maintain consistent fin positioning.

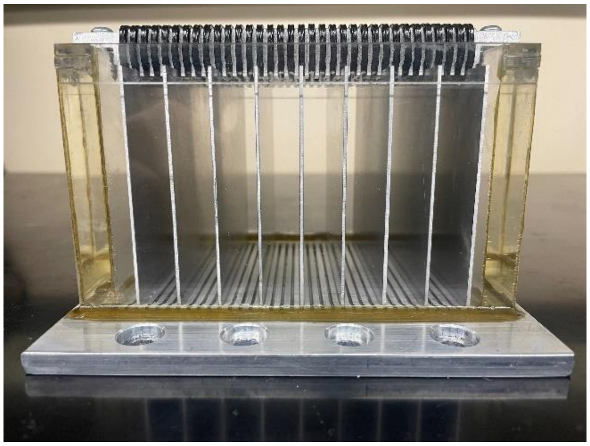

(a) 12-mm fin pitch

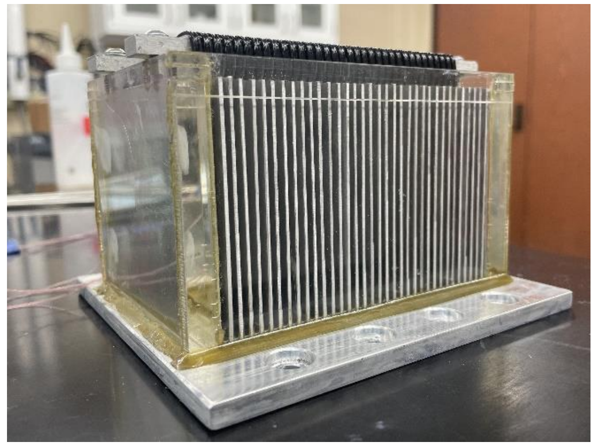

(b) 3-mm fin pitch

Figure 3: Images of the parallel fin test section (PFTS) configured to the **(a)** 12-mm fin pitch and **(b)** 3-mm fin pitch.

The PCM for these experiments was hexadecane, which filled the remainder of the container to the fill line (10.6 cm × 7.6 cm × 6.3 cm). The base of the container was constructed from a 6.3-mm thick 6061 aluminum plate, while the sides were made of cast acrylic to provide both thermal insulation and optical access. Two 2.54-cm tabs in front and behind the PCM volume were added to allow the test section to be securely fastened to the heat source, minimizing contact resistance with the heater or temperature controlled plate. Finally, an insulation box (R-250 foam insulation) with an acrylic viewing window was placed around the test section and heat source during the melting experiments to reduce heat losses to the environment. The material properties of hexeadecane, 6061 aluminum, and cast acrylic are shown in Table 1.

Table 1*:* Material properties of the working PCM, HCM, and walls

	K [W/m·K]	**C [J/kg·K]**	**ρ [kg/m^3]**	**T_{melt} [°C]**	**ΔH [J/kg]**
6061 Aluminum	167	900	2710	-	-
Solid Hexadecane	0.24	1680	835	18.2	236.1e3
Liquid Hexadecane	0.14	2220	776	17.6	236.1e3
Cast Acrylic	0.19	1470	1186	-	-

Air-filled cavities reduce the effective composite conductivity and disturb imaging methods when the air is released, particularly for velocity measurements near the solid liquid interface. Therefore, in preparation for the melting tests, the test section was clamped onto a temperature control plate with an intermediate layer of thermal paste, and hexadecane was frozen

in layers to reduce air entrapment. The mass of PCM used corresponded to the volume required to fill liquid PCM to the fill line. After the PCM was fully frozen, the temperature control plate was set to 15 °C and the PCM was allowed to come to thermal equilibrium with the base.

2.1.2 Topology optimized test section (TOTS)

The TOTS was generated using the IFSO method with a conduction-based numerical model built in OpenFOAM v7.0. A total of three optimized designs were generated from tetralkaidecahedron (TKDS), triply periodic minimal surface structure (TPMS), and paralel fin (PF) geometry seeds. All three designs were treated as three dimensional structures for optimization using a unit cell approach. The unit cell domain was sized to be 12 mm × 12 mm × 69.35 mm to match a single fin pitch of the 12-mm PFTS, as shown in Fig. 4. The unit cell optimization was chosen to reduce the computational time required to solve the problem.

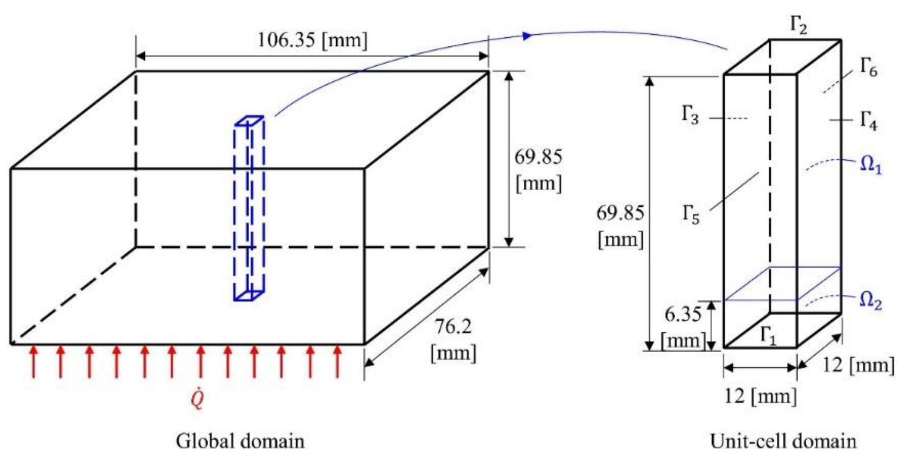

Figure 4: Global domain and unit cell of the optimization problem.

After optimization, the IFSO results were tested for manufacturability with polymer 3-D printing. This was done by exporting the unit-cell structure into a Paraview model. Then the unit cell-structure was duplicated to fill the entire design domain. The polymer proof-of-concepts are shown in Fig. 5. The design from the parallel fin seed was selected for experimental evaluation because of the readily available parallel fin baseline.

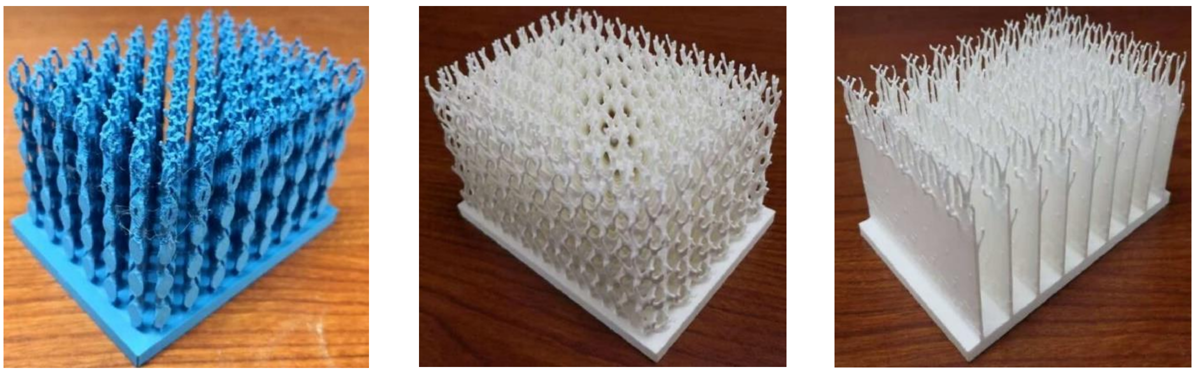

(a) (b) (c)

Figure 5: Plastic 3D printed IFSO designs from **(a)** TKDS, **(b)** TPMS, and **(c)** PF seeds.

The optimized PF design was additively manufactured using Direct Metal Laser Sintering of AlSi10Mg. This printable aluminum alloy has a nominal thermal conductivity of 130 W/m·K, which is less than generic aluminum conductivity of 150 W/m·K that was used for optimization. This discrepancy is an unfortunate limitation on the experimental tests. Even so, the experiments still provide insight into the relative effectiveness of the IFSO design method. In order to have a fair comparison between the TOTS and the PFTS, the 6061 aluminum fins in the TOTS were replaced with 7075 aluminum fins. This alloy has a conductivity of 130 W/m·K that matches AlSi10Mg. The test section was filled so that the PCM reached the fill line in its frozen state. This change was requested by reviewers, causing the device capacity to increase by 7.6% from the other parallel fin tests. The assembled test section is shown in Fig. 6.

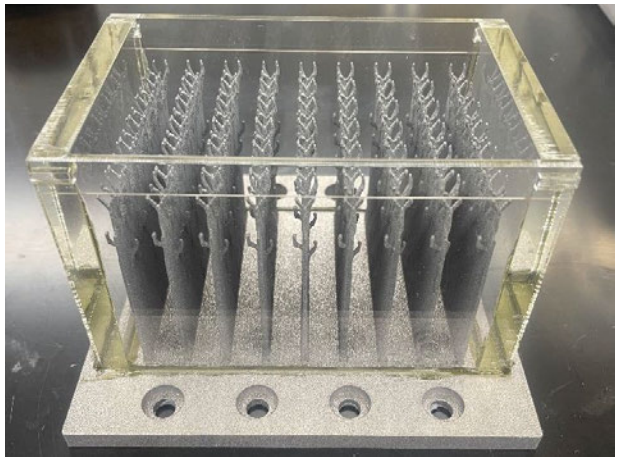

Figure 6: IFSO Test section fabricated with metal additive manufacturing.

2.1.3 Metal foam test section (MFTS)

The metal foam test section was intended to be used as a model validation for another set of topology optimization problems involving metal foams. Results from the MFTS did not agree with the numerical model, so continued efforts in that path were stopped. However, the data collected from the MFTS tests were still valuable as seemingly rare experiments that provide both temperature and liquid fraction data for metal foams. Thus, the data collected from the MFTS was used for the Ragone analyses.

The MFTS was designed and manufactured in a similar way to the previous two test sections. A 6061 aluminum base was milled with pockets for the acrylic walls. The dimensions of the PCM enclosure were 10.3 cm × 7.6 cm × 6.25 cm. Two Duocell ® 6101 aluminum foam samples were purchased from ERG Aerospace. These were then cut to size and glued to the base side by side with a thermally conductive epoxy (OmegaBond 102), as shown in Fig. 7. A summary of important foam features can be found in Table 2.

Table 2: ERG Aerospace metal foam properties

K [W/m·K]	C [J/kg·K]	ρ [kg/m^3]	Pores per inch	Relative Density
220	900	2700	5	10.3%

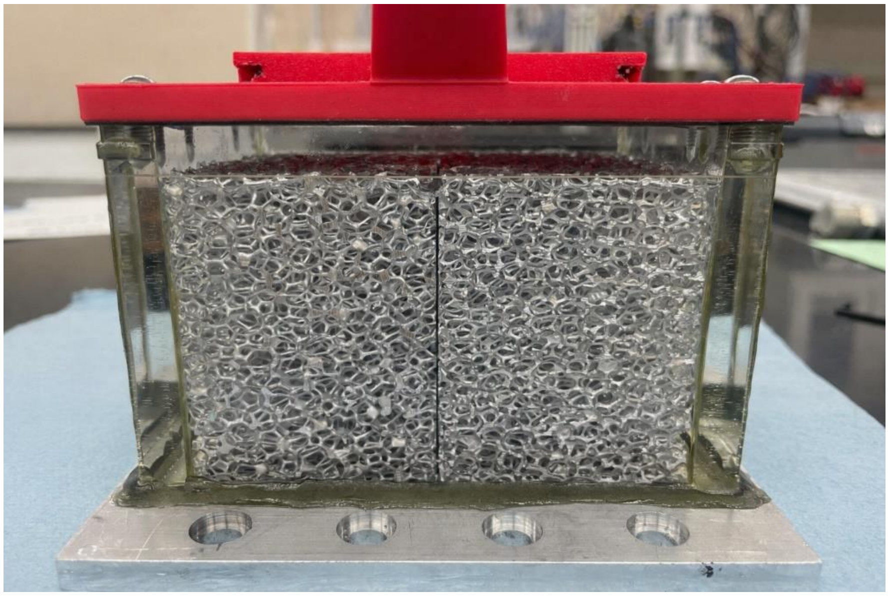

Figure 7: Metal foam test section composed of two Duocell metal foam block and a similar PCM containment method.

One possible mistake that may have occurred during MFTS manufacturing was when the metal foam blocks were adhered to the top surface of the base. The OmegaBond 102 epoxy requires a thouroughly mixed solute and solvent which then has a settling time of roughly 10 minutes. It was difficult to evenly mix and spread the epoxy across the base in this time period, so there are regions of the base that were not covered in a full layer of epoxy. This may contribute to a contact resistance at the base that inhibits heat transfer into the foam, thereby increasing the base temperature. Future attempts to manufacture metal foam test sections in this way should investigate other thermal interface materials to use at the foam-base interface.

2.2 Experimental Facilities

PCM freezing was prepared in the same manner for all tests, although PCM melting experiments were evaluated with either a constant temperature or a constant heat flux boundary condition. The two melting conditions required different experimental setups which will be described in the following subsections.

2.2.1 Constant temperature flow loop

The first facility, shown in Fig. 8(a), maintains a constant temperature boundary condition on the bottom surface of the test section by circulating conditioned water through a thermal plate (Advanced Thermal Solutions PN: ATS-CP-1004-DIY), which is designed to keep a near-constant temperature across a 15.8 cm × 16.5 cm area. Water was circulated using a variable-speed gear pump (Micropump PN: 85376) with a speed set to keep the steady state temperature rise across the thermal plate below 1.5 °C. The pump speed was chosen because larger temperature rises will result in more non-uniformity in the test section base temperature. The fluid was thermally conditioned to the desired setpoint using a brazed plate heat exchanger (Alfa Laval PN: CBH16-11H) connected to a temperature-controlled chiller and an electric heater (Watlow PN: 2187-8116). An insulation box was placed around the PCM container, as shown in Fig. 8.

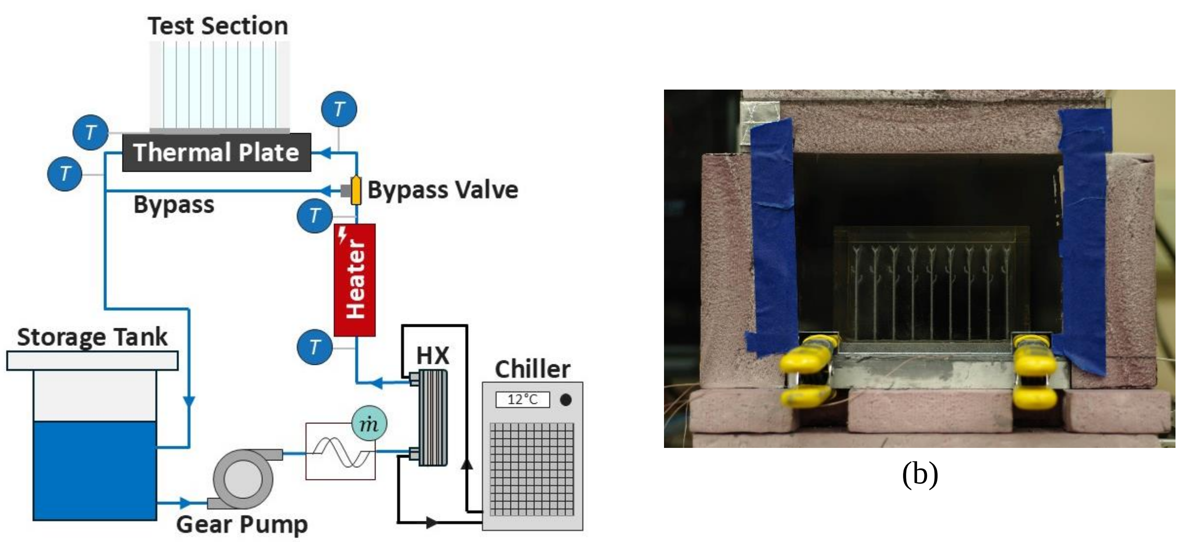

(a) (b)

Figure 8: Constant temperature flow loop **(a)** diagram and **(b)** close-up image of thermal plate (gray) with the TOTS and insulation box.

The PCM was first frozen inside the test section by lowering the chiller setpoint below the PCM transition temperature and turning off the electric heater. To reduce air gaps discussed in Section 2.1.1, PCM was poured in four roughly equivalent layers once the previous layer had fully frozen for all test sections. Maximum differences in base temperature were recorded to be no greater than 0.5 ℃ during PCM freezing. Once all the PCM was fully frozen and brought to an isothermal state, the bypass line was used to thermally isolate the test section. The chiller was then turned off, and the heater was turned on and controlled until its outlet temperature matched the desired thermal plate temperature. Finally, the constant-temperature experiment began by redirecting the flow to the thermal plate. The heater power was dynamically controlled using a tuned PID controller with base-plate thermocouple readings to maintain the thermal plate surface temperature at the setpoint. Temperature setpoints of 25 ℃, 35 ℃, and 45 ℃ were used for all fin pitch tests with the PFTS. Additional tests at 55 ℃ were conducted for fin pitches of 9 mm and 12 mm to extend the range of testing conditions of the PFTS. The constant temperature facility was not used for melting experiments with the TOTS or the MFTS.

2.2.2 Constant heat flux setup

The second facility, shown in Fig. 9, maintains a constant heat flux boundary condition at the bottom surface of the test section. After the test section was frozen with the temperature-controlled facility, it was fastened to a resistive band heater (Tempco PN: MSH04840) with thermal paste applied at the interface to reduce contact resistance. The heater was sandwiched between the test section and an acrylic block, which includes through-holes for fastening at four locations to ensure uniform pressure. A variable DC power supply was used to deliver the required power throughout each test. Power setpoints of 40, 80, and 120 W (4.94, 9.88, and 14.8 kW/m^2, respectively) were selected for the PFTS experiments. Additional tests were performed at 64 W (7.90 kW/m^2) for the PFTS at 12 mm and the TOTS for TO experimentation. Tests were run for the MFTS at 40 W, 60 W (7.41 kW/m^2), and 80 W.

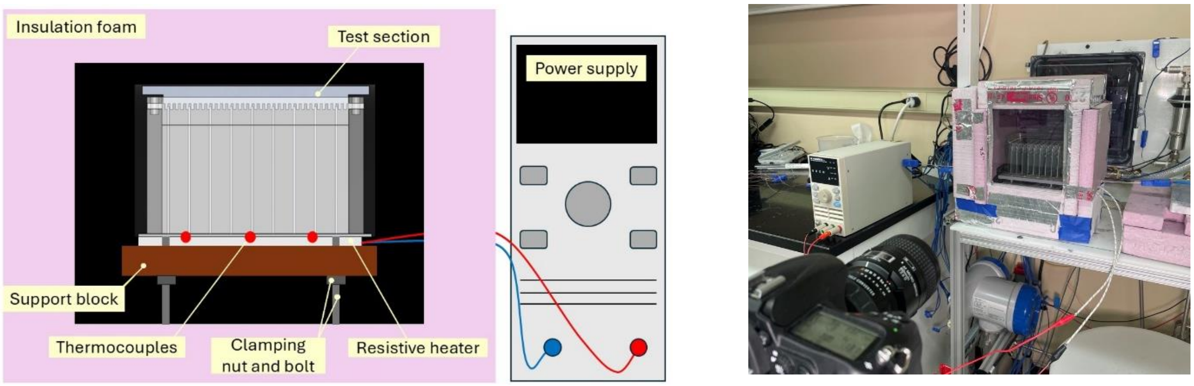

(a) (b)

Figure 9: A diagram **(a)** and photo **(b)** of the constant heat flux experimental setup.

An insulation box was placed around the test sections for constant heat flux tests as well. An estimate of convective losses at an environmental temperature of 21 °C and a uniform PCM temperature of 30 °C yields a heat loss of 0.83 W. This value is low enough to neglect natural convection losses from the acrylic walls even with the conservative assumptions that the entire PCM volume is at the representative temperature, that the air is unobstructed by the insulative enclosure, and that the ambient temperature inside the insulation box does not increase with time.

2.3 Instrumentation

Three measurement methods were used to observe local temperature, phase front, and fluid movement dynamics during the PCM melting process. These melt features were selected to explore their interdependent relationship with natural convection and PCM TES performance.

2.3.1 Temperature

Several DwyerOmega thermocouples were installed in the test section to measure the thermal characteristics during melting. For all test sections, the base temperature was measured using the average readings from three thermocouples placed at the heater-test section interface. Two of the thermocouples for the PFTS were fine-gauge welded wires (PN: TT-T-36-100), and one was a 0.0625-inch diameter probe (PN: TMQSS-026G-12) fitted into a slot that runs along the center of the base. For the subsequent test sections, three slots were made so that 0.0625-inch diameter probes were used for all base thermocouples. Additional thermocouple instrumentation was included in the PFTS to better understand the temperature response in the PCM layers. Twelve fine-gauge welded thermocouples were distributed throughout the PCM and on the fin surface to capture spatial temperature variations during melting. Fig. 10 shows a diagram and photograph illustrating thermocouple placement within the test section.

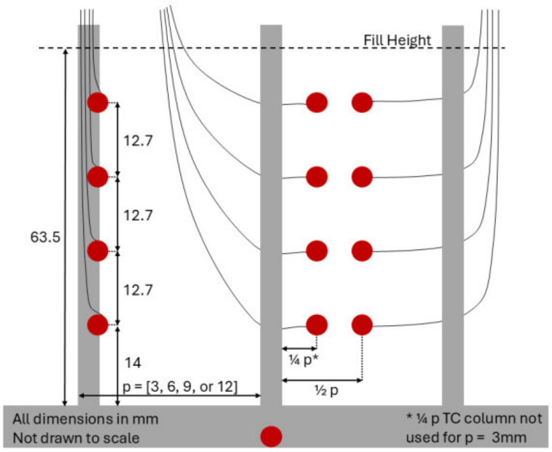

(a)

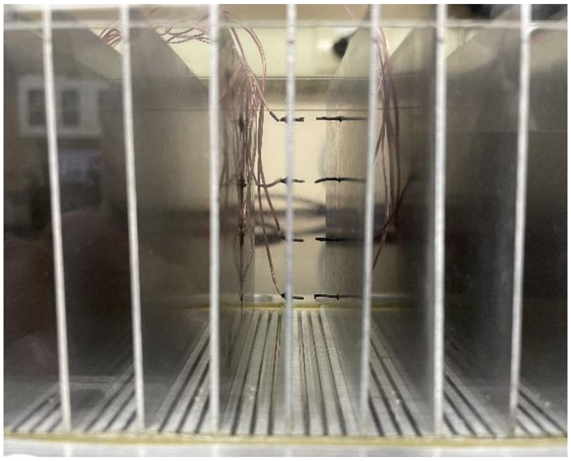

(b)

Figure 10: Thermocouple instrumentation placements shown via **(a)** a dimensioned diagram and **(b)** an image for the 12 mm PFTS configuration.

2.3.2 Image analysis of phase front

The liquid fraction of PCM was measured every 30 seconds using a Nikon D300 camera. In the images, liquid PCM appears dark and solid PCM appears light, so the liquid fraction was calculated by dividing the dark (liquid) regions by the total PCM volume. The first step of this analysis involved isolating the PCM regions by masking out bright aluminum features in

the raw image. This was accomplished by subtracting the final fully melted raw image from all preceding frames. This subtraction seeks to remove all liquid and non-PCM features, leaving only the solid PCM at high pixel intensities. The subtracted images were then binarized with a suitable threshold (Fig. 11(b)) to isolate the solid pixels. These pixels were counted in each frame and compared to the count in the first frame (when solid fills the full PCM volume) to estimate the

PCM solid fraction (f_{solid}). Liquid fraction (f_{liquid}) was taken as $1 - f_{solid}$. This method assumes that the melt front is 2-D with negligible variations in the direction perpendicular to the viewing plane.

Manufacturing constraints called for a 1.34-mm gap between TOTS fins and acrylic wall. This gap, which was filled with PCM, was farther from the conductive fins. As a result, the PCM in this region may have melted more slowly than the PCM further from the acrylic wall. This slower melting could cause a delay in the observed liquid fraction. This effect diminishes as more PCM melts away from the wall and is negligible after PCM has detached from the walls.

(a) Raw Image (b) Binarized Image (c) Masked Binary

Figure 11: Liquid fraction image processing approach for the 9-mm fin pitch test section showing the progression from **(a)** raw to **(b)** binarized and finally **(c)** masked images.

A complication arose for the PFTS tests when evaluating the liquid fraction after the solid PCM detached from the fin and acrylic surfaces and settled to the base of the test section. Although detachment occurred at about the same time for all uninstrumented channels, the thermocouples shown in Fig. 10 supported the solid PCM throughout the test, slowing the melting process in those regions. This resulted in unequal liquid fractions across unit cells. To remove the impact of sensors on the liquid fraction measurement, the instrumented channels were removed from all the binarized images, as shown in Fig. 11(c), The TOTS and MFTS did not have thermocouples embedded in the PCM, so this was not a problem for those test sections.

The binarized images were also analyzed to extract the height, width, and position of each solid body. Specifically for these measurements, only suspended PCM was used because the non-vertical orientation of the settled PCM skewed the results. These metrics were averaged across all bodies that were still suspended, including both instrumented and uninstrumented channels, when applicable. All image analysis was performed in MATLAB 2024a using the Image Region Analyzer and Image Segmenter toolboxes.

2.3.3 Particle Image Velocimetry (PIV)

One objective of the parallel fin study was to investigate the influence of natural convection on PCM melting by measuring buoyancy-driven velocity fields in the liquid phase. Particle image velocimetry (PIV) was used to estimate local velocities at varying stages of melting. In PIV, tracer particles are seeded into the fluid, and their motion is tracked by correlating pixel intensity changes between successive frames. While laser sheet illumination is typically used in PIV, it was not feasible in this setup because the solid PCM blocks the laser light unless it entered through the heated surface, which is opaque. Instead, two 85-W LED lights were directed through the front at the test section to illuminate the tracer particles. Because the particle velocities were at scales much slower than typical PIV, this method was found to successfully capture bulk fluid motion without a laser sheet.

A Basler acA2440-35uc camera with a variable lens captured 5-megapixel images at an exposure time of 1800 μs and an inter-frame frequency of 30 hz. The lens aperture was adjusted to maximize the depth of field to keep all illuminated particles in focus. Volumetric illumination was used in this setup based on the expectation that the flow would be predominantly two-dimensional. Fig. 12 shows a photograph of the PIV setup. The PIV camera, lights, and power supply were mounted on a sliding table, allowing the PIV system to be moved in front of the Nikon D300 camera between liquid fraction measurements. This movement did not introduce any noticeable error in the final velocity data.

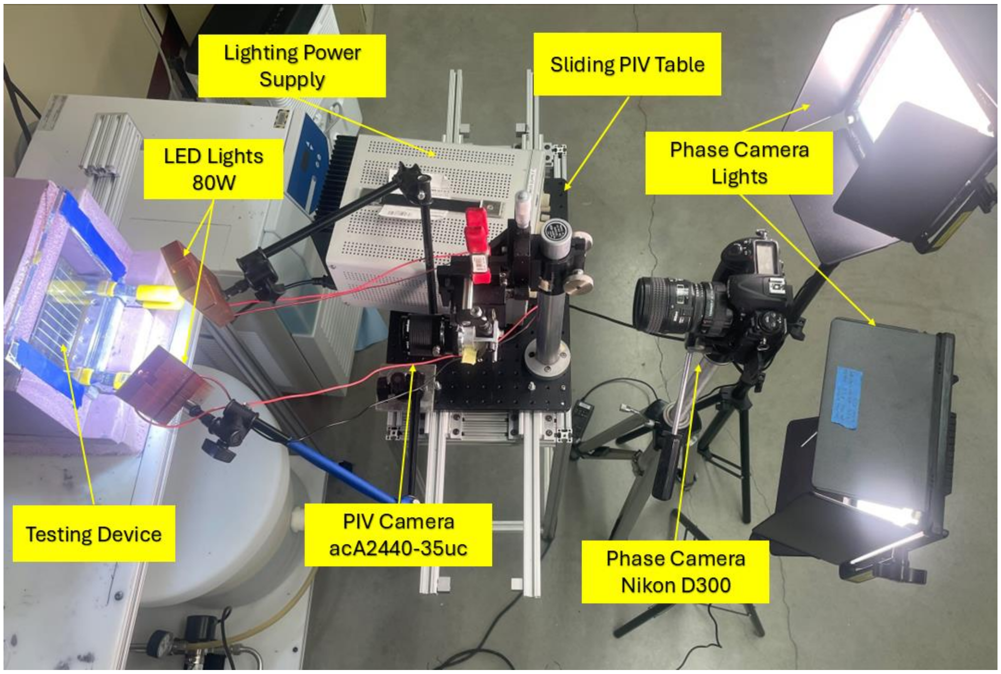

Figure 12: Image analysis setup with PIV camera in position

In PIV, tracer particles must closely follow the fluid motion to accurately represent the velocity field. The tracking fidelity is commonly assessed with the Stokes number (Eq. 1), which compares the particle response time to the characteristic time scale of the flow. For reliable PIV, the Stokes number, *St*, should be less than 10^{-3} [68].

$$St = \frac{t_0 U_o}{d_p} \tag{1}$$

Here, U_o is the characteristic velocity of the flow, t_o is the particle relaxation time, and d_p is the particle diameter. In very low Reynolds number flows (Stokes flows), the characteristic velocity U_o is taken as the particle's terminal settling velocity, derived from a force balance of buoyant, viscous, and gravitational forces in Eq. 2:

$$U_o = \frac{D_p g(\rho_p - \rho_{PCM})}{18\mu_{PCM}} \tag{2}$$

The particle relaxation time t_o is given by:

$$t_o = \frac{\rho_p d_p^2}{18\mu_{PCM}} \tag{3}$$

Eq. 3 is only applicable when the Reynolds number ($Re_p = \frac{\rho_{PCM} U_o d_p}{\mu_{PCM}}$) is much less than 1. Silver-coated hollow glass microspheres (density = 900 kg/m^3 and diameter = 25 − 65 μm) were used as the tracer particles in this experiment. The largest particles have a Stokes number St = 7.84×10^{-5} and a Reynolds number Re_p = 0.0014, confirming the Stokes flow assumptions. Given the low Stokes number, these particles are well within the limits for strong fluid tracking.

Each PIV measurement consisted of a batch of 60 images taken at regular intervals over the span of two seconds. The PIV measurement frequency ranged from one to four minutes and was based on the estimated melt duration. This resulted in seven to eleven measurements for each test. PIV analysis focused on one PCM channel between two adjacent fins. Because the images captured multiple channels, separate analyses could be performed for instrumented and non-instrumented channels. Thermocouples in the instrumented channel were not expected to strongly influence measured flow behavior because the LED lighting did not penetrate deep enough into the testing device for the tracer microspheres near the thermocouples to be captured by the camera. Image processing was performed using the open-source software PIVLab [69]. Prior to analysis, the solid PCM region was manually masked. Each frame was then preprocessed, including histogram contrast equalization and background subtraction to isolate the tracer microspheres.

For 12-mm and 9-mm pitch tests, 128, 64, and 32 pixel square interrogation window passes were made for the multipass FFT correlation using a Gauss 2 × 3-point pixel estimator. The 6-mm pitch correlation was identical to the 12 mm case except that the 128 pixel window was skipped because the region of interest was too narrow to sustain reasonable correlation certainty. The 3-mm pitch tests were not analyzed because PIVLab was unable to identify enough particles per interrogation window for a reasonable velocity estimation. Visual observations of 3-mm PIV images showed no particle movement at 40 W, but uniformly downward PCM movement at 120 W (see Appendix E for a description of selected PIV videos). These particle velocities were significantly slower than the 6-mm 40-W velocities, however they still may contribute to thermal transport.

After pixel correlation, standard deviation and local median filters were applied to the resulting velocity data to remove outliers. Finally, the data were exported to MATLAB for the 59 frame pairs and averaged into a single local velocity map. This averaging removed noise from the velocity data but did not significantly change the results because the flow was quasi-steady. More information on the PIV image collection and data processing can be found in Appendix H.

CHAPTER 3: MODELING METHODS

Three modeling approaches were evaluated to assess their accuracy in representing the melting dynamics of finned PCM composite devices. These include: (1) a one-dimensional conduction model with effective thermophysical properties, (2) a two-dimensional conduction model, and (3) a two-dimensional computational fluid dynamics (CFD) model capable of capturing buoyancy-induced liquid motion. I developed the 1-D conduction model while Tianye Wang developed the 2-D models. They will be referred to as the 1-D EMA, the 2-D conduction and the 2-D convection models in subsequent sections. The purpose of building these models was to test their accuracy with respect to experimental data and to frame the relative importance of convection and conduction heat transfer.

3-D conduction and convection models were also developed by Tianye Wang for the purposes of TO. These models were not considered in Chapter 4 (evaluation of model fidelity) because the TES design resulted in primarily 2-D heat transfer. However, using a third dimension enables more surface area generation per unit volume, which has been shown to improve PCM heat sink performance. In Tianye's implementation of TO, the optimizing function used the 3-D conduction model for its physical engine. The 3-D convection model was then used for performance predictions of the conduction-optimized geometry. The 3-D models used the same set of governing equations and assumptions as the 2-D models. Detailed descriptions of the 1-D and 2-D models are provided in the following subsections (sections on Tianye's model were co-written by Tianye and me).

3.1 1-D Conduction Model

A 1-dimensional finite difference conduction model was developed assuming that the fin/PCM composite acts as a homogeneous material with effective properties. All thermophysical properties of the PCM/HCM composite are based on volume-averaged EMA equations. The volume fraction of PCM (ϕ_{PCM}) and HCM (ϕ_{HCM}) are evaluated based on the test section width w_{ts}, fin thickness th_f, and pitch P_f, all in units of mm:

$$\phi_{PCM} = 1 - \frac{w_{ts} + 2}{P_f \cdot w_{ts}} \cdot th_f \tag{4}$$

$$\phi_{HCM} = 1 - \phi_{PCM} \tag{5}$$

where the second term in Eq. 4 evaluates the number of fins based on the pitch and the test section width. Since fin slots contacted the edges of the testing device on either side, the test section width required an additional 2 mm to correct for the final slot pitch that was cut short.

Other thermophysical properties are then calculated as effective lumped values. For example, the effective thermal conductivity k_{eff} and density ρ_{eff} are:

$$K_{eff} = \phi_{PCM} \cdot K_{PCM} + \phi_{HCM} \cdot K_{HCM} \tag{6}$$

$$\rho_{eff} = \phi_{PCM} \cdot \rho_{PCM} + \phi_{HCM} \cdot \rho_{HCM} \tag{7}$$

These properties are then implemented in a one-dimensional transient finite-difference solver, using the enthalpy approach [49] to track the state of the PCM composite. The effective enthalpy of the composite at a given temperature is modeled by mass-averaging the respective PCM and HCM enthalpies with the same reference value,

$$H_{eff}(T) = \phi_{PCM} \cdot \frac{\rho_{PCM}}{\rho_{eff}} \cdot H_{PCM}(T) + \phi_{HCM} \cdot \frac{\rho_{HCM}}{\rho_{eff}} \cdot H_{HCM}(T) \tag{8}$$

where the property type of each material in the composite (PCM or HCM) is denoted in the subscript.

Hexadecane properties were used for the PCM and 6061 aluminum properties were used for the HCM. The final model is split into two parts – a 6.35-mm thick base plate of pure HCM, and a 63-mm tall phase change composite with effective PCM/HCM properties. The base plate was split into five nodes with a length of 1.27 mm and the composite domain was calculated using a discretized form of Fourier's Law. The change in state of each node was then calculated using energy balances, where the temperature change of the internal base nodes, dT_b, with time is:

$$\left.\frac{dT_b}{dt}\right|_j = \frac{K_{HCM}}{c_{HCM} \cdot \rho_{HCM} \cdot \Delta x^2}\left(T_{b,j-1} + T_{b,j+1} - 2 \cdot T_{b,j}\right) \tag{9}$$

Where j represents the base node number, Δx is the node height, C is the specific heat capacity of the base, and T_b is the base node temperature. Similarly, the enthalpy change, $dH_{eff,i}$, of the internal PCM composite nodes were also calculated with an energy balance (Eq. 10).

$$\left.\frac{dH_{eff}}{dt}\right|_i = \frac{K_{eff}}{\rho_{eff} \cdot \Delta x^2}\left(T_{i-1} + T_{i+1} - 2 \cdot T_i\right) \tag{10}$$

The temperature of each node in the next step was then numerically integrated using the Euler approach and the relationship between effective enthalpy and temperature for the PCM composite. The simulation timestep was set to the smallest critical timestep in the problem, which is 1.8 ms and occurs in the base plate nodes. Further information on the EMA modeling approach is provided in Appendix A. Using the 12-mm 120-W test as a representative case, the model took 1.32 minutes to run on a dual socket AMD 7K62 workstation (96 total cores). This could be reduced by using a implicit integration scheme.

3.2 2-D Conduction Model

A second model was developed to understand the impacts of 2-D melting in the PCM composite. The 2-D conduction simulation model is derived from the continuous energy balance equation, which still assumes that natural convection is not present. The computational domain is split into two distinct regions: the PCM region (Ω_{PCM}) and the HCM region (Ω_{HCM}), and the interfaces of the PCM and the HCM regions are denoted as Γ_c. In the PCM region, the enthalpy approach [70] is again used to model the melting process of the PCM. The PCM material properties, including density and specific heat, are assumed to be temperature-independent and are therefore treated as constants. With these assumptions, the conduction energy equation governing thermal transport in the PCM can be expressed as:

$$\rho_{PCM} \cdot c_{PCM} \cdot \frac{\partial \mathrm{T}}{\partial \mathrm{t}} = \nabla \cdot (\mathrm{K_{PCM}} \cdot \nabla \mathrm{T}) - \rho_{PCM} \cdot \mathrm{H}_{latent} \cdot \frac{\partial \mathrm{F}}{\partial \mathrm{t}}, \quad \text{in } \Omega_{\mathrm{PCM}}, \tag{11}$$

Where F is a phase field to distinguish the solid and liquid phases of PCM, defined as:

$$F(T) = \begin{cases} 0, & T \le T_{melt,s} \\ \frac{T - T_{melt,s}}{T_{melt,l} - T_{melt,s}}, & T_{melt,s} \le T \le T_{melt,l} \\ 1, & T \ge T_{melt,l} \end{cases} \tag{12}$$

Where $T_{melt,s}$ and $\mathrm{T_{melt,l}}$ are the solidus and liquidus temperatures, defined as $T_{melt,s} = T_{melt} - 0.05$ K and as $T_{melt,l} = T_{melt} + 0.05$ K in this study. It should be noted that hexadecane has a temperature glide of 0.6 ℃, so the numerical models largely ignored any temperature change during phase transition in its governing equations.

In the HCM region, the energy equation is:

$$\rho_{HCM} \cdot c_{HCM} \cdot \frac{\partial T}{\partial t} = \nabla \cdot (K_{\mathrm{PCM}} \cdot \nabla T), \quad \text{in } \Omega_{HCM} \tag{13}$$

The PCM and the HCM regions are coupled by assuming temperature and heat flux are continuous across the interfaces Γ_c. The boundary conditions for T on Γ_c are then:

$$T_{PCM} = T_{HCM}, \quad on\ \Gamma_c \tag{14}$$

$$K_{HCM} \cdot \mathbf{n} \cdot \nabla T_{PCM} = -K_{HCM} \cdot \mathbf{n} \cdot \nabla T_{HCM}, \quad on\ \Gamma_c \tag{15}$$

Finally, there are two boundaries surrounding the computational domain: the heat source surface Γ_1 and the remaining surface Γ_2. For the heat source surface Γ_1, two different discharging conditions are considered in this study: 1) constant temperature and 2) constant heat flux. For the constant temperature condition, the boundary is condition is represented as:

$$T = T_b, \quad on\ \Gamma_1 \tag{16}$$

while for the constant heat flux, the boundary condition is represented as:

$$k_{HCM} \cdot \mathbf{n} \cdot \nabla T = \dot{q}``, \quad on\ \Gamma_1 \tag{17}$$

For the adiabatic surfaces Γ_2, the temperature gradient is set to zero:

$$\mathbf{n} \cdot \nabla T = 0, \quad on\ \Gamma_2 \tag{18}$$

The 2-D conduction model was solved for the representative 12-mm 120-W test cases in 245.8 minutes on the same workstation as the 1-D EMA model. The two-order difference in magnitude demonstrates the relative efficiency of the 1-D conduction model and highlights its strength as a potential design tool if it accurately captures the melting process.

3.3 2-D Convection Model

The 2-D convection model captured buoyancy-driven fluid motion of liquid PCM in the device. The liquid PCM is assumed incompressible, and the Boussinesq assumption is adopted to simplify the buoyancy force term. Because the model operates under a fixed total volume, it ignores the change in density during melting from 776 kg/m^3 to 830 kg/m^3. The governing Navier-Stokes equations in the PCM region, taking natural convection and phase change into consideration, are:

$$\nabla \cdot \boldsymbol{u} = 0 \tag{19}$$

$$\rho_{PCM} \cdot \left(\frac{\partial \boldsymbol{u}}{\partial t} + \boldsymbol{u} \cdot \nabla \boldsymbol{u}\right) = -\nabla \mathrm{p} + \nabla \cdot (\mu_{PCM} \cdot \nabla \boldsymbol{u}) - \beta_{PCM} \cdot (T - T_{ref}) \cdot \boldsymbol{g} - A_m \cdot \frac{(1-F)^2}{F^3 + \varepsilon} \cdot \boldsymbol{u} \tag{20}$$

Where β_{PCM} is the thermal expansion rate of the PCM ($\beta_{PCM} = 8.61 \times 10^{-4}\ K^{-1}$) for hexadecane [71]). A_m is the mushy zone constant, and ε is the small constant to avoid division-by-zero during simulations. In this study, A_m and ϵ are chosen as $A_m = 1010\ \mathrm{kg/m^3s}$ and $\varepsilon = 0.001$. The impacts of fluid motion can then be added to Eq. 21, resulting in the governing convective energy equation:

$$\rho_{PCM} \cdot c_{p,PCM} \cdot \left(\frac{\partial T}{\partial t} + \boldsymbol{u} \cdot \nabla T\right) = \nabla \cdot (k_{PCM} \cdot \nabla T) - \rho_{PCM} \cdot h_{latent} \cdot \frac{\partial f}{\partial t}. \qquad (21)$$

Boundary conditions for velocity $\boldsymbol{u}$ and pressure p can be summarized as follows:

$$\boldsymbol{u} = 0, \boldsymbol{n} \cdot \nabla p = 0, \qquad \text{on } \Gamma_1 \cup \Gamma_2 \cup \Gamma_c. \qquad (22)$$

Both the 2-D conduction and the convection models were developed in the open-source CFD software - OpenFOAM v7.0. The entire domain (106.35 × 69.85 mm^2) is discretized to a finite-volume mesh with 557 × 337 cells, resulting in a 0.2-mm mesh resolution. Time step size is fixed at Δt = 0.01 seconds so that the Courant number condition $Co = \frac{u\Delta t}{\Delta x} < 1$ is satisfied. The first-order implicit scheme (Euler) is adopted for temporal discretization. The diffusion terms are discretized through the second-order linear scheme, while the convection terms are discretized through the second-order upwind scheme. The semi-implicit method for pressure-linked equations is used in this study to deal with the coupling of velocity and pressure.

The convection model solved the representative 12-mm 120-W test case in 2044 minutes, or roughly 34 hours, on the same workstation as the other models. This additional order of magnitude increase in computational time makes it more difficult to use the model for design and optimization.

3.4 Heated Surface Boundary Condition

The boundary condition at the heat source surface Γ_1 was set to match experimentally measured values for all modeling approaches. This was necessary because tests began with a transient period before the surface conditions stabilized and reached the desired steady state boundary conditions. This can be visualized in Fig. 13, which shows the base-thermocouple readings for constant temperature tests, and heat flux estimations (described below) shown for constant heat flux tests.

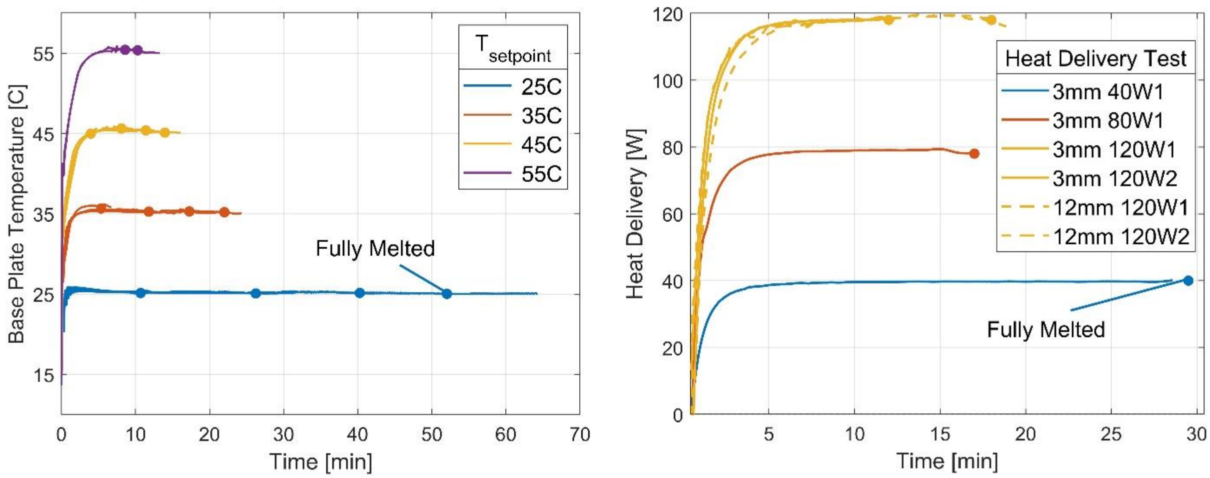

(a) Constant temperature: all tests (b) Constant heat flux: 120-W tests

Figure 13: Experimental boundary condition transience for **(a)** constant temperature and **(b)** constant heat flux boundary conditions

For the constant temperature cases, the temperature node at Γ_1 was set equal to the experimentally measured base temperature at time t. For the constant heat flux cases, the heat flux at Γ_1 was estimated based on the electrical energy input $\dot{P}_e$ and the sensible energy storage in the heater.

The sensible heat stored in the resistive heater was calculated by assuming it as a lumped capacitance with a mass of m_h. Six tests using the instrumented 3-mm pitch test section were run with thermocouples attached to the insulated surface of the heater to directly measure an effective heater temperature T_h. An energy balance was used to calibrate the specific heat capacity, c_h, by fitting c_h such that the total energy stored in the test section and the integrated delivered heat flux $\dot{q}_{delivered}$ were equivalent. With an estimated c_h value, a heat rate balance (Eq. 23) was used to obtain a temporally resolved heat flux profile.

$$\dot{q}_{delivered} = \dot{P}_e - m_h \cdot c_h \cdot \frac{dT_h}{dt} \tag{23}$$

The estimated value for c_h was 450 J/kg·K. Further information on transient heat flux and transient temperature boundary condition enforcement is provided in Appendix B.

Finally, contact resistances were added to the model to account for imperfect thermal contact at interfaces in the experimental setup. Specifically, contact resistances were present between the base plate and the heat source (thermal plate or heater), and between the base plate and the fins for the PFTS. These resistances were incorporated into the 1-D conduction model and calibrated to minimize discrepancies in total melt time for temperature-controlled tests and in base temperature at the onset of PCM melting during heat flux-controlled tests. Based on the fitted results, the base-to-heater contact resistance was set to 1.33×10^{-4} $K \cdot m^2/W$, the base-to-thermal-plate resistance was set to 0 $K \cdot m^2/W$, and the base-to-fin resistance was set to 5×10^{-6} $K \cdot m^2/W$. The base-to-fin resistance could not be directly incorporated into the 2-D conduction and convection models, so its value was added to the base-to-heat source resistance. More information about the fitting procedure and contact resistance estimation is provided in Appendix C.

CHAPTER 4: PCM MELT DYNAMICS AND MODEL EVALUATION

The goal of the experiments in this chapter, as motivated by Section 1.1, was to assess the extent that natural convection impacts PCM melting behavior at different fin pitch and power for the PFTS. Key indicators include the phase front dynamics, liquid PCM velocity, and the boundary condition dependent performance metrics. The performance metric for a constant heat flux test is the base temperature. For a constant temperature test it is the heat flux, which for this study has been proxied as the final melt time.

4.1 Phase Front Dynamics

The PCM melt front reveals the direction of heat transfer from the HCM into the PCM. Fig. 14 shows the location of the melt front for each fin pitch at a liquid fraction of approximately 55%. These images demonstrate that as the fin pitch increases, the melting behavior transitions from 1-D (bottom to top) to 2-D (fins to center). This transition from 1-D to 2-D melting has been observed in previous works [28], [32] Because hexadecane expands when it melts, liquid PCM rises above the solid PCM fill height and gives the appearance that it is melting from above as well. Visual observations of the phase front indicate that melting from the top of the solid PCM was insignificant.

The shape of the solid PCM can be described with the aspect ratio between the solid PCM length L and average width *w*: $AR = L_{PCM}/w_{PCM}$. The aspect ratio was then normalized (AR_n) by dividing by the aspect ratio of the PCM channel. If the composite behaved as an effective medium, the melt front would move horizontally away from the base, resulting in purely 1-D melting behavior. In this scenario, the normalized aspect ratio would vary linearly with liquid fraction according to Eq. 24. The difference between the measured and 1-D normalized aspect ratios was then calculated to evaluate the degree of 2-D melting behavior (either caused by fin effects or natural convection). This difference, (δ_{1D}), is calculated with Eq. 25 and is used as the primary metric for evaluating melting dynamics.

$$AR_{n,1D} = \frac{L_{PCM}}{L_{ch}} = 1 - F_{liquid} \tag{24}$$

$$\delta_{1D} = AR_n - (1 - F_{liquid}) \tag{25}$$

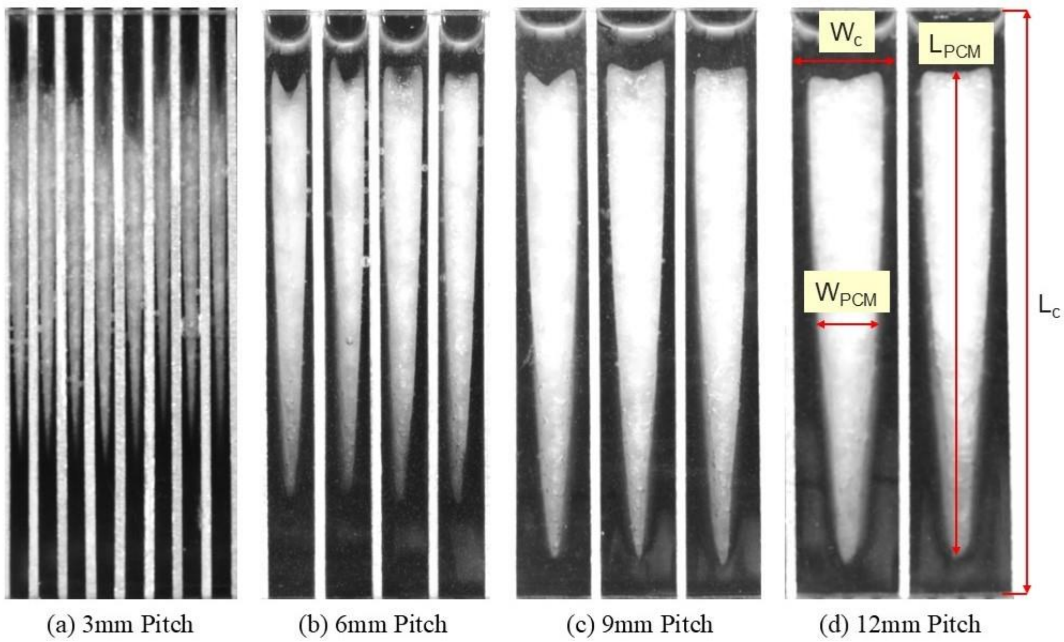

Figure 14: Images of the melting process at F_{liquid} = 0.55 ± 0.02 with key dimension labels at **(a)** 3 mm, **(b)** 6 mm, **(c)** 9 mm, and **(d)** 12 mm fin pitches.

Fig. 15(a) shows the deviation factor δ_{1D} as a function of liquid fraction for all tested boundary conditions. Overlaid are two limiting cases for a pure conduction melting scenario: one in which the melt front advances vertically from the base (1-D conduction), and another where the fin effectiveness is 1, resulting in uniform melting from all HCM surfaces. A description of the assumptions that went into the 2-D conduction limiting case is provided in Appendix D. Differences in δ_{1D} profiles are negligibly small between the investigated fin pitches.

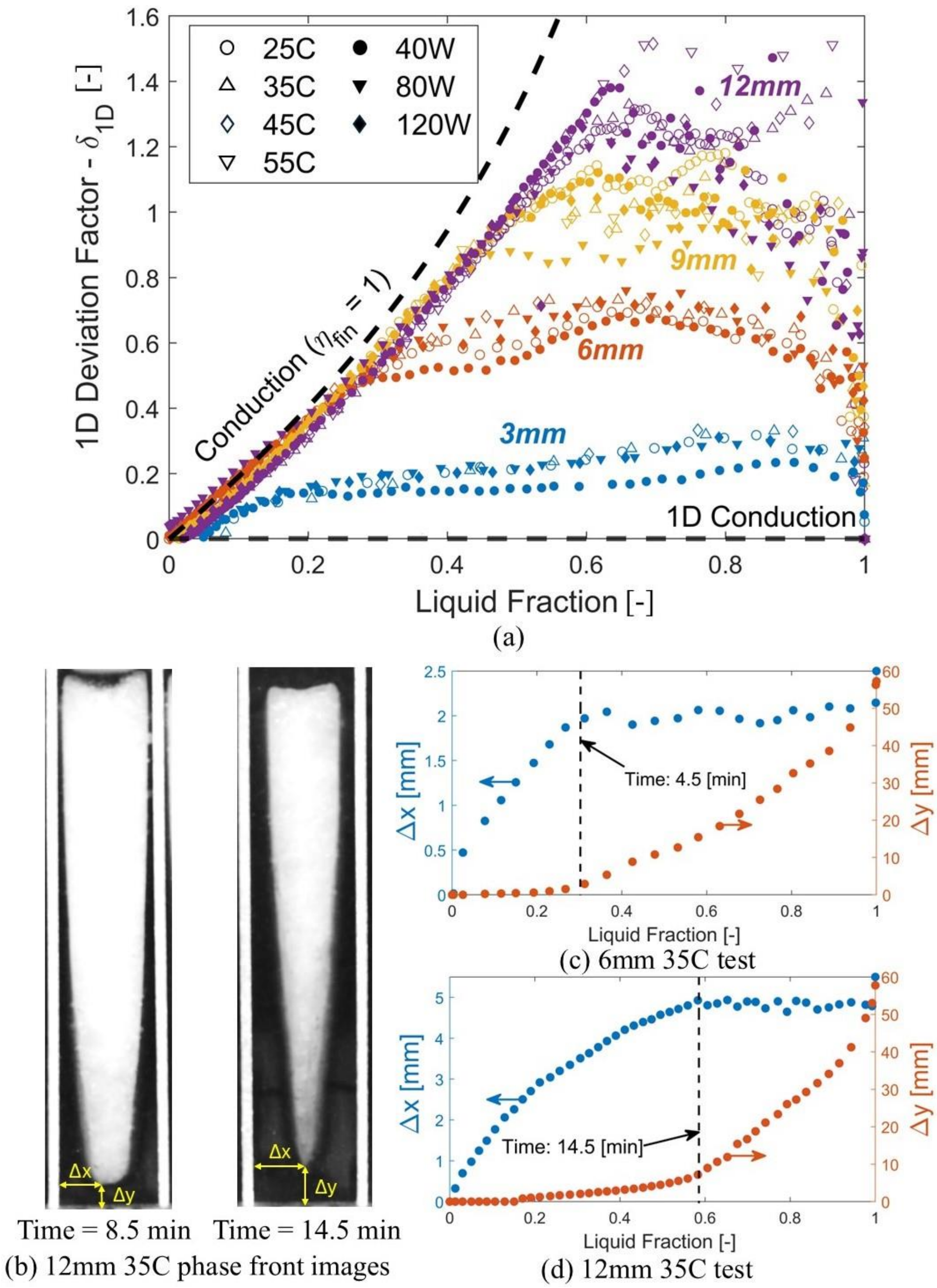

Figure 15: Melting dynamics descried with **(a)** deviation from 1-D melting across all boundary conditions, bounded by ideal cases, and **(b)** images of the 12-mm PCM phase front before and during the transition to 1-D melting (device melted with 35 ºC base temperature). The melt height vs. time for the **(c)** 6-mm and **(d)** 12 mm-fin pitches is also shown when the test sections are melted with a 35 ºC base temperature.

The results show that for all fin pitches, the melting behavior can be split into two regimes. Initially, the PCM melts away from all HCM surfaces, where the liquid thickness between the base and solid is approximately equal to the average PCM thickness between the fins and the solid. This first regime closely follows the melting shape of the perfect fin case, indicating strong 2-D melting behavior. It is understandable that δ_{1D} is slightly smaller for the experimental measurements than the perfect fin because there are temperature gradients along the fin that slows melting from the sides. The first regime is then followed by a second regime with a relatively constant δ_{1D}, which is what would be expected for a 1-D conduction case. It is worth investigating why this transition occurs and what factors cause its timing.

Fig. 15(b) displays images of the melt front for 6-mm and 12-mm tests and denotes the melt front distances from the HCM boundaries, where Δy is the distance from the base to the bottom of the melt font, and Δx is the distance from the fin to the melt front at the bottom of the solid PCM. The regime transition to 1-D melting coincides with an abrupt increase in the rate of change of Δy. This is illustrated in Fig. 15(c) and (d) by matching the liquid fraction where Δy changes slope to the liquid fraction where δ_{1D} transitions to 1-D melting for each pitch. Additionally, Δy changes slope when Δx reaches the channel centerline, bringing the solid PCM to a sharp point in Fig. 15(b). Comparing Δx between Fig. 15(c) and (d) shows that increasing the fin pitch necessitates larger Δx values to reach the channel centerline, thereby prolonging the 2-D melting period to higher volume fractions. This trend remains consistent across boundary conditions because the relative rate of change between Δx and Δy is not affected by the rate of power delivery.

4.2 Characterization of Buoyancy Driven Phenomenon

The density of liquid PCM varies with temperature, characterized by a thermal expansion coefficient. This forces liquid PCM to rise in warmer regions and fall in cooler regions, driving natural convection. Natural convection is visible in the local velocity measurements in Fig. 16 for instrumented channels in the (a) 6-mm and (b) 12-mm test sections when discharged at 45 ℃.

Streamline magnitudes generally increase with volume fraction as the liquid region grows and the fins get hotter. High fluid velocities are visible near the bottom of the solid PCM and between the fin and solid PCM for 12-mm frames.

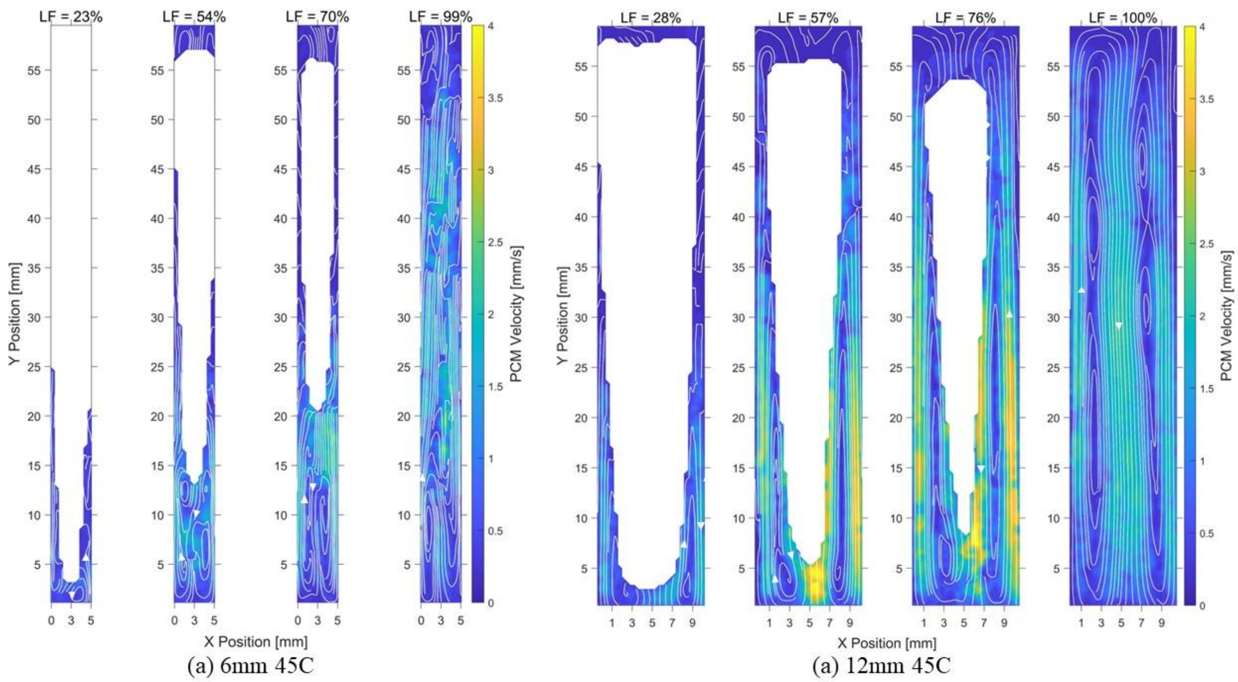

Figure 16: Local velocity measurements compared between **(a)** 6-mm and **(b)** 12-mm fin pitches at four stages in the melting process with a 45 ºC boundary condition. Streamlines are indicated in white with color-coded fluid velocity.

The direction and magnitude of the PCM streamlines are related to the linearly interpolated reconstruction of the local temperature gradients in the PCM, shown in Fig. 17. The white circles in the figure indicate the thermocouple locations, with black outlines delineating the phase front. The PCM at the bottom center of the test section is assigned the temperature of the hottest fin thermocouple. This method was chosen instead of using a thermocouple reading at the base to enable a conservative estimate of PCM temperature throughout the full channel. As a result, temperature data below the first row of thermocouples has high uncertainty and low spatial granularity. Thus, the analysis of local PCM temperatures is confined to the volume above the first row of thermocouples in the PCM composite and is limited to a qualitative discussion.

Additionally, the temperature profile is assumed to be symmetric around the center plane between adjacent fins. This assumption may introduce uncertainty in cases where natural convection currents are not symmetrical.

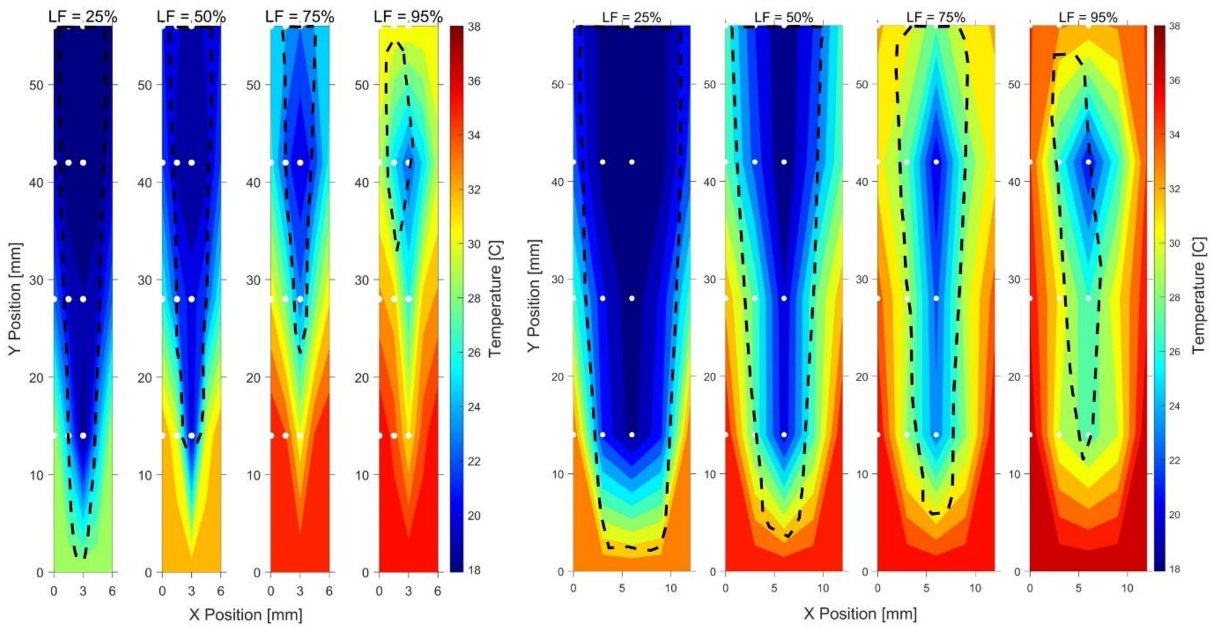

(a) 6mm 45C

(b) 12mm 45C

Figure 17: Local temperature distributions compared between **(a)** 6-mm and **(b)** 12-mm fin pitches at four stages in the melting process at a 45 °C boundary condition.

Fig. 16(b) and Fig. 17(b) shows that horizontal temperature gradients move liquid PCM against gravity along the fins and with gravity along the solid PCM interface. In the 12-mm pitch test section, horizontal gradients as large as 16 °C persist along much of the fin length and generate significant liquid velocities in the gap between the fin and the solid PCM. This fluid motion results in higher liquid temperatures near the top of the device, which aids in melting solid PCM far from the heated surface. The circulating fluid may also form boundary layers at the fin surface and PCM interface that enhance heat transfer. This effect appears to confirm results from previous numerical studies with similar PCM melting conditions [72, 73]. In contrast, the 6-mm pitch case (Fig. 17(a) and Fig. 17(b)) demonstrate that the 1-D melting behavior confines horizontal temperature gradients into smaller portions of the fin length. The added volume of HCM also promotes heat diffusion upward through the fins, thereby further reducing the scale of the horizontal temperature gradients. Lastly, the smaller pitch also narrows the gap between the solid PCM interface and the fins, increasing viscous resistance and suppressing buoyancy-driven fluid motion. These factors contribute to lower velocities magnitudes compared to the 12-mm case and confines fluid motion to the region beneath the solid PCM.

The maximum fluid velocity was extracted from the PIV data and plotted against liquid fraction in Fig. 18. This plot reinforces that fluid velocity initially increases with liquid fraction but shows a clear maximum and decreases in the later stages of melting. Comparing this data to Fig. 16, the drop in maximum velocity occurs much earlier. For instance, in the 12-mm pitch, 45 ℃ experiment, Fig. 18 shows a decrease at a liquid fraction of 55%, whereas Fig. 16 shows velocities above 4 mm/s at 76% liquid fraction. This discrepancy is related to the PIV measurement location. The data in Fig. 18 were collected in PCM channels without thermocouples, where the solid PCM detaches from the fins and acrylic wall and settles to the bottom. Once this occurs, fluid velocities decrease, likely due to lower horizontal temperature gradients in the liquid. This trend is most visible at the 12-mm fin pitch and suggests that conduction becomes the dominant mode of thermal transport once solid PCM settles to the base.

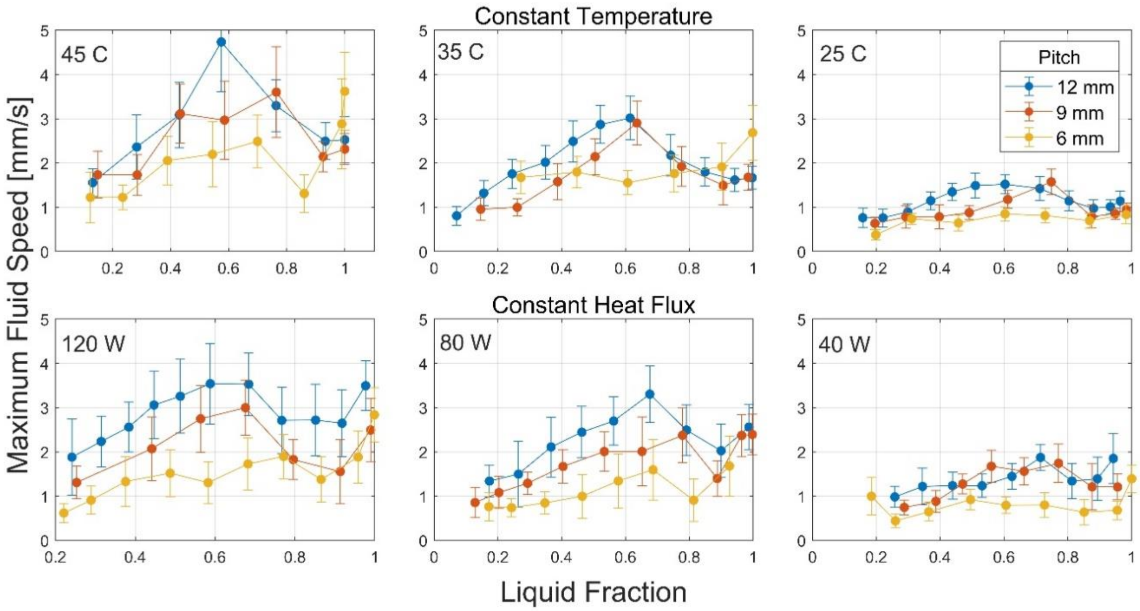

Figure 18: Maximum measured PCM velocity vs liquid fraction with aluminum fins spaced 6-12 mm apart. The results are shown for two types of boundary conditions: a range of constant base temperatures (top panel) and a range of constant heat fluxes (bottom panel). Error bars indicate a 95% confidence interval for the maximum velocity observed at each liquid fraction.

Additionally, Fig. 18 shows that the maximum PCM velocity increases with both heat delivery rate and fin pitch. Higher heat delivery rates increase the driving temperature difference between the HCM and the solid PCM, causing stronger convective flows. Conversely, lower fin pitches narrows the gap between the HCM fins and solid PCM, increasing viscous forces and impeding natural convection. These trends are most apparent when the TES is discharged quickly (45 °C and 120 W condition). The higher HCM temperatures clearly increase the velocity, but the magnitudes are significantly reduced when fin pitches are low, even for the same driving temperature difference. At 25 °C or 40 W, the driving temperature difference is insufficient to maintain strong convective flows, even in the 12-mm test section. For these conditions, velocities are low and similar across fin pitches.

The experimental trends in melting behavior and natural convection illustrate that the PCM melting process transitions from primarily conduction-dominant at 3-mm low power tests to more complicated, multi-mechanistic physics at higher fin pitches. While 2-D melting is dependent on only fin pitch, natural convection increases with both power and fin spacing. This is because the large temperature gradients that drive fluid motion require 2-D melting effects and high heat delivery rates. This dual dependence is reflected in the maximum fluid velocity plots with 12-mm pitch tests at the highest heat deliveries resulting in the largest PCM velocities. These results also suggest that natural convection does not strongly impact the location of the melt front at a given state of charge; however, as discussed in the following sections, it does impact the time it takes to melt the PCM.

4.3 Test Section Performance

Fig. 19 shows the base plate temperature over time for test sections organized by fin pitch and discharge rate. Each test begins with a rapid increase in base temperature as the solid PCM sensibly heats and approaches the melt temperature. Once melting begins, the base temperature monotonically increases until the solid PCM detaches from the acrylic walls and settles to the bottom of the test section.

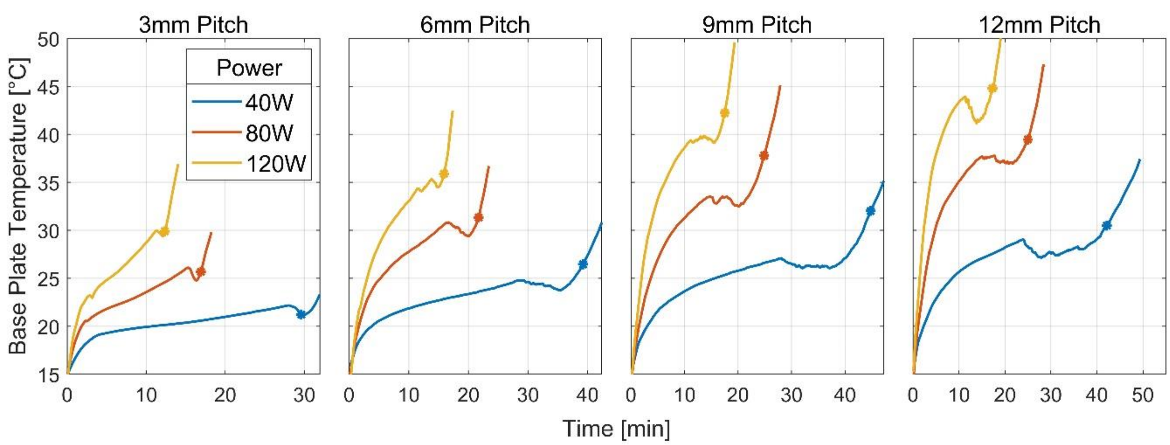

Figure 19: Base plate temperature vs time for constant heat flux tests. Results show increasingly non-linear profiles at higher fin pitches. Asterisks mark when the PCM has fully melted.

For a conduction-dominated 1-D melting scenario, PCM will melt vertically away from the heated surface and the distance between the base and solid PCM (L_{cond}) will be directly related to the liquid volume fraction ($L_{cond} = F_{liquid} \cdot L_{ts}$). If conduction is the only mode of heat transfer, the base temperature can be described using Eq. 26 once the PCM has begun melting:

$$T_b = T_{melt} + L_{cond} \cdot \frac{\dot{q}``}{K_{PCM}} \tag{26}$$

With a constant heat flux, the liquid fraction and the base temperature should also increase linearly with time.

Fig. 19 shows that at low fin pitches, the base temperature rises linearly in the suspended melting region. This is expected given the data presented previously in Fig. 15 in which the 3-mm tests appear to follow a primarily 1-D melt path, and PIV data suggests that fluid motion is limited.

For higher fin pitches, the assumptions underlying Eq. 26 break down because heat transfer is no longer purely conduction driven. Increasing fin spacing reduces the conductive pathways, which tends to raise the base temperature. However, the larger spacing and elevated HCM temperatures promote natural convection within the PCM. This additional mechanism enhances heat transfer and partially offsets the loss of conduction, limiting the base temperature growth compared to the linear trend predicted by conduction alone. As a result, the temperature profiles in Fig. 19 become progressively non-linear with increasing pitch and power. The strongest effect occurs in the 12-mm 120-W test, where vigorous convection significantly reduced the rate of temperature rise. This behavior reflects an implicit coupling between effective thermal conductivity and natural convection heat transfer coefficient through competing impacts on the base temperature.

In all experimental cases, the PCM initially detached from the fin surfaces, followed by eventual detachment from the front and back acrylic walls due to minor lateral conduction and ambient heat gain. While thin melt layers formed at the acrylic-solid interface, the melt rate in the depth direction remained secondary to the primary melting front. At liquid fractions between 40% and 95%, the PCM detachment from the acrylic wall causes the PCM to sink, thereby coming into direct contact with the heated surface below. During this period, the solid melts most rapidly at the interface directly contacting the base, suggesting that direct conduction plays a dominant role in heat transfer. During this period, the base temperature decreases and plateaus. This phenomenon is not captured by numerical models because they assume there is no density difference between the solid and liquid PCM phases. The detachment time was manually determined by selecting the first image where any detached PCM is in contact with the base. Running each 3-mm constant heat flux test three times yielded detachment times that remained within ±1 minute of the reported time.

Table 3 shows that the solid detaches around the same time for a given power level, which happens at higher liquid fractions for low fin pitch tests because they melt faster. PCM settling escalates the non-linear relationship between base temperature and time while also making it difficult to disentangle the effects of natural convection and 2-D melting dynamics in base temperature regulation.

Table 3: PCM settling time (min) and liquid fraction (%) when discharged with a constant heat flux boundary condition

-	3 mm	6 mm	9 mm	12 mm
40 W	28.2 [95.0%]	28.9 [62.5%]	27.4 [50.9%]	24.2 [43.2%]
80 W	15.4 [91.8%]	16.7 [67.6%]	15.2 [50.6%]	14.5 [48.7%]
120 W	11.3 [92.2%]	12.5 [64.1%]	11.0 [56.4%]	10.6 [55.0%]

Fig. 20 displays the total melt time when the TES is discharged with a constant temperature boundary condition. At a given setpoint temperature, the melt time decreases as HCM is added, or as fin pitches decreased. The diminishing advantage of increasing fin density is evident across this study. For example, when the base temperature is set to 25°C, the melt-time reduces by 25 minutes when the HCM volume fraction increases from 9% and 17% but only reduces by 15.5 minutes when it is increased from 17% to 33%. This trend, which aligns with numerical findings by Briache et al. [53], is driven by a reduction in local fin utilization at lower pitches. For example, at 50% state of charge the fin temperatures remained within 1°C of the melt temperature in the final 35% of the fin length for the 3-mm pitch test section. This means that much of the surface area surrounded by solid PCM is essentially inactive, causing the fins to act as a parallel 1-D conduction pathway that increases the effective thermal conductivity of the composite medium. Conversely, in the 12-mm pitch case, the PCM melts away from the fins earlier, and are significantly warmer than the PCM throughout. Consequently, increasing the HCM volume fraction can decrease the fin effectiveness, resulting in diminishing gains at lower fin pitches.

Predictably, higher temperature setpoints also shorten the melt time, but to a diminishing degree as demonstrated by Safari et al. [27]. Interestingly, only a 2% change in volume fraction from 9 mm to 12 mm had a 29% increase in melt time at the 25 °C setpoint. However, at the 55 °C setpoint, the increase in melt time reduces to 23%. This can be attributed to the increased natural convection enhancement at higher fin pitches for cases with large temperature gradients.

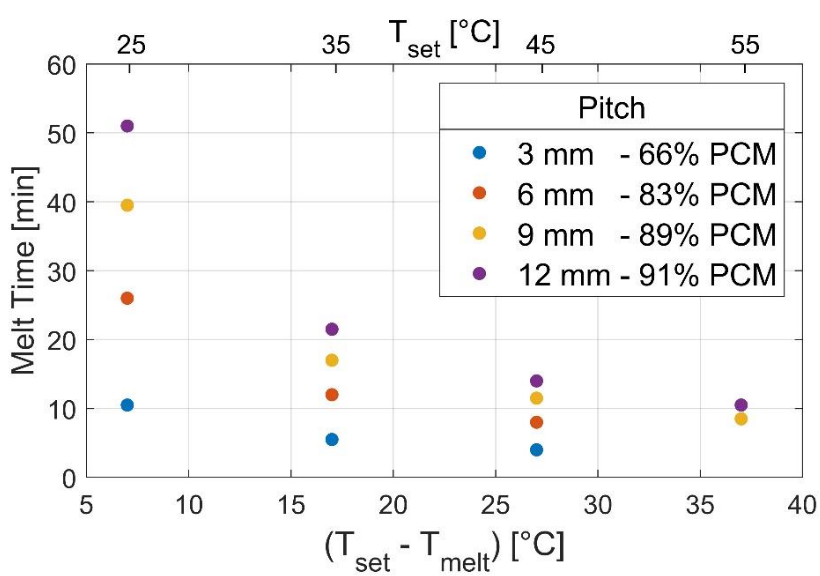

Figure 20: PCM melt times for tests discharged at a constant temperature boundary condition with volume fractions of PCM listed for each pitch.

4.4 Model Evaluation

The experimentally measured base temperature or heat flux was input into the models discussed in Chapter 3 to better understand the driving heat transfer mechanisms. Specifically, the models were compared at low (40 W) and high (120 W) heat flux, and low (25 °C) and high (45 °C) temperature setpoints across all experimental fin pitches. These cases were chosen to observe model performance at the extremes of the selected testing conditions, considering a wide range of length and time scales. These global metrics are supported by a spatial validation of local temperatures and melt-front morphologies provided in the Appendix F. The results show that the convection model effectively captures local trends.

Fig. 21 shows how the base temperature varies over the course of the constant heat flux experiment for the three models and the experiment. The solid markers indicate the final melt time, and the open marker indicate when the solid PCM falls to the base of the test section in the experiments. The y-axis varies between the 3-mm (top panel) and 12-mm (bottom panel) fin pitch results, but the grid spacing is consistent to make the results easier to compare. The percent error, defined in Eq. 27 as the time-averaged error in the base temperature between the model and experiment, is shown in Table 4

$$Model\ Error\ [\%] = \frac{100\%}{N}\sum_{i=1}^{N}\frac{\left|T_{model,i} - T_{exp,i}\right|}{T_{final} - T_{melt}} \tag{27}$$

where i represents a measured instant in time in the set of N data points and T_{final} is the experimentally measured based temperature at the melt time.

Table 4: Model to experiment base temperature error at the melt time.

Test Condition	3 mm 40 W	3 mm 120 W	12 mm 40 W	12 mm 120 W
1-D EMA	19.6%	18.2%	29.3%	40.6%
2-D Conduction	19.2%	18.4%	37.0%	58.0%
2-D Convection	19.2%	18.4%	8.2%	8.5%

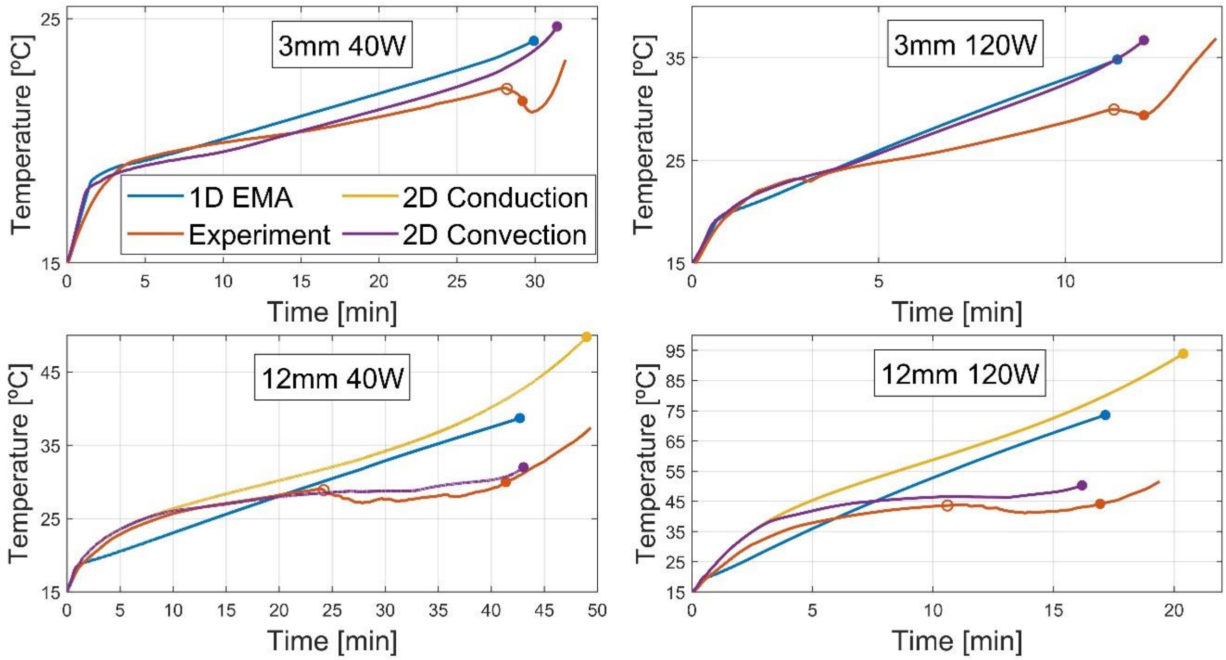

Figure 21: Base temperature comparisons between the three developed models and the experimental results at four operating conditions that represent a broad range of melting mechanisms. Hollow dots designate the visually observed detachment time; solid dots designate the fully melted time.

At the 3-mm 40-W condition, the model trends align with the experimental base temperature measurements. This is reflected in Table 4, which shows that all models have approximately the same level of error. The 2-D convection and conduction results are identical, implying that the convection model does not predict any fluid movement. In the 3-mm 120-W case, all three models have base temperature curves that are again closely grouped. The temperature difference error is similar to the lower power case, although the absolute temperatures are more noticeably different because of the higher heat flux. The 3-mm results suggest that either the thermal conductivity of the fin material is underestimated in the models, reducing the effectiveness of conduction, or that some heat transfer mechanism reduces the effective resistance about equally for the two boundary conditions. For example, 3-D cellular natural convection was observed below the solid PCM in the 6-mm pitch PIV data, which would enhance heat transfer. Additionally, a strong pressure-driven convective flow was observed in the 3-mm and 6-mm phase front videos. As discussed above, there is a significant density difference between the solid and liquid PCM. When the PCM started melting in the lower portion of the container, it expanded and pressurized while it was trapped under the solid PCM. Once small gaps grew between the solid PCM and the fins, liquid PCM quickly flowed to the top of the container above the solid. Hot liquid PCM that flows through small gaps in the solid PCM may enhance heat transfer and lower the final base temperature, especially when the discharge time is short. Because PIV videos showed minimal fluid circulation at 3-mm tests, pressure driven flow is a more likely explanation for the temperature over-prediction at the 3-mm tests. Videos of the 3D cellular natural convection and the pressure driven flow are attached in Appendix E.

In the 12-mm fin pitch test section, the convection model captures the fluid motion described in section for both power conditions. The resulting error stays much lower than the EMA and conduction models. Errors in the convection model may include effects from solid PCM falling, inaccurate contact resistances, and transient differences in power delivery. Inaccuracy in contact resistance will cause higher errors at the 120-W boundary condition, but it is unclear how other error sources may depend on testing conditions.

The presence of 2-D melting can be clearly seen by the difference between the 1-D conduction and the 2-D conduction model. When the 12-mm pitch test section is discharged at 40 W, the 1-D conduction model has a sharp transition from unregulated sensible heating to latent temperature regulation. After the transition, the base temperature is related to the length of conduction from the base to the melt front (as discussed in Eq. 26), causing a linear temperature profile with time. In contrast, the conduction model has a smooth transition from sensible heating to latent temperature regulation. This may be the result of how the initial liquid layer forms. When the pitch is small, the phase front moves predominately away from the base, increasing in distance as the liquid fraction increases. This results in an abrupt change in slope when liquid first appears and the liquid resistance establishes itself. For large fin pitches, a liquid layer develops on the base plate at around the same time, but some of the heat is routed into the fins because of the relatively high effective resistance of the composite. This causes the fins to sensibly heat above T_{melt}, allowing the liquid film to develop over more surface area. This fin heating and surface area expansion develops during the more gradual base temperature change characteristic of the larger pitches.

The significance of natural convection can also be visualized by the difference between the conduction and convection models. Looking at the 12-mm tests, natural convection appears to dominate heat transport once the transition to latent temperature regulation has finished. This occurs 10 minutes into the 40-W test, and 4 minutes into the 120-W test. After which, natural convection plays an important role in cooling the base. For example, the 2-D conduction model predicts base temperatures that are 3.3 °C and 13.7 °C higher than the convection model at the PCM settling time for the 40-W and 120-W test, respectively.

The trends in Fig. 21 can be visualized together in Fig. 22. The plot orders the tests by fin pitch and discharge rate, which is the inverse of discharge time. The 1-D EMA model and 2-D convection model accuracies are then displayed via a color map. The conduction model was not displayed because Fig. 21 showed that conduction results were either identical to the 2-D convection model when natural convection was not predicted, or worse than the 1-D EMA model.

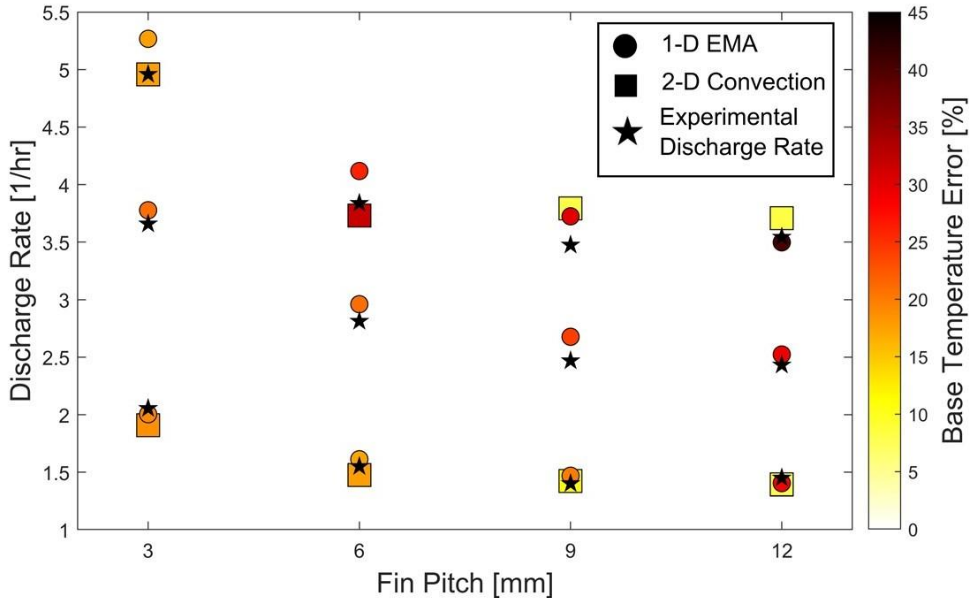

Figure 22: Base temperature model error and model discharge rates for constant heat flux tests mapped over the experimental campaign. Colors of the large dots indicate the 2-D convection model error while the colors of the small dots indicate the 1-D EMA model error.

Fig. 22 demonstrates how the dominant heat transfer mode dictates model performance. For the 1-D EMA model, error steadily increased with pitch and discharge rate as reflected in the PIV trends from Fig. 18. In contrast, the 2-D convection model was most accurate at conditions where 2-D natural convection dominated heat transfer. This transition appeared to occur between the 6-mm and 9-mm fin pitches. Notably, the 6-mm 120-W condition generated a consistently large error, further supporting the presence of 3-D natural convection and pressure driven flow at narrow pitch, high power tests. For both the 1-D EMA and the 2-D Convection model, the error in predicting the melt time remained below 10% for all conditions. This suggests that melt time prediction is less sensitive to model fidelity, and that the 1-D EMA model can be a powerful tool when melting duration is of primary interest.

A similar analysis was performed for constant temperature tests, using the melt time as the performance metric. For this boundary condition, the Rayleigh number (*Ra*) provides a convenient way to combine the effects of fin pitch and driving temperature difference into a single nondimensional parameter. The Rayleigh number characterizes the relative strength of buoyancy forces to viscous forces and thermal diffusion (Eq. 28). For this study, the characteristic length L is defined as the PCM channel volume divided by the total surface area.

$$Ra = \frac{g\beta\Delta T L^3}{\nu\alpha}, \qquad \text{where } \Delta T = T_b - T_{ini} \tag{28}$$

Natural convection becomes significant when the Rayleigh number exceeds a critical value. For vertical rectangular enclosures with a constant temperature difference between the two walls, the critical Rayleigh number is approximately 10^3 [74]. This enclosure is partially analogous to the PCM melting conditions, where hot fins and cold, solid PCM enclose the liquid region from either side. Fig. 23 shows how the prediction error for the 1-D EMA and 2-D convection models varies with Ra. The critical Ra is included as a dashed line, illustrating the transition from conduction-dominated to convection-influenced melting predicted by previous studies in simple rectangular enclosures.

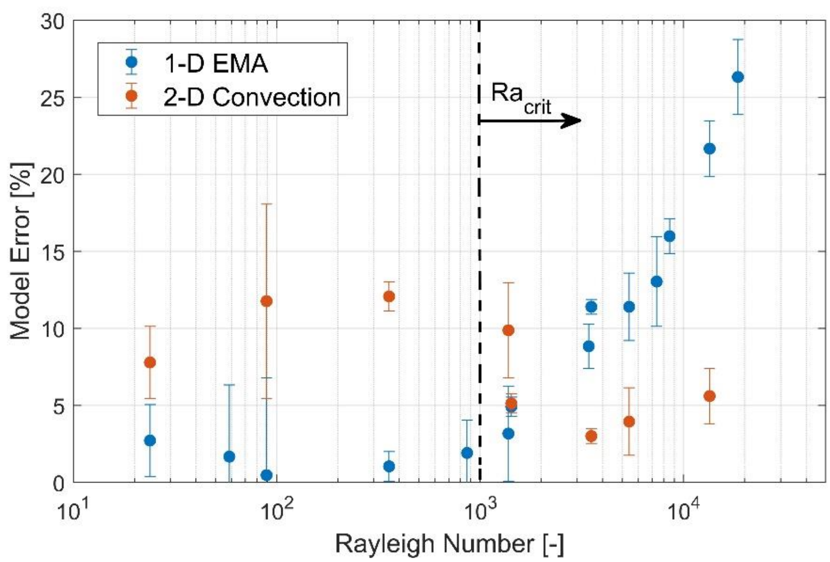

Figure 23: Constant temperature discharge-time error for the 1-D EMA and 2-D convection models with respect to the Rayleigh Number (Ra). Model uncertainty is calculated with respect to the camera interframe rate.

Fig. 23 demonstrates that at Rayleigh numbers below the critical limit, the EMA model is a strong predictor of discharge time. This is true for tests at the 3-mm and 6-mm fin pitches. Once the Rayleigh number exceeds the critical limit, the EMA model becomes increasingly inaccurate. As in Fig. 22, the convection model had lowest errors when there are clear 2-D convection currents in the composite, which mostly occur in the 9-mm and 12-mm pitch test sections (Section 4.2). While a Rayleigh number relation cannot be verified at constant heat flux cases due to the convection dependence on base temperature, constant temperature tests reveal clear limits for the 2-D conduction and 1-D EMA models. The different performance metrics between boundary conditions also affected the relative scale of model errors, with base temperature appearing to be a more sensitive metric than melt time.

4.5 Conclusions from Melt Dynamics and Modeling Work

This study investigated the impacts of fin pitch and boundary condition on the melting behavior of PCM composite TES devices. Specifically, this study described the melt front dynamics, degree of natural convection, device performance metrics (base temperature or melt time), and the accuracy of different modeling methods to predict those metrics.

The melt front dynamics follows a predictable pattern strongly influenced by the fin pitch. Early in the experiment, the PCM melts away from both the base and the fins, increasing the soild PCM aspect ratio. This change in aspect ratio is consistent with the expected melt front dynamics if the fin efficiency were one, meaning the PCM would melt equally away from the base and the fins. This initial stage of melting is largely independent of boundary condition or fin pitch but depends on the melt fraction and likely the fin properties. Once the bottom of the solid PCM tapers to a point, the melt front progresses primarily upward, away from the base.

Buoyancy driven phenomenon was characterized through local PCM thermocouple measurements and PIV velocity estimations. Local temperature plots highlight the importance of horizontal temperature gradients for inducing liquid PCM movement. Increasing fin pitch, and consequently the degree of 2-D melting, promotes fluid motion in the liquid PCM regions. Additionally, fluid motion became increasingly dependent on the heat input rate at higher fin pitches, with higher heat inputs driving stronger natural convection currents. In addition to the characterizing the melting process, this study measured overall device performance and compared the results to different transient heat transfer models. The PCM composite domain was modeled with three approaches — a 1-D EMA conduction model, a 2-D conduction model, and a 2-D convection model. These models were compared to the experimental results to evaluate their ability to predict device performance. Constant heat flux results showed that the conduction models performed reasonably well for low powers and fin pitches, but failed to accurately predict base temperature for other cases. The convection model could accurately predict base temperature or total melt time for conditions when natural convection was present and limited to 2-D eddy structures ($Ra > 10^3$), but the 6-mm 120-W case suggested that 3-D natural convection or pressure induced flow may significantly affect base temperature at high discharge rates. A summary of model computational times, limiting flaws, and recommended use cases is presented in Table 5.

Although hexadecane was used as the PCM for this study, the models accommodate various material properties through user-defined inputs. Since the modeling approach avoids empirical fitting parameters, the observed melting behavior and model performance should remain valid for other PCMs with similar characteristics. Nevertheless, the broader relevance of some trends depends on specific property combinations. For example, PCMs with solid-to-liquid density ratios near one (e.g. heptadecane) may not undergo detachment and settling, while materials with higher viscosity or lower thermal expansion coefficients (e.g., octadecane) will exhibit reduced natural convection. The HCM properties are also considered, where higher HCM thermal conductivity (i.e. copper) would increase heat transfer enhancement and lower base temperatures.

These examples may alter the range of applicable use conditions for a given model, but the mechanisms that cause these limits would remain unchanged. In contrast, fundamental changes to the HCM structure—such as the integration of metal foams or nanoparticles—alter the underlying heat and mass transfer dynamics significantly and would require separate modeling evaluations.

Table 5: Summary of model computational time, limiting flaws, and recommended use cases. Note that the compute time was recorded for the 12-mm 120-W case.

	1-D EMA	**2-D Conduction**	**2-D Convection**
Compute minutes per simulated minute	0.0348	7.37	111
Primary model limitations	Inaccurate for pitches >3 mm due to neglected 2-D melting and significant natural convection at higher pitches.	Neglects convective circulation (dominant at 6-mm pitch and high power and all discharge conditions at >6-mm pitch)	Neglects 3-D natural convection, pressure-driven flows due to volumetric expansion (both at low pitch/high power) and late-stage PCM detachment.
Recommended use cases	- Discharge time for constant base temperature melting with Ra $\leq 10^3$ - Global discharge estimates for constant heat flux boundary conditions - Base temperature for 3-mm pitch or lower at any heat flux	- Not recommended; no cases where 1-D EMA does not provide similar fidelity	- Discharge time for all discharge conditions - Base temperature prediction for 12-mm pitch or lower at heat flux $\leq 4.94\ \mathrm{kW/m^2}$ - Base temperature prediction for 9-mm pitch or higher at any heat flux*

*The 2-D convection model may be less physically representative when PCM detachment is present, although prediction accuracy stays reliable even when detachment dominates late-stage heat transfer.

This study focused on understanding the important mechanisms that dominate lamellar PCM composite melting behavior and explaining how these mechanisms influence model accuracy across testing conditions. Future work could help clarify these findings by better characterizing contact resistances, increasing the range of testing conditions, and including the impacts of solid/liquid density differences in a 3-D convection-based model. Other PCMs could also be investigated to discern if the trends found with hexadecane remain consistent across other hydrocarbon PCMs. This work also aimed to inform future corrections of the EMA model so that it can be used as a computationally efficient and accurate means of predicting PCM melting behavior.

Using a characteristic Rayleigh number may be valuable for correcting natural convection in lamellar PCM composite melting models. If doing so can meaningfully extend the range of the EMA model, it could allow designers to quickly iterate through fin parameters to maximize energy density and power density at unique design conditions. While heuristic, this approach is promising in its potential versatility and ease to develop. Furthermore, it can be leveraged for more deliberate optimizations as has been shown in previous studies [36, 37].

CHAPTER 5: TOPOLOGY OPTIMIZATION

The goal of the work discussed in this chapter, as motivated in Section 1.2, was to evaluate the efficacy of the IFSO method using the 2-D conduction model at (a) generating improved PCM composite designs from a 12-mm spaced parallel fin seed, and (b) predicting the degree of device improvement based on its optimization objective. The design conditions were selected in part because of the clear presence of natural convection at 12 mm. This allowed for additional discussion on the merits and limitations of using a conduction-based model for PCM devices with convective heat transfer.

5.1 Optimized Design

The parallel fin IFSO optimization method was developed and numerically implemented by Tianye Wang. Professor Mahvi, Proffesor Xian, and myself contributed to the setup of the design problem as pertaining to the constraints, optimization goal, and device geometry.

The parallel fin optimization problem was constructed for a single unit cell of the 12-mm fin pitch parallel fin device. The optimization goal was to minimize the average base temperature at a stated operation time (called the design condition) of 1760 seconds at a power delivery of 7.90 kW/m^2. This heat flux is equivalent to a 64-W load being applied to the PFTS. A constraint was added that maintained the HCM volume fraction at 8.33% so that it was the same as the parallel fin design. The device operation time should be sized so that the total heat input is close to the device capacity. Thus, the design condition of 1760 seconds was selected because it was numerically observed that the 12-mm PF design reached within 5% of fully melted at that time. A final constraint was added that prohibited the optimizer from generating designs with overhang angles greater than 45° in the print direction. The measured performance improvement was calculated using Eq. 29.

$$Improvement\ [\%] = \frac{T_{PF} - T_{IFSO}}{T_{PF} - T_{melt}} \times 100\% \quad (29)$$

The final design and the design evolution are shown in Fig. 24(a) and Fig. 24(b). During the optimization process, there were two main changes to the geometry: 1) in the top region, the single fin is eroded to several pin-like fins first, and then those fins generate bifurcated branches as marked by the red square; 2) in the middle region of the main fin, several bumps are generated, which later evolve into two side-wall fins as marked by blue squares.

The temperature performances of the IFSO and PF designs are shown in Fig. 24(c). At t = 1760 seconds, the average bottom plate temperature of the PF design is 59.87 °C, while the optimized IFSO temperature is 54.43 °C. The performance improvement calculated by Eq. 29 is 12.69%. The liquid fraction evolutions of both cases are plotted in Fig. 24(d). At the design condition, the IFSO design has 3.44% more melted PCMs than the PF design, indicating that more heat is conducted away from the base, thereby melting more PCM near the top of the structure and resulting in less superheated PCM near the base.

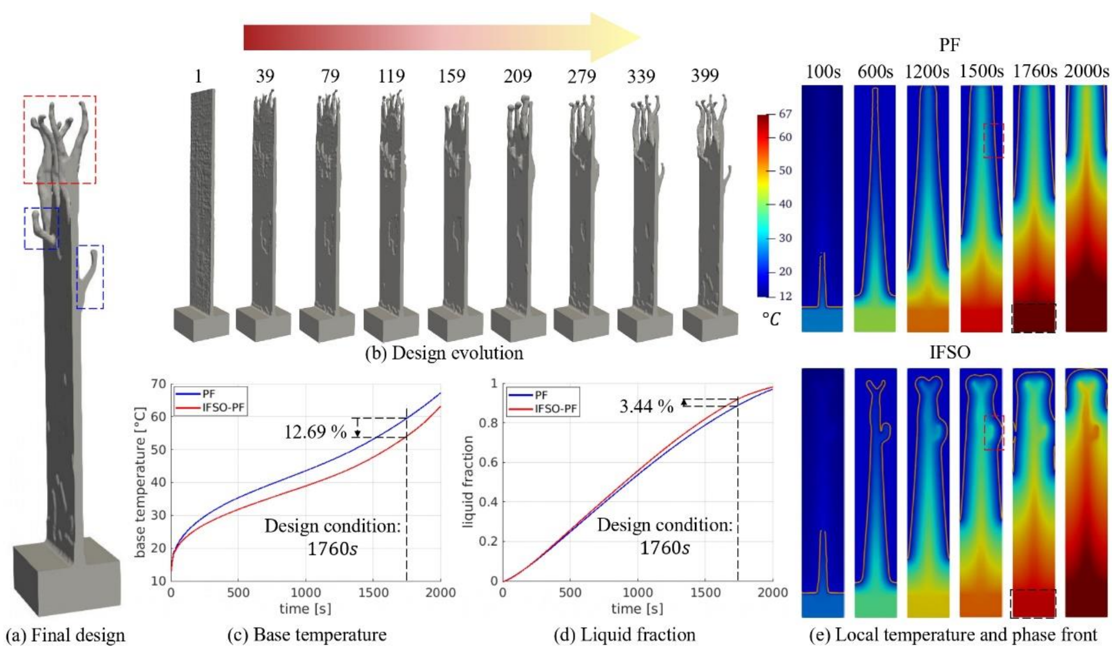

Figure 24: Design evolution **(a)** and **(b)**, performance **(c)** and **(d)**, and local fields **(e)** of the IFSO optimization using a 3-D conduction-based model.

The temperature field and the phase front are also examined, as shown in Fig. 24(e). The first row shows 2-D cross-sections of the PF fields at six different times, while the second row shows the same results for the IFSO case. The temperature fields demonstrate the utility in bifurcating fin structures. Their increased surface area enhances the melting rate, allowing for more effective heat removal from the base. This is highlighted in Fig. 24(e) with the red box at 1500 seconds and the black box at 1760 seconds.

5.2 Experimental Results

Before addressing the performance of the IFSO optimized design, it is important to discuss the limitations of the conduction-based optimizer. Experimental observations of the phase front demonstrate ways in which the optimizer missed some physical phenomena and can give insights into how this will affect the respective device performances. Fig. 25 shows four snapshots of the phase front starting at 1020 seconds and ending at 1620 seconds, shortly before the optimizer evaluation time. At 1020 seconds, the apparent phase fronts look very similar between the IFSO and PF device. However, at 1260 seconds, the first PCM body detaches from the acrylic walls in the PF device. This detachment causes the solid PCM body to sink, putting it in close thermal contact with the base. As more PCM settles, direct conduction between the base and solid PCM becomes a dominant heat transfer mechanism that can lower the base temperature. This process does not begin until 1500 seconds for the IFSO device because of its branching fins that suspend the solid PCM even after its detached from the acrylic walls.

The described phenomenon is caused by buoyancy differences between solid and liquid PCM (the density of solid hexadecane is 835 kg/m^3 while liquid hexadecane is 776 kg/m^3). This difference is not accounted for in any of the models, where PCM density is assumed to be constant.

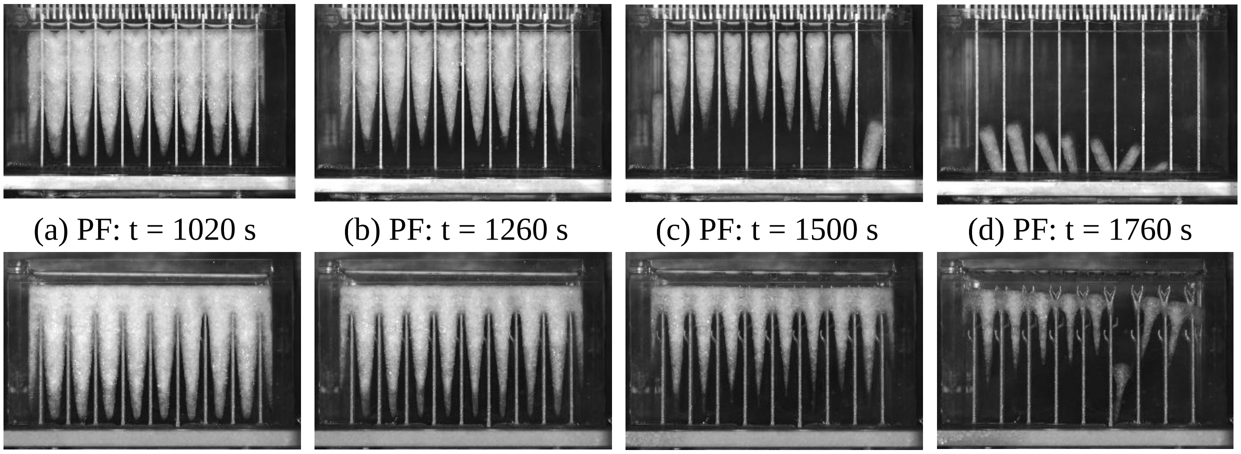

(a) PF: t = 1020 s (b) PF: t = 1260 s (c) PF: t = 1500 s (d) PF: t = 1760 s

(e) IFSO: t = 1020 s (f) IFSO: t = 1260 s (g) IFSO: t = 1500 s (h) IFSO: t = 1760 s

Figure 25: Snapshots of the experimental melting process for (a-d) PFTS, and (e-h) TOTS.

In addition to the density difference between solid and liquid PCM, temperature variations within the liquid PCM can cause buoyancy driven flow. Buoyancy driven flow can considerably influence the base temperature via natural convection boundary layer development or simply circulating hot PCM upwards and cold PCM towards the base. Fig. 25 shows large regions of liquid PCM below and beside the solid PCM where natural convection could develop before solid PCM settling. While natural convection was not considered in the optimization, a 3-D CFD simulation in OpenFOAM with buoyancy driven flow was performed after the optimization to gauge the significance of these effects.

Fig. 26(a) shows the base temperature as a function of time for the once-repeated experimental tests, conduction-based simulations, and convection-based CFD simulations. The results show that the IFSO device maintains lower base temperatures throughout the duration of the test and that differences between repeated experiments were minimal.

The results also show that natural convection in the liquid PCM flow has a significant impact on the base temperature. At the evaluation time, the IFSO test was 20.76 ℃ colder than what the conduction model predicted. This is contrasted by the convection-based model which shows strong parity with the experimental results. The time at which PCM settling occurs is identified by a decrease in base temperature for both devices (roughly 1400 seconds for PF and roughly 1750 seconds for IFSO). Before these times, the difference between the conduction model predictions and experimental data can be attributed entirely to natural convection. After these times, heat transfer is dominated by conduction from the base to the fallen PCM. This transition in primary heat transfer mechanism from natural convection to near-base conduction causes the convection model to lose agreement with the experiment at the late stage.

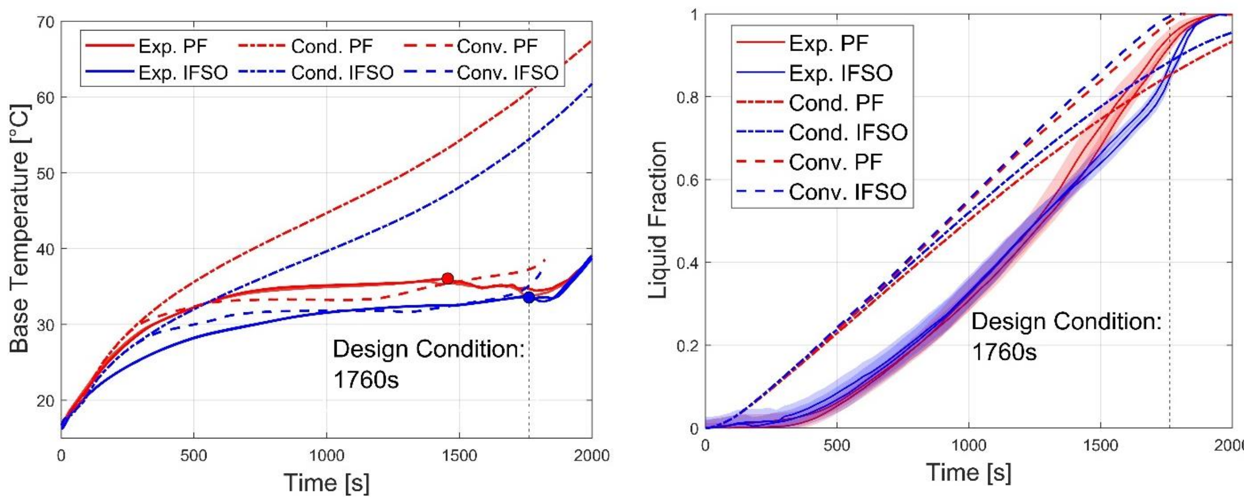

(a) Temperature (b) PCM liquid fraction

Figure 26: Experimental performance comparison of (a) base temperature and (b) liquid fraction between the IFSO and PF designs.

Previously, performance improvement was evaluated using Eq. 29 at the design condition, yielding an IFSO performance improvement of 4.43%. This value is small because of the unpredicted impact of PCM settling. Eq. 29 references the optimization objective of minimizing base temperature at a given time, although that objective was selected with the assumption that the base temperature would monotonically increase. This is supported in the temperature profiles of the conduction and convection simulations in Fig. 26(a). Under this assumption, an equivalent objective would be to minimize the maximum base temperature before a set evaluation time, as visualized with the color-coded dots in Fig. 26(a). This metric would consider the experimental effects of natural convection and PCM settling while retaining an equivalent conduction-based optimization goal in mind. The resulting IFSO performance improvement with respect to maximum temperature is 12.11%. This is very close to the predicted performance improvement of 12.69% despite its sizeable differences in final base temperature. The convection-based model predicted an 11.33% improvement for the IFSO design, reinforcing the strong parity between it and the experiment.

The similar value in the optimizer-predicted performance improvement and the actual improvement may suggest that natural convection enhancements are not highly dependent on the HCM structure. In other words, relatively small changes in HCM structure introduced in the IFSO method may not significantly impact convective heat transfer while improving conduction heat transfer. Although this claim remains speculative with only one experimental data point, subsequent convection-based optimization efforts show nominal improvement over the conduction optimizer for similar conditions.

Fig. 26(b) compares the experimentally measured liquid fraction to the conduction- and convection-based simulation results. The conduction and convection simulations predict similar linear liquid fraction growth until around 1000 seconds, at which point the convection model begins to deviate due to natural convection. Unlike the models, the experimental tests have a 400-second delay before the liquid fraction begins to noticeably increase. This delay is likely the result of differences in how liquid fraction is measured between the models and experiments. The experiments require full melting of a region before it is considered melted, whereas the models account for any latent heat utilization as contributing to the liquid fraction. This possible error is compounded by the lag caused by a 3-D PCM melt front discussed in Section 2.3.2. Considering these error sources, the final melt times between the experiment and convection model still show reasonable agreement.

One common characteristic between all testing methods is the similarity in liquid fraction histories between the PF and IFSO devices. For example, PF and IFSO liquid fractions are indistinguishable throughout most of the experiment (see Fig. 26(b)). Their eventual divergence, denoted by a sharp increase in PF melt rate, aligns with the PF PCM settling time of 1400 seconds. A similar spike in melt rate can be observed in the IFSO data at 1750 seconds. While the experiments may fail to verify that exact liquid fraction histories are accurately represented by either model, they do demonstrate that the IFSO method achieves better base temperature profiles without sacrificing a significant increase in melt rate, and consequently a smaller operational time.

The experimental results demonstrate that while the physical model fails to capture all heat and mass transport mechanisms for the optimization scheme, the final design still showed significant experimental improvements. Furthermore, the IFSO approach can be used with initial designs that diminish the importance of the density-based phenomena that drove errors between the models and experiments. For example, natural convection cannot develop in liquid PCM regions that are frequently interrupted by HCM structures, and solid PCM cannot easily fall to the base if there are HCM structures beneath it. Device geometries like the TPMS and TKD structures are strong examples of when conduction-based modeling could still capture all the important heat and mass transport. [44, 45]. Thus, the observed model errors are not inherent to all PCM designs, but they do motivate future work integrating density-based phenomenon into a solver for the IFSO method. Otherwise, the IFSO method should be experimentally tested at initial seeding conditions that restrict natural convection, either by minimizing the unit cell domain or generating device constraints that require high volume fractions of HCM.

5.3 Conclusions from Topology Optimization

This study improved the traditional parallel fin design through the novel IFSO method. Optimization via a 3-D conduction-based model yielded a fin design with a truncated height and bifurcating fins. The conduction-based solver predicted a device improvement of 12.69%, with experimental tests confirming this prediction with an improvement of 12.11%. However, significant discrepancies between the optimizer-predicted base temperature motivated a discussion on the dominating heat transfer mechanisms. Similar to the findings from Section 4.3, natural convection and PCM settling dramatically reduced the final base temperature compared to the predicted values from the conduction-based model.

The importance of buoyancy driven mechanisms prompts further investigations that deploy more robust optimization models with different heat flux profiles. Additional numerical investigations may be performed with the goal of demonstrating a clear advantage to using a convection-based solver. They could include a comparison between two optimized geometries: one that relied only on conduction, and one that considered natural convection during optimization. A comparison between the two, both numerically and experimentally, would show whether the increased fidelity in the convection model optimization corresponds to further device improvement. The optimization and testing procedures could also be repeated at different boundary conditions and initial HCM geometry seeds to study how the results change for a variety of conditions. Lastly, different heat flux profiles may impact how useful natural convection may be as a design consideration. Investigating a partially heated boundary at the base may reveal a different dynamic in the balance between natural convection and conduction-based optimization.

CHAPTER 6: ENERGY AND POWER CAPACITY ANALYSIS

As motivated by Section 1.3, this chapter investigates PCM heat sink performance using the Ragone framework. Results are evaluated on a device-level basis where energy density and power density are competing figures of merit.

6.1 Data Preparation

The following analysis was done using data from the test sections described in Section 2.1 and from additional data collected from published studies on PCM device performance. These studies provide context for how the test sections discussed in this work compare to other previous findings. The selection criteria and data processing methods for the literature survey are provided in Section 6.3.

The sets of experimental and literature data were processed into a database with a standardized format for easy manipulation into Ragone results. There were three input parameters for modifying the Ragone analysis: the cutoff temperature difference, the basis for energy and power density (by volume – volumetric, or by mass – gravimetric), and the option to normalize the data by a device characteristic.

The cutoff temperature difference set the available temperature rise above the melting temperature that the base can sustain, after which, the remaining latent energy is unusable. The cutoff temperature is critical for evaluating the latent energy capacity a device holds. In addition, using a temperature increase from the melt temperature rather than a constant temperature enables comparison between studies that use PCMs with different melting temperatures.

The option to normalize by mass or by volume did not play an important role in the analysis of in-house devices because they used same PCM and HCM. If the material properties had been a varied parameter in this analysis, the basis for calculating density would be an important factor depending on the application the PCM device is meant for.

After an initial analysis, it was quickly determined that further normalization beyond the melting temperature would be required for a meaningful analysis of dissimilar heat sink architectures. Device characteristic normalization was included to remove a selected property from the comparison between two or more devices. For instance, normalizing energy and power density by the latent heat of fusion removes the advantage one device may have from a PCM that has higher latent heat of fusion than another, allowing for a more direct comparison on enhancement methods. In all, these input parameters tailor the Ragone analysis to a specific question while granting the specificity required to achieve meaningful results.

6.2 Evaluation of Present Work

Discussions from Chapters 4 and 5 focused on melting behavior, modeling, and optimization, but did not recommend a specific device based on design criteria. To address this, the parallel fin, IFSO, and metal foam test sections were evaluated based on their power and energy densities at specified cutoff temperatures (i.e. design criteria). The results were not normalized by a device characteristic because the same PCM was used in all tests. Additionally, the device volume was selected as the basis for the figures of merit.

The first step in evaluating energy density and power density was to record the base temperature and SOC response of a device at a given power. This relationship is often called the rate capability of the device in energy storage literature. This is demonstrated in Fig. 27 with the performance of the PFTS at a fin pitch of 12-mm and the MFTS, both plotted at 40 W and 80 W. The power density was inherently set by the testing condition and is therefore independent of the device performance. However, Fig. 27 reveals that at the temperature setpoint of 36 ºC, the usable energy storage is a strong function of the device rate capability. For example, at a power of 40 W, the MFTS base temperature quickly crosses the cutoff temperature with the liquid fraction of 0.46 (SOC at 54%). In contrast, the PFTS completely melts before crossing the temperature cutoff. From this, it is expected that because the PFTS used roughly twice the latent heat of the MFTS, the PFTS will have roughly twice the energy density at the observed condition. At 80 W, the PFTS still outperforms the MFTS, however the degree of improvement is lessened because the PFTS also crosses the temperature threshold early in the melting process.

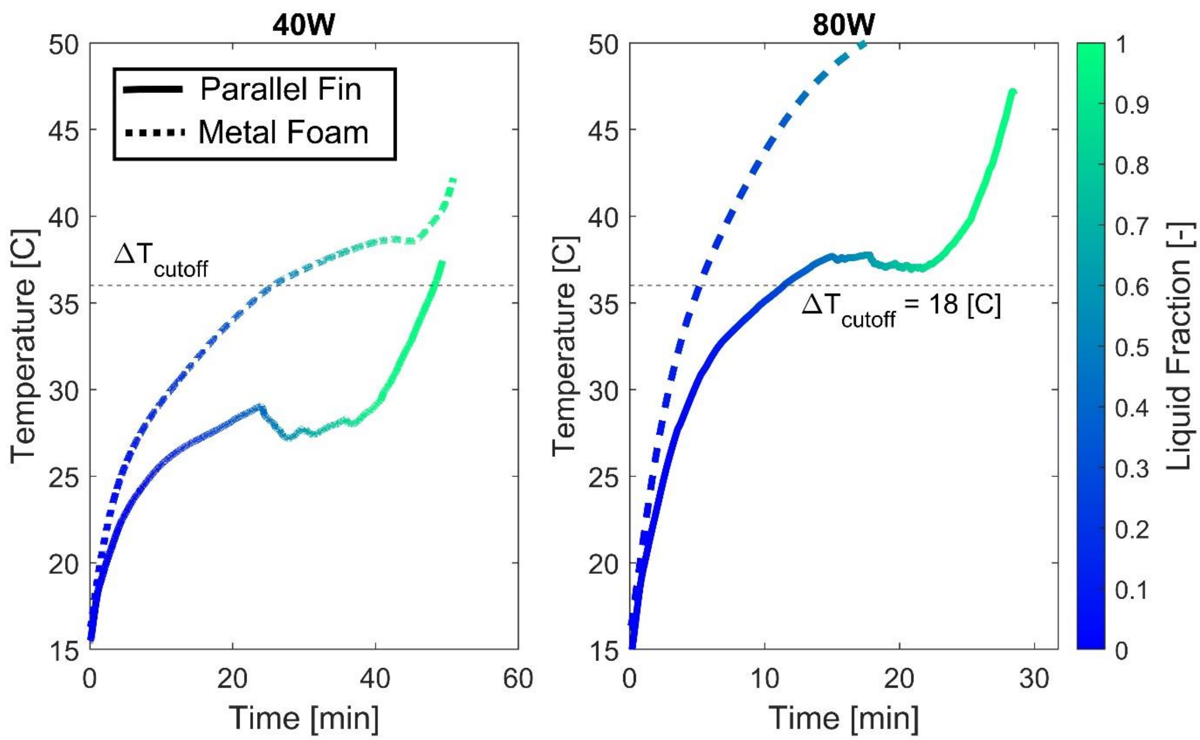

Figure 27: Rate capability curves (temperature vs time) of PFTS and MFTS at 40 and 80 W.

Fig. 27 can be generalized to all possible test conditions across a range of cutoff temperatures, thereby creating a device performance response for an entire field of conditions. To do so, the liquid fraction, or synonymously the storage fraction, was calculated as a function of cutoff temperature and power across the four PFTS geometries and the MFTS. This data is combined with the maximum latent capacity to generate the device utility plot shown in Fig. 28.

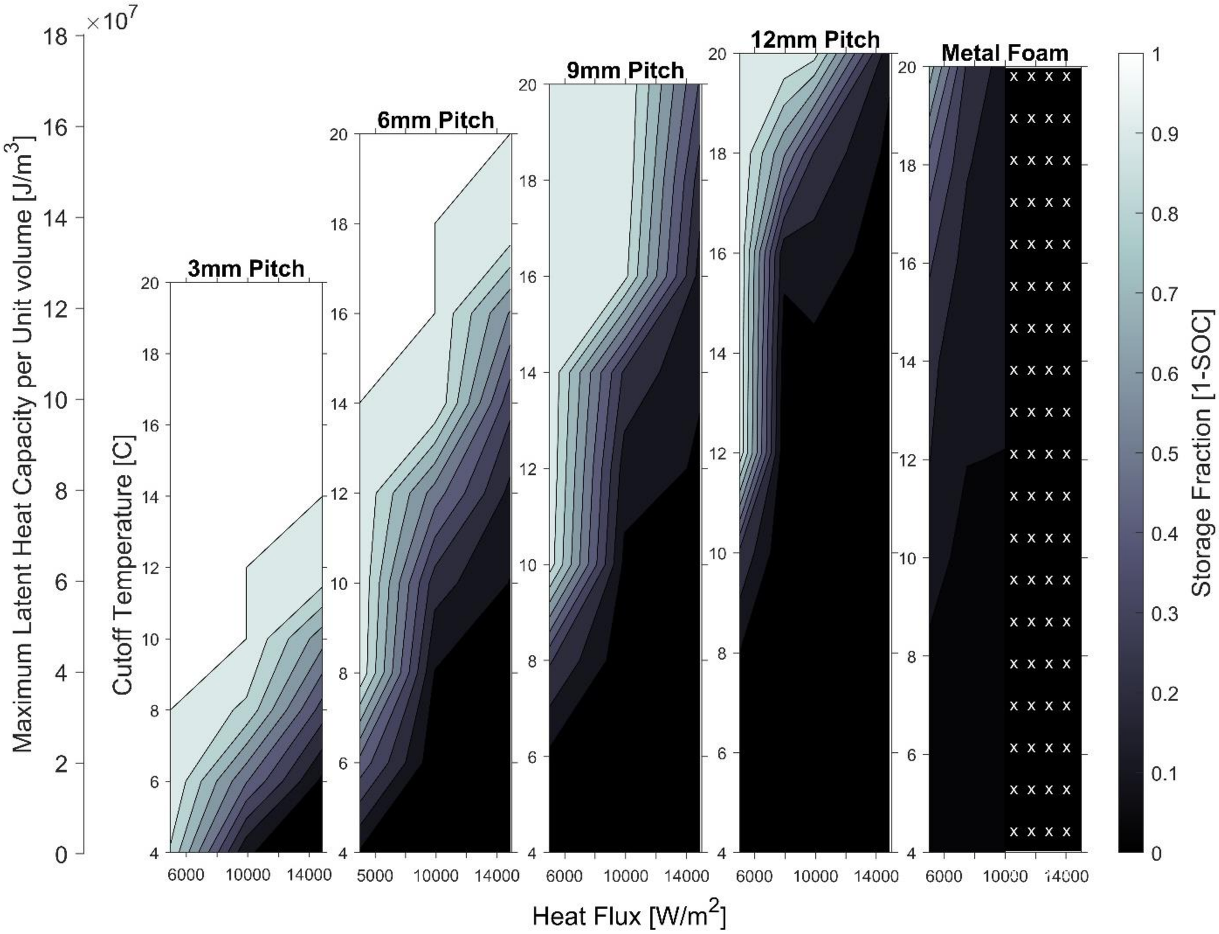

Figure 28: Device utility plot for the PFTS and MFTS devices. It denotes the maximum latent capacity with the bar height, and the achieved storage fraction as a function of power and cutoff temperature with the contour plot inside of the bar. X-marks in the metal foam bar indicate conditions that were not tested but where the storage fraction is inferred.

The device utility plot clearly elucidates the tradeoff between energy capacity – via bar height – and device resilience to power and temperature requirements – via the storage fraction contour. For example, the 3-mm device has the largest portion of design conditions with a storage fraction at one; It is the most resilient to high power and low cutoff temperatures because it has the largest volume of HCM. Consequently, it also has the lowest latent heat capacity per unit volume. The opposite side of the tradeoff is evident in the 12-mm pitch device with low resilience but a high ceiling for energy density. Interestingly, the observed benefits of natural convection associated with increasing pitch never fully offset the detrimental impact of diminished conduction pathways caused by increasing pitch. This is apparent by the absence of a condition set where a higher fin pitch has a higher storage fraction than a lower fin pitch.

As expected from Fig. 27, the metal foam test section performed notably worse than the 12-mm and 9-mm test sections at similar energy capacities. The poor performance could in part be due to weak adhesion between the base plate and the metal foam surface. This would have caused a large temperature gradient between the PCM melt temperature and the base temperature. However, the base temperature profiles in Fig. 27 suggest that the temperature began to severely diverge when natural convection became a significant heat transfer mechanism in the parallel fin device. In addition, the MFTS shows a slower reduction of the rate of temperature rise that is characteristic of natural convection heat transfer in wide channels. Intuitively, the foam structures that disrupt flow and uniformly disperse heat appear to underperform against the parallel fins at volume fractions and heat fluxes that support natural convection dominated melting. It would be worth investigating whether metal foams continue to underperform parallel fins at device geometries and testing conditions where 1-D conduction appropriately captured melting dynamics.

Aside from comparing performance trends, the device utility plot can also be a valuable design tool for sizing PCM heat sinks with understood behaviors. An engineer with access to a device utility plot could quickly determine which device to use for a given heat flux and cutoff temperature by multiplying the storage fraction at that condition by the maximum latent heat capacity per unit volume for a given device. Although if device performance is only important for a single cutoff temperature, a Ragone plot may provide a clearer comparison between devices. Fig. 29 shows a Ragone plot of the PFTS, MFTS, and IFSO devices at a cutoff temperature of 36 ºC (ΔT_{cutoff} = 18 °C).

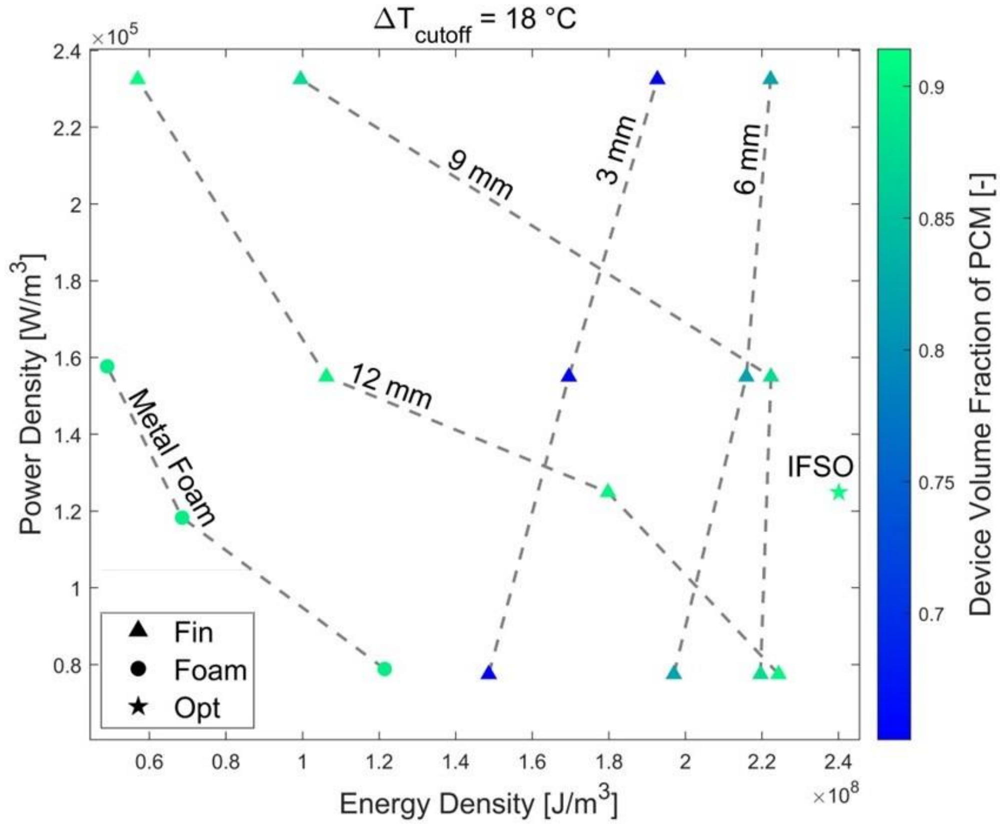

Figure 29: Ragone plot of the PFTS, MFTS, and IFSO device evaluated at a cutoff temperature 18 ºC above the melting temperature (36 ºC for hexadecane).

Fig. 29 compares device performance for a range of power requirements, assuming that the base temperature must remain between the melt temperature and 18 ºC above it. This Ragone plot shows that if the device only needs to operate at very low powers (< 5 kW/m^2), then the largest fin spacing is the best design. However, if the device needs to dissipate a larger range of heat fluxes (4.94 and 14.8 kW/m^2), the 6-mm device is the best option. At lower power densities, the 9-mm and 12-mm devices outperform the 6-mm device but never exceed an improvement greater than 20%, while at higher power densities, they fail to achieve useful energy storage.

It is worth noting that the IFSO device outperformed the 12-mm PF device by 33.6%. This is a far greater increase than the metric used for device improvement in Chapter 5. Additionally, the IFSO has a higher energy density than the 12-mm PF device despite having the same volume fraction of PCM. It is worth noting that the 12-mm PF device never reached a full storage fraction, but also, energy storage is counted as the product of power and the operational time. This means that time when the IFSO had fully melted but maintained base temperatures below the cutoff would count toward its energy density.

Fig. 30 demonstrates the same Ragone plot for a cutoff temperature of 28 ºC (ΔT_{cutoff} = 10 °C). The tighter restriction on base temperature confines the maximum energy density below 2×10^8 J/m^3 (55.6 kW-h/m^3). For this condition, the 3-mm pitch test is the most appropriate for covering the range of power densities at a near-constant energy density. This conclusion agrees with the device utility trends in Fig. 28 with the 3-mm pitch demonstrating resilience to low cutoff temperatures and high power requirements due to its high volume fraction of HCM.

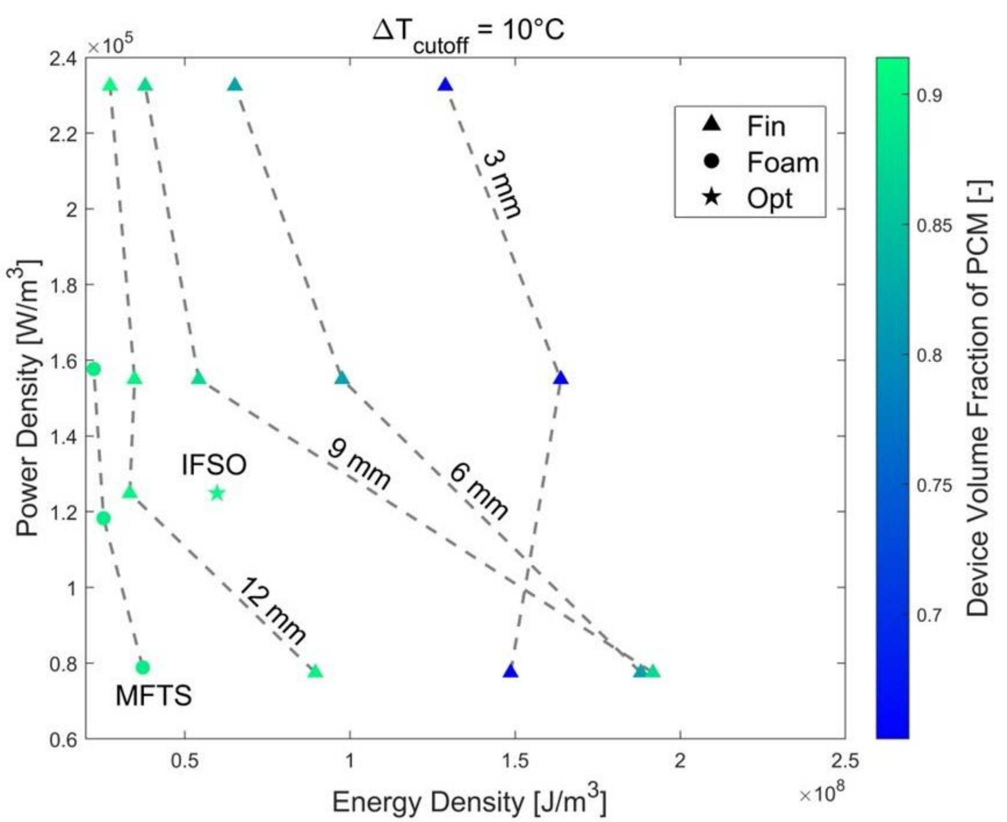

Figure 30: Ragone plot of in-house devices evaluated at a cutoff temperature 10 ºC above the melting temperature (28 ºC).

6.3 Benchmarking Against Surveyed Literature

The experimental tests done in this work were benchmarked against other studies to contextualize where the presented data fits within the larger literature. Ten studies were selected from literature to represent a variety of PCM heat sinks for comparison. Many other papers were considered, but only those that met the following requirements were selected for data processing: 1) The paper must experimentally test PCM devices using a clearly stated constant heat flux boundary condition; 2) the paper must discuss critical characteristics about the device, such as PCM properties, device geometry, and enhancement methods; 3) the paper must provide base temperature profiles over time; and 4) the study must provide some means of estimating the state-of-charge (SOC) or melt rate over time. If a study met these requirements with results relevant to the previous discussions, the base temperature and SOC data were copied into the database.

Plot digitizers were used to record base temperature from available plots. Many studies directly included liquid fraction data, which was also digitized and then converted from liquid fraction to SOC. Fig. 31 and Fig. 32 display side-by-side examples of data extracted from Temel et al and Fu et al, then repurposed into a base temperature and SOC response plot. Many studies, particularly with CCM devices, did not include liquid fraction measurements but included a steady state melting rate. Although it was a less direct measurement, the melting rate was used to estimate the SOC with additional information on when the PCM reached the melting temperature and the total height of the PCM (Fig. 32). This was especially important for determining the duration of the device operation. If a test provided neither liquid fraction nor melting rate data, a linear melting rate was assumed to begin once at least one thermocouple was at the PCM melting temperature. The collection of studies that were used for this paper are shown in Table 6. They are sorted by device and include key features of the study.

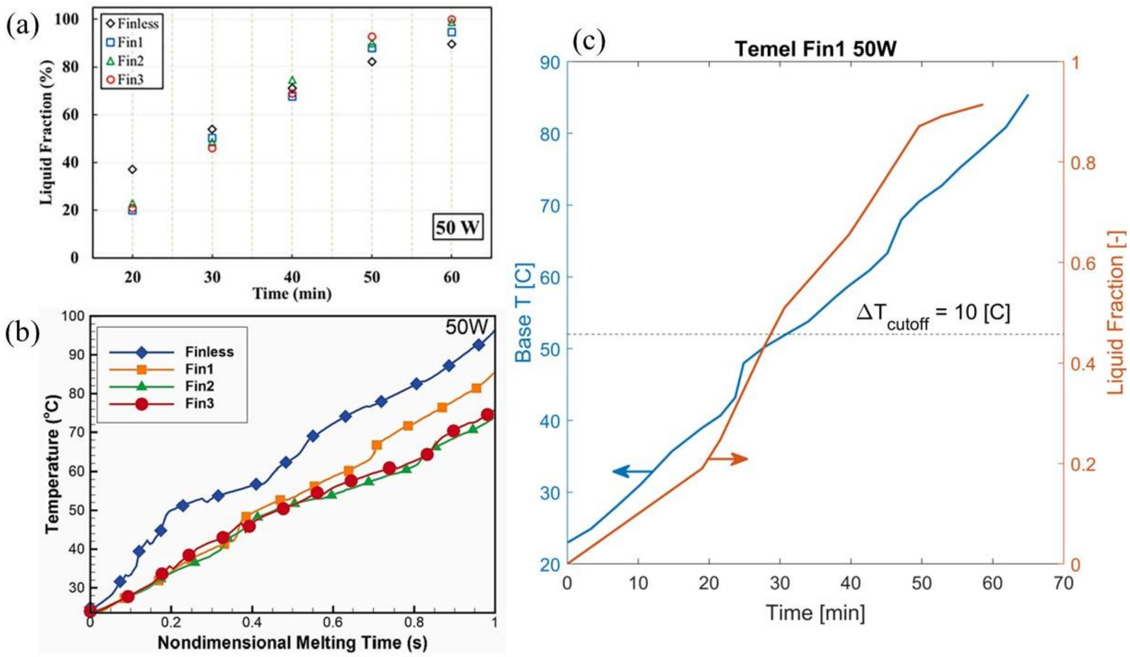

Figure 31: Data collection and manipulation from the study Temel et al (2023) [75]. Plots (a) and (b) show plots of liquid fraction and base temperature directly from the paper. Plot (c) shows base temperature and liquid fraction data refitted into a modified temperature response plot.

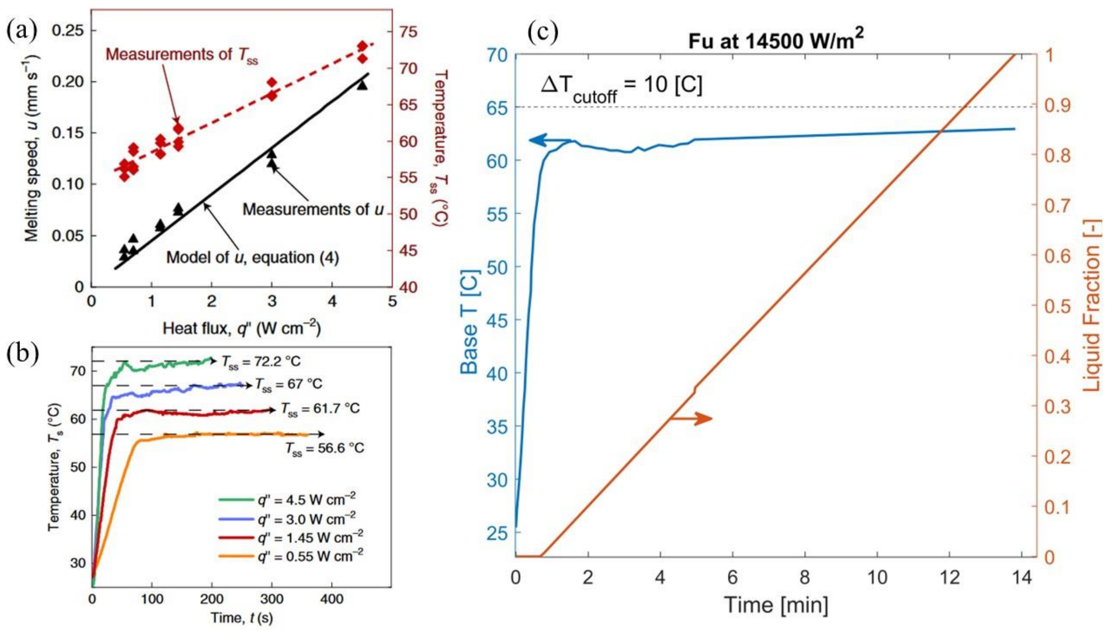

Figure 32: Data collection and manipulation from the study Fu et al (2021) [59]. Plots **(a)** and **(b)** show plots of melt speed and base temperature directly from the paper. Plot **(c)** shows base temperature and liquid fraction data refitted into a modified temperature response plot.

Table 6: List of literature gathered for Ragone analysis

Lead Author	Year published	Device type	Number of tests used	PCM used	Notable features
Joneidi [76]	2019	Fins	3 (varying number of fins)	RT35, Rubitherm T_{melt} = 35 ºC	Small number of fins. Not fully extended to fill height. Low power.
Sodhi [57]	2020	Fins	7 (varying pin fin and power)	PCM 58, Microtech laboratories T_{melt} = 58 ºC	Fins extended beyond PCM fill height for air convection. Different geometry pin fins
Deng [77]	2020	Fins	9 (varying fin number and power)	Lauric Acid T_{melt} = 45 ºC	Fin thickness changed to keep volume fraction fixed with increasing fin count
Temel [75]	2023	Fins	12 (varying fin layout and power)	A42 (PlusICE) T_{melt} = 42 ºC	Heater mounted on the side with fins of different lengths.
Mills [47]	2024	Fins	12 (varying power and orientation)	Coconut oil T_{melt} = 24 ºC	Singular fin with tree-like branches. Small device.
Prout	-	Fins	12 (varying fin pitch and power)	Hexadecane T_{melt} = 18 ºC	Varying effect of natural convection by pitch and power.
Diani [78]	2021	Foam	3 (varying power)	RT42, (Rubitherm) T_{melt} = 43 ºC	Very short test section with copper foam. Varied porosity and PCM.
Singh [79]	2024	Foam	2 (varying power)	n-eisocane T_{melt} = 70 ºC	Experiments used for a numerical parametric Ragone analysis. Short test device.
Prout	-	Foam	3 (varying power)	Hexadecane T_{melt} = 18 ºC	Metal foam adhered to base with thermal epoxy. May be ineffective
Fu [59]	2021	CCM	4 (varying power)	Paraffin T_{melt} = 55 ºC	First instance of DynPCM method. A weight pushes PCM on the heated surface.
He [61]	2023	CCM	5 (varying power)	Paraffin T_{melt} = 55 ºC	Compared paraffin to a low melting point metal alloy.
Stavins [62]	2026	CCM	6 (varying fins and power)	n-Octosocane T_{melt} = 61 ºC	Used small fins with CCM to enhance pressure and heat spreading.

The first benchmark is presented between the PFTS geometries and all other finned HCM studies in Table 6. Fig. 33 shows volumetric energy density plotted against volumetric power density at ΔT_{cutoff} = 10 ºC, where both metrics are normalized against their respective PCM latent heat of fusion (ΔH). This normalization is differentiated from standard density metrics by using the *specific* density qualifier. Fig. 33 shows that the PFTS matches the same design region as all other devices except those from Sodhi et al. Sodhi devices outperformed others because they were only filled with PCM partially up the pin-fin length, creating a hybrid PCM-traditional heat sink. This artificially increased the energy density at high temperature gradients between the outside air and the base by allowing for significant heat removal via natural convection with the ambient environment.

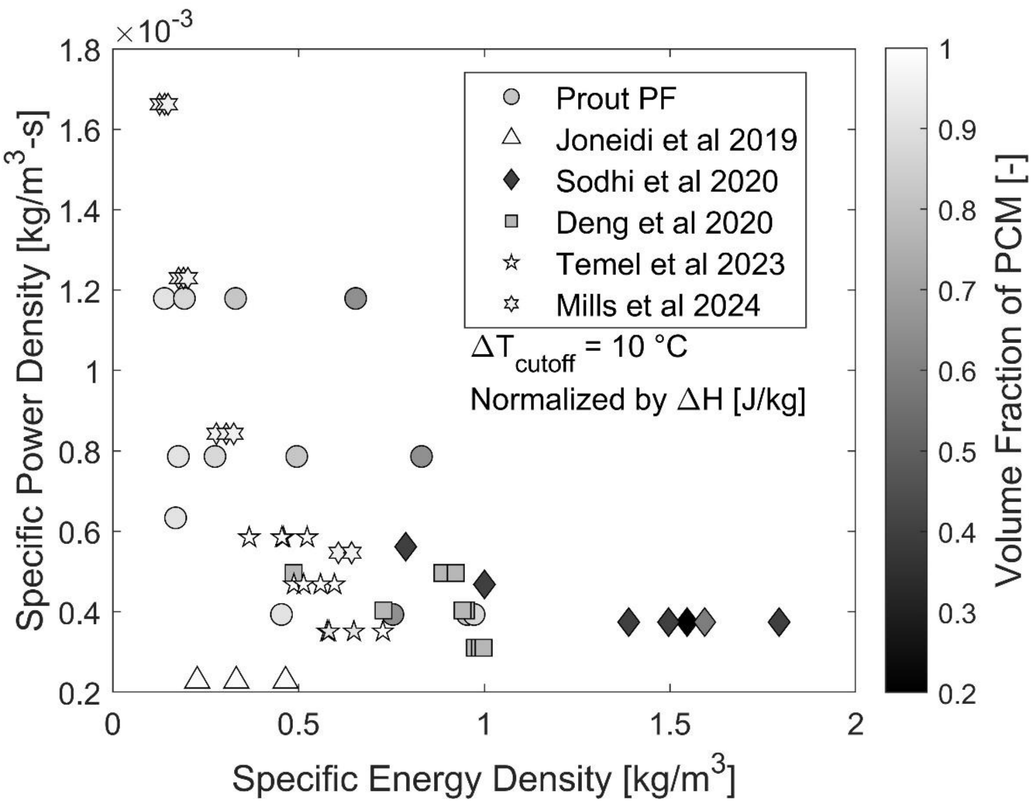

Figure 33: Specific energy density against specific power density, normalized by ΔH, for a selection of finned PCM heat sinks.

Discounting the Sodhi et al study, the PFTS appeared to perform better than most other devices. At high power densities, the 3-mm pitch outperformed Mills et al. Whereas at low power densities, the 9-mm pitch sat near the front of the traditional PCM devices. More data could be gathered for lower PCM volume fractions and higher power densities, but the current data set demonstrates that the PFTS is a well-designed test section with appropriately selected boundary conditions.

The second benchmark observes how the PFTS and MFTS align with other metal foam and CCM studies from Table 6. Metal foam test sections were difficult to collect because authors commonly excluded liquid fraction and base temperature measurements from their results. Meanwhile, CCM is a newer technology with only a small number of groups developing data. Regardless, Fig. 34 shows energy density plotted against power density at a cutoff temperature difference of 10 ºC, both normalized by the respective latent heat of fusion. The PFTS comprises all the fin data shown in Fig. 34.

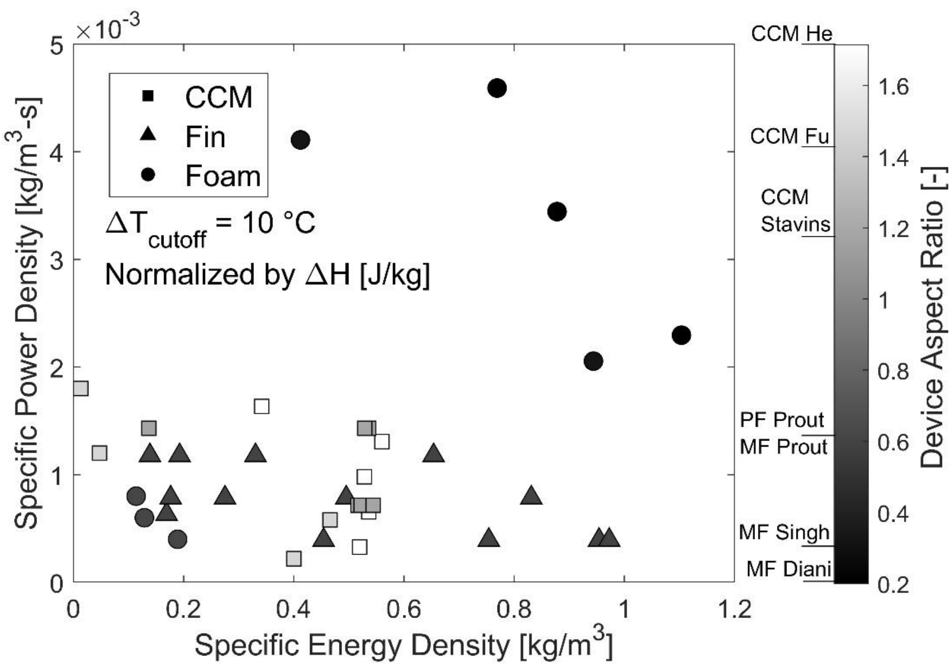

Figure 34: The PFTS benchmarked against available metal foam and CCM papers. The marker color is scaled by the device aspect ratio, defined as device width divided by its height.

From what was observed in Section 4.3, devices that can be treated as effective mediums (such as metal foams [80, 81]) display 1-D melting behavior that causes a base temperature response associated with the length of conduction through the liquid melt front (Eq. 26). Short devices are inherently incapable of developing long liquid melt fronts and therefore can use their full latent capacity with minimal temperature rises. Accordingly, devices with small aspect ratios offer significantly better latent heat utilization at higher heat fluxes, thus increasing their power density.

This is apparent in Fig. 34 with Singh et al and Diani et al outperforming the PFTS and MFTS in specific power density by factors ranging from roughly 2×10^{-3} to 5×10^{-3} kg/m^3-s at comparable specific energy densities. In contrast, the PFTS and CCM devices occupy the same energy and power density region despite the PFTS device having much lower aspect ratios. This is because of the fundamentally different melting mechanism employed by CCM. Results from Fig. **Figure *34***34 suggest that designers should try to maximize the device base area while minimizing height. Although when the base area is significantly constrained, CCM devices may provide a valuable alternative by providing comparable performance at high aspect ratios.

The devices in Fig. 34 can also be compared using a device utility plot, shown in Fig. 35. Here, the 3-mm pitch PFTS is plotted alongside the metal foam test section from Diani et al, along with all the collected CCM devices. As in Fig. 34, the energy capacity is normalized by ΔH, however, power is listed as a heat flux rather than power density, with unique axes for each device.

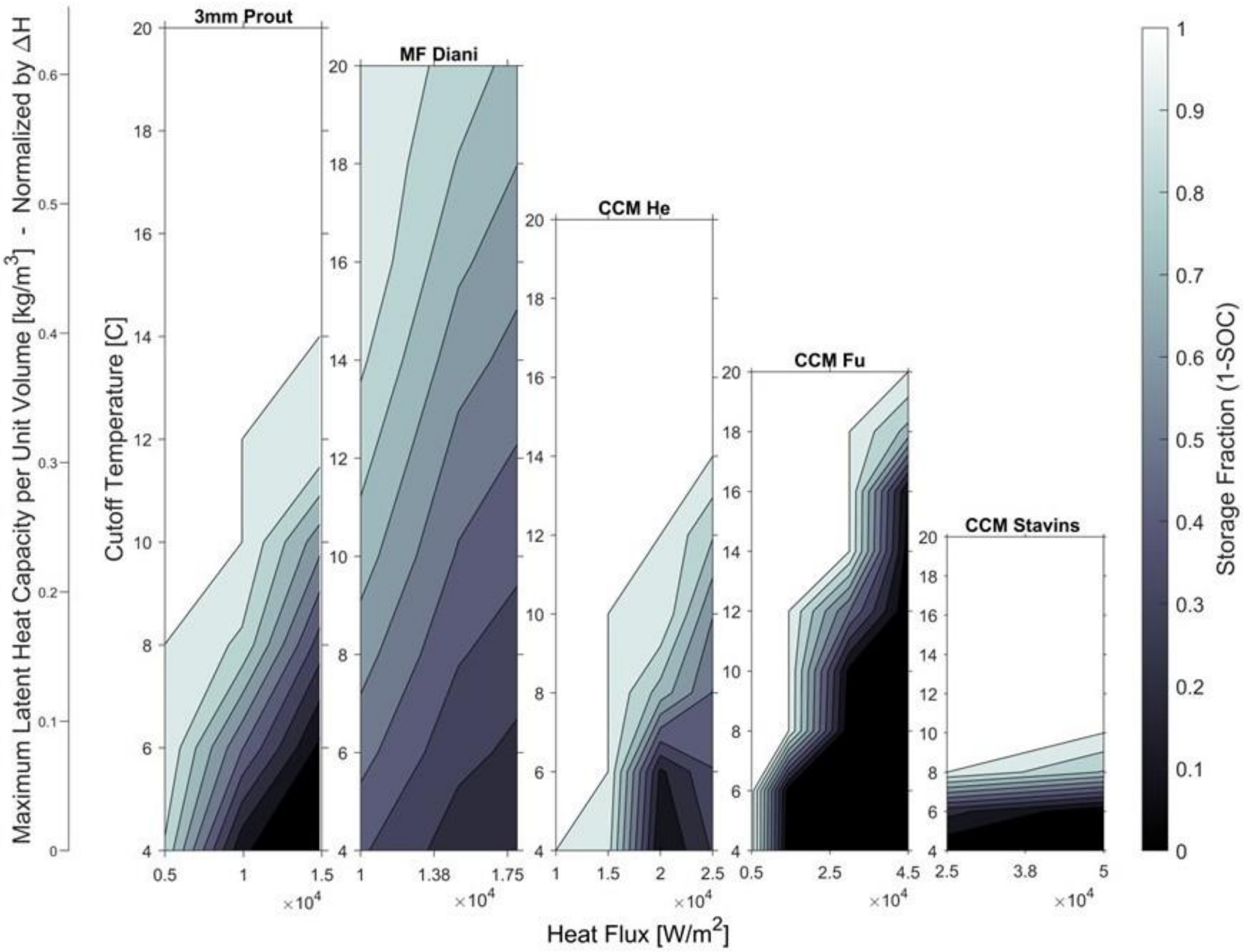

Figure 35: Device utility plot of the 3-mm PFTS alongside other devices from literature. Note that each bar has a unique heat flux range.

With heat flux as the basis for comparison rather than power density, it appears that the 3-mm PFTS has better energy storage utility than the Diani et al device. This is reconciled by the fact that the volume of the PFTS is 72% larger than the Diani et al device, while the PFTS base area is only 81% of the Diani et al device: Smaller volumes at the same heat flux will yield larger volumetric power densities. Fig. 35 also demonstrates the importance of choosing a figure of merit that matches your design goals. For instance, the device utility plot is more insightful to a design case where improving energy capacity at a given heat flux supersedes maximizing energy density.

Storage fraction trends from the right three studies reveals an advantage for CCM devices: powerful temperature regulation at high heat fluxes. This is most evident with the Stavins device achieving full latent utilization at a heat flux of 50 kW/m^2 when the temperature cutoff difference is at 10 ºC. Like the 12-mm PFTS, the major drawback is the diminished maximum energy capacity per unit volume.

Overall, the conducted literature survey positions the PFTS device as a well-designed PCM heat sink with its energy density and power density aligning with other studies. Furthermore, investigating other enhancement methods and geometries signaled that the device aspect ratio is a critical design parameter for maximizing power density for traditional PCM architectures. It should always be considered when comparing results from studies where the aspect ratio is not held constant. Lastly, the CCM architecture displayed excellent resilience to demanding temperature and heat flux constraints while also remaining unaffected by the aspect ratio trends found in traditional PCM devices. Future work on Ragone analysis could systematically map PCM architectures by energy and power density, expand the work to a numerical survey with additional in-house modeling, or consider PCM heat sink performance with reference to other PCM-based technologies.

CHAPTER 7: CONCLUSION

This work explored PCM heat sink design through several complementary perspectives, including (1) fundamental PCM melting behavior, (2) model fidelity, (3) HCM topology optimization, and (4) device-level performance metrics. Throughout these investigations, the tradeoff between energy storage and power capacity has emerged as the central design challenge. By bridging the gap between fundamental melting dynamics and practical optimization methods, this work provides a framework to navigate this tradeoff, ultimately improving PCM-based heat sinks for thermal management.

First, this study discussed the clear trends in the melting behavior of PCM between parallel fins. Most notably, the fin pitch was found to be the primary determiner of melting shape. As the fin pitch increases, the melt front transitions from moving linearly upwards to a 2-D ellipse. Under the combined conditions of a 2-D melt shape and high power levels, liquid PCM exhibited pronounced horizontal temperature gradients that generated density-driven fluid motion. This observation agreed with the introduction of natural-convection enhanced heat transfer. Specifically, the rate of base temperature increase was significantly curtailed at the 9-mm and 12-mm fin pitches, where the maximum PCM velocities were consistently above 2 mm/s.

The transition from 1-D to 2-D melting and its effects on liquid PCM motion also drove the accuracy of the 1-D EMA, 2-D conduction, and 2-D convection model across the experimental conditions. The presence of 2-D melting limited the predictive capabilities of the 1-D EMA model to the 3-mm fin pitch. In contrast, the 2-D convection model showed improved accuracy at conditions where 2-D melting promoted natural convection.

The observations on melting behavior and modeling accuracy motivated an optimization of the 12-mm fin pitch using a conduction-based and convection-based IFSO method. The resulting geometry was experimentally measured to reduce the maximum base temperature by 12.1%. This value agreed with the improvement predicted by the convection model of 12.6%.

Finally, a device-level approach to PCM heat sink characterization was considered for evaluation of the parallel fin, IFSO, and metal foam test sections. Comparing devices based on energy and power density demonstrated that energy capacity is balanced by device resilience even in cases where natural convection is a dominant heat transfer mechanism. A survey of available literature benchmarked the PFTS against a variety of PCM heat sinks. Ragone and device utility plots validated the PFTS design and revealed principals for effective PCM heat sink selection.

Future work investigating PCM heat sink performance could further explore findings from this work. For example, PCM detachment and pressure-induced fluid motion were unexpected phenomena that impacted PCM melting behavior. The models did not capture either of the phenomena, so more work could be done to capture these behaviors in CFD simulations – improving the ability to fully optimize the design.

Additionally, the optimization results discussed in this work motivate continued optimization studies. A primary interest would be to systematically compare the performance of convection and conduction-based solvers in parallel fin optimization problems. Such a study could discern when a conduction-based solver achieves an equivalent design, thereby reducing the computational demands of PCM composite optimization. It could also be of interest to explore how different problem formulations yield different results. Attempting to optimize for increasing operational time below some cutoff temperature or optimize for power and energy density are appealing problem formulations because of their clear connection to the Ragone framework. Adopting these as minimization functions with an experimental facility that allows for a flexible test section geometry could leverage knowledge gained from natural convection enhancement, optimization methods, and the Ragone framework to gain interesting results with their causes clearly grounded in the power versus energy capacity tradeoff. Lastly, the Ragone analysis herein was mainly exploratory, although it does incentivize a deeper dive into device-level PCM design principles or broader comparisons of PCM.

REFERENCES

[1] A. Datas, A. Ramos, A. Martí, C. Del Cañizo, and A. Luque, “Ultra high temperature latent heat energy storage and thermophotovoltaic energy conversion,” *Energy*, vol. 107, pp. 542–549, Jul. 2016, doi: 10.1016/j.energy.2016.04.048.

[2] A. Mavrigiannaki and E. Ampatzi, “Latent heat storage in building elements: A systematic review on properties and contextual performance factors,” *Renew. Sustain. Energy Rev.*, vol. 60, pp. 852–866, Jul. 2016, doi: 10.1016/j.rser.2016.01.115.

[3] Z. Ling *et al.*, “Review on thermal management systems using phase change materials for electronic components, Li-ion batteries and photovoltaic modules,” *Renew. Sustain. Energy Rev.*, vol. 31, pp. 427–438, Mar. 2014, doi: 10.1016/j.rser.2013.12.017.

[4] X. Yan, B. Xie, and C. Li, “Phase change materials for aerospace,” *Renew. Sustain. Energy Rev.*, vol. 226, p. 116230, Jan. 2026, doi: 10.1016/j.rser.2025.116230.

[5] K. W. Shah, “A review on enhancement of phase change materials - A nanomaterials perspective,” *Energy Build.*, vol. 175, pp. 57–68, Sep. 2018, doi: 10.1016/j.enbuild.2018.06.043.

[6] A. Sarı and A. Karaipekli, “Thermal conductivity and latent heat thermal energy storage characteristics of paraffin/expanded graphite composite as phase change material,” *Appl. Therm. Eng.*, vol. 27, no. 8–9, pp. 1271–1277, Jun. 2007, doi: 10.1016/j.applthermaleng.2006.11.004.

[7] C. Y. Zhao and Z. G. Wu, “Heat transfer enhancement of high temperature thermal energy storage using metal foams and expanded graphite,” *Sol. Energy Mater. Sol. Cells*, vol. 95, no. 2, pp. 636–643, Feb. 2011, doi: 10.1016/j.solmat.2010.09.032.

[8] Y. Li, Z. Fu, M. Xue, Z. Shao, Y. Li, and Q. Zhu, “Experimental study on preparation and thermal storage properties of expanded graphite/paraffin wax as a shape-stabilized phase change material,” *Energy Rep.*, vol. 8, pp. 324–331, Nov. 2022, doi: 10.1016/j.egyr.2022.09.149.

[9] A. Mallow, O. Abdelaziz, and S. Graham, “Thermal charging study of compressed expanded natural graphite/phase change material composites,” *Carbon*, vol. 109, pp. 495–504, Nov. 2016, doi: 10.1016/j.carbon.2016.08.030.

[10] A. Islam, A. K. Pandey, R. Saidur, B. Aljafari, and V. V. Tyagi, “Advancements in foam-based phase change materials: Unveiling leakage control, enhanced thermal conductivity, and promising applications,” *J. Energy Storage*, vol. 74, p. 109380, Dec. 2023, doi: 10.1016/j.est.2023.109380.

[11] Z. Maqbool, M. Hanief, and M. Parveez, “Review on performance enhancement of phase change material based heat sinks in conjugation with thermal conductivity enhancers for electronic cooling,” *J. Energy Storage*, vol. 60, p. 106591, Apr. 2023, doi: 10.1016/j.est.2022.106591.

[12] H. A. Al-Salami, N. S. Dhaidan, H. H. Abbas, F. N. Al-Mousawi, and R. Z. Homod, “Review of PCM charging in latent heat thermal energy storage systems with fins,” *Therm. Sci. Eng. Prog.*, vol. 51, p. 102640, Jun. 2024, doi: 10.1016/j.tsep.2024.102640.

[13] A. P. Wemhoff and A. J. Webb, “Investigation of nanoparticle agglomeration on the effective thermal conductivity of a composite material,” *Int. J. Heat Mass Transf.*, vol. 97, pp. 432–438, Jun. 2016, doi: 10.1016/j.ijheatmasstransfer.2016.02.027.

[14] A. Hoe, M. Deckard, A. Tamraparni, A. Elwany, J. R. Felts, and P. J. Shamberger, “Conductive heat transfer in lamellar phase change material composites,” *Appl. Therm. Eng.*, vol. 178, p. 115553, Sep. 2020, doi: 10.1016/j.applthermaleng.2020.115553.

[15] M. Al-Jethelah, S. Ebadi, K. Venkateshwar, S. H. Tasnim, S. Mahmud, and A. Dutta, “Charging nanoparticle enhanced bio-based PCM in open cell metallic foams: An experimental investigation,” *Appl. Therm. Eng.*, vol. 148, pp. 1029–1042, Feb. 2019, doi: 10.1016/j.applthermaleng.2018.11.121.

[16] Q. Ren, H. Xu, and Z. Luo, “PCM charging process accelerated with combination of optimized triangle fins and nanoparticles,” *Int. J. Therm. Sci.*, vol. 140, pp. 466–479, Jun. 2019, doi: 10.1016/j.ijthermalsci.2019.03.005.

[17] D. Cheneler and A. R. Kennedy, “A comparison of the manufacture and mechanical performance of porous aluminium and aluminium syntactic foams made by vacuum-assisted casting,” *Mater. Sci. Eng. A*, vol. 789, p. 139528, Jul. 2020, doi: 10.1016/j.msea.2020.139528.

[18] Q. Wang, D. Zhou, Y. Chen, P. Eames, and Z. Wu, “Characterization and effects of thermal cycling on the properties of paraffin/expanded graphite composites,” *Renew. Energy*, vol. 147, pp. 1131–1138, Mar. 2020, doi: 10.1016/j.renene.2019.09.091.

[19] S. Zheng *et al.*, “Enhancing latent heat storage devices: A thermodynamic and thermo-economic assessment into metal fins, metal foam, and expanded graphite,” *J. Energy Storage*, vol. 98, p. 112932, Sep. 2024, doi: 10.1016/j.est.2024.112932.

[20] J. Soto, M. Jadal, N. De Guyenro, and D. Delaunay, “Thermal cycling aging of encapsulated phase change material – Compressed expanded natural graphite composite,” *Therm. Sci. Eng. Prog.*, vol. 22, p. 100836, May 2021, doi: 10.1016/j.tsep.2020.100836.

[21] J. Wu and Z. Wu, “Experimental comparison of latent thermal energy storage units with different metal macro-additives,” *Appl. Therm. Eng.*, vol. 216, p. 119089, Nov. 2022, doi: 10.1016/j.applthermaleng.2022.119089.

[22] A. H. F. Theeb and I. Y. Hussain, “Numerical simulation of thermal performance of heat sink augmented with phase change material PCM integrated with solid and aluminum metal foam fins,” *Heat Transf.*, p. htj.23113, Jun. 2024, doi: 10.1002/htj.23113.

[23] Z.-R. Li, S. Baghaei Oskouei, G.-T. Fu, Ö. Bayer, and L.-W. Fan, “Enhanced power density during energy charging of a shell-and-tube thermal storage unit: Comparison between the inclusion of metal fins and foams,” *J. Energy Storage*, vol. 55, p. 105576, Nov. 2022, doi: 10.1016/j.est.2022.105576.

[24] V. Joshi and M. K. Rathod, “Experimental and numerical assessments of thermal transport in fins and metal foam infused latent heat thermal energy storage systems: A comparative evaluation,” *Appl. Therm. Eng.*, vol. 178, p. 115518, Sep. 2020, doi: 10.1016/j.applthermaleng.2020.115518.

[25] Z. Du, G. Liu, X. Huang, T. Xiao, X. Yang, and Y.-L. He, “Numerical studies on a fin-foam composite structure towards improving melting phase change,” *Int. J. Heat Mass Transf.*, vol. 208, p. 124076, Jul. 2023, doi: 10.1016/j.ijheatmasstransfer.2023.124076.

[26] M. E. Zayed *et al.*, “Recent progress in phase change materials storage containers: Geometries, design considerations and heat transfer improvement methods,” *J. Energy Storage*, vol. 30, p. 101341, Aug. 2020, doi: 10.1016/j.est.2020.101341.

[27] V. Safari, B. Kamkari, N. Hewitt, and K. Hooman, “Experimental comparative study on thermal performance of latent heat storage tanks with pin, perforated, and rectangular fins at different orientations,” *Therm. Sci. Eng. Prog.*, vol. 48, p. 102401, Feb. 2024, doi: 10.1016/j.tsep.2024.102401.

[28] S. F. Hosseinizadeh, F. L. Tan, and S. M. Moosania, “Experimental and numerical studies on performance of PCM-based heat sink with different configurations of internal fins,” *Appl. Therm. Eng.*, vol. 31, no. 17–18, pp. 3827–3838, Dec. 2011, doi: 10.1016/j.applthermaleng.2011.07.031.

[29] C. Zhao, J. Wang, Y. Sun, S. He, and K. Hooman, “Fin design optimization to enhance PCM melting rate inside a rectangular enclosure,” *Appl. Energy*, vol. 321, p. 119368, Sep. 2022, doi: 10.1016/j.apenergy.2022.119368.

[30] I. Jmal and M. Baccar, “Numerical investigation of PCM solidification in a finned rectangular heat exchanger including natural convection,” *Int. J. Heat Mass Transf.*, vol. 127, pp. 714–727, Dec. 2018, doi: 10.1016/j.ijheatmasstransfer.2018.08.058.

[31] C. Ji, Z. Qin, S. Dubey, F. H. Choo, and F. Duan, “Simulation on PCM melting enhancement with double-fin length arrangements in a rectangular enclosure induced by natural convection,” *Int. J. Heat Mass Transf.*, vol. 127, pp. 255–265, Dec. 2018, doi: 10.1016/j.ijheatmasstransfer.2018.07.118.

[32] V. Shatikian, G. Ziskind, and R. Letan, “Numerical investigation of a PCM-based heat sink with internal fins,” *Int. J. Heat Mass Transf.*, vol. 48, no. 17, pp. 3689–3706, Aug. 2005, doi: 10.1016/j.ijheatmasstransfer.2004.10.042.

[33] “Water Resources Research - 2015 - Ghanbarian - Thermal conductivity in porous media Percolation-based effective-medium.pdf.”

[34] J. Woods, A. Mahvi, A. Goyal, E. Kozubal, A. Odukomaiya, and R. Jackson, “Rate capability and Ragone plots for phase change thermal energy storage,” *Nat. Energy*, vol. 6, no. 3, pp. 295–302, Feb. 2021, doi: 10.1038/s41560-021-00778-w.

[35] A. Singh, S. Rangarajan, and B. G. Sammakia, “A novel framework to design phase change material composite for cooling of electronic devices,” in *2024 23rd IEEE Intersociety Conference on Thermal and Thermomechanical Phenomena in Electronic*

Systems (ITherm), Aurora, CO, USA: IEEE, May 2024, pp. 1–8. doi: 10.1109/itherm55375.2024.10709475.

[36] N. James, A. Mahvi, and J. Woods, "Optimizing phase change composite thermal energy storage using the thermal Ragone framework," *J. Energy Storage*, vol. 56, p. 105875, Dec. 2022, doi: 10.1016/j.est.2022.105875.

[37] M. T. Barako, S. Lingamneni, J. S. Katz, T. Liu, K. E. Goodson, and J. Tice, "Optimizing the design of composite phase change materials for high thermal power density," *J. Appl. Phys.*, vol. 124, no. 14, p. 145103, Oct. 2018, doi: 10.1063/1.5031914.

[38] A. Tamraparni *et al.*, "Design and Optimization of Lamellar Phase Change Composites for Thermal Energy Storage," *Adv. Eng. Mater.*, vol. 23, no. 1, p. 2001052, Jan. 2021, doi: 10.1002/adem.202001052.

[39] T. Bauer, "Approximate analytical solutions for the solidification of PCMs in fin geometries using effective thermophysical properties," *Int. J. Heat Mass Transf.*, vol. 54, no. 23–24, pp. 4923–4930, Nov. 2011, doi: 10.1016/j.ijheatmasstransfer.2011.07.004.

[40] J. Vogel, J. Felbinger, and M. Johnson, "Natural convection in high temperature flat plate latent heat thermal energy storage systems," *Appl. Energy*, vol. 184, pp. 184–196, Dec. 2016, doi: 10.1016/j.apenergy.2016.10.001.

[41] J. Vogel and M. Johnson, "Natural convection during melting in vertical finned tube latent thermal energy storage systems," *Appl. Energy*, vol. 246, pp. 38–52, Jul. 2019, doi: 10.1016/j.apenergy.2019.04.011.

[42] H. M. Ali *et al.*, "Thermal management of electronics: An experimental analysis of triangular, rectangular and circular pin-fin heat sinks for various PCMs," *Int. J. Heat Mass Transf.*, vol. 123, pp. 272–284, Aug. 2018, doi: 10.1016/j.ijheatmasstransfer.2018.02.044.

[43] H. Pan, X. Liu, Q. Yang, H. Xu, and D. Xu, "Three-dimensional Lattice Boltzmann study on structure optimization and heat dissipation performance of pin-fin heat sink integrated with phase change material," *J. Energy Storage*, vol. 71, p. 108233, Nov. 2023, doi: 10.1016/j.est.2023.108233.

[44] N. B. Khedher, M. Ghalambaz, A. S. Alghawli, A. Hajjar, M. Sheremet, and S. A. M. Mehryan, “Study of tree-shaped optimized fins in a heat sink filled by solid-solid nanocomposite phase change material,” *Int. Commun. Heat Mass Transf.*, vol. 136, p. 106195, Jul. 2022, doi: 10.1016/j.icheatmasstransfer.2022.106195.

[45] Z. Guo, L. Xu, F. Sun, and S. Sun, “Experimental Investigation on Heat Transfer Enhancement of Phase Change Materials by Fractal Fins,” *Energies*, vol. 17, no. 11, p. 2657, May 2024, doi: 10.3390/en17112657.

[46] A. Shukla, K. Kant, P. H. Biwole, R. Pitchumani, and A. Sharma, “Melting and solidification of a phase change material with constructal tree-shaped fins for thermal energy storage,” *J. Energy Storage*, vol. 53, p. 105158, Sep. 2022, doi: 10.1016/j.est.2022.105158.

[47] T. Mills, K. Venkateshwar, S. H. Tasnim, and S. Mahmud, “Numerical and experimental investigation of the melting of a PCM in an enclosure having a tree-shaped internal fin,” *Therm. Sci. Eng. Prog.*, vol. 48, p. 102434, Feb. 2024, doi: 10.1016/j.tsep.2024.102434.

[48] A. Pizzolato, A. Sharma, K. Maute, A. Sciacovelli, and V. Verda, “Design of effective fins for fast PCM melting and solidification in shell-and-tube latent heat thermal energy storage through topology optimization,” *Appl. Energy*, vol. 208, pp. 210–227, Dec. 2017, doi: 10.1016/j.apenergy.2017.10.050.

[49] A.-C. Iradukunda, A. Vargas, D. Huitink, and D. Lohan, “Transient thermal performance using phase change material integrated topology optimized heat sinks,” *Appl. Therm. Eng.*, vol. 179, p. 115723, Oct. 2020, doi: 10.1016/j.applthermaleng.2020.115723.

[50] Q. Y. Yao, C. Y. Zhao, Y. Zhao, H. Wang, and W. Li, “Topology optimization for heat transfer enhancement in latent heat storage,” *Int. J. Therm. Sci.*, vol. 159, p. 106578, Jan. 2021, doi: 10.1016/j.ijthermalsci.2020.106578.

[51] J. Y. Ho, Y. S. See, K. C. Leong, and T. N. Wong, “An experimental investigation of a PCM-based heat sink enhanced with a topology-optimized tree-like structure,” *Energy Convers. Manag.*, vol. 245, p. 114608, Oct. 2021, doi: 10.1016/j.enconman.2021.114608.

[52] S. Lee, H. Choi, P. Park, S. Kang, K. Choi, and H. Lee, “Investigation of enhanced PCM heat sink design under extreme thermal conditions for high-heat-generating electronic

devices," *Int. Commun. Heat Mass Transf.*, vol. 159, p. 108050, Dec. 2024, doi: 10.1016/j.icheatmasstransfer.2024.108050.

[53] A. Briache, A. Afass, M. Ouardouz, M. Ahachad, and M. Mahdaoui, "A Comparative Analysis of Enhancement Techniques in a PCM-Embedded Heat Sink: Fin forms, Nanoparticles, and Metal Foam," *Int. J. Heat Mass Transf.*, vol. 229, p. 125730, Sep. 2024, doi: 10.1016/j.ijheatmasstransfer.2024.125730.

[54] M. Pourfallah and E. Languri, "Experimental analysis on thermal performance of multi-scale metal foam and PCM composite in a rectangular chamber," *Therm. Sci. Eng. Prog.*, vol. 66, p. 104075, Oct. 2025, doi: 10.1016/j.tsep.2025.104075.

[55] H. Wang, F. Wang, Z. Li, Y. Tang, B. Yu, and W. Yuan, "Experimental investigation on the thermal performance of a heat sink filled with porous metal fiber sintered felt/paraffin composite phase change material," *Appl. Energy*, vol. 176, pp. 221–232, Aug. 2016, doi: 10.1016/j.apenergy.2016.05.050.

[56] Z. Wang, Z. Zhang, L. Jia, and L. Yang, "Paraffin and paraffin/aluminum foam composite phase change material heat storage experimental study based on thermal management of Li-ion battery," *Appl. Therm. Eng.*, vol. 78, pp. 428–436, Mar. 2015, doi: 10.1016/j.applthermaleng.2015.01.009.

[57] G. S. Sodhi, C. Botting, E. Lau, M. Palanisamy, M. Rouhani, and M. Bahrami, "Hybrid heat sinks for thermal management of PASSIVELY COOLED battery chargers," *Int. J. Energy Res.*, vol. 45, no. 4, pp. 6333–6349, Mar. 2021, doi: 10.1002/er.6260.

[58] X. Huang, Z. Du, Z. Liu, X. Yang, and B. Sundén, "Research progress of fin design in latent heat energy storage enhancement technology," *Appl. Therm. Eng.*, vol. 278, p. 127157, Nov. 2025, doi: 10.1016/j.applthermaleng.2025.127157.

[59] W. Fu, X. Yan, Y. Gurumukhi, V. S. Garimella, W. P. King, and N. Miljkovic, "High power and energy density dynamic phase change materials using pressure-enhanced close contact melting," *Nat. Energy*, vol. 7, no. 3, pp. 270–280, Mar. 2022, doi: 10.1038/s41560-022-00986-y.

[60] I. Salman *et al.*, “Practical realization and full cycle performance of an ‘hourglass’ system for transient thermal management based on dynamic melting,” *Int. J. Heat Mass Transf.*, vol. 257, p. 128250, Apr. 2026, doi: 10.1016/j.ijheatmasstransfer.2025.128250.

[61] J. He, W. Chu, and Q. Wang, “Experimental study on pressure-enhanced close contact melting with PCMs for stable temperature control of high heat flux electronic devices,” *Appl. Therm. Eng.*, vol. 230, p. 120707, Jul. 2023, doi: 10.1016/j.applthermaleng.2023.120707.

[62] R. A. Stavins *et al.*, “Experimental and numerical exploration of dynamic phase change materials on rectangular strip fins,” *Int. J. Heat Mass Transf.*, vol. 256, p. 127950, Mar. 2026, doi: 10.1016/j.ijheatmasstransfer.2025.127950.

[63] K. Yazawa, P. J. Shamberger, and T. S. Fisher, “Ragone Relations for Thermal Energy Storage Technologies,” *Front. Mech. Eng.*, vol. 5, p. 29, Jun. 2019, doi: 10.3389/fmech.2019.00029.

[64] R. A. Kishore *et al.*, “Experimental characterization and analysis of phase change material-based thermal energy storage system for refrigerated display case,” *Energy Convers. Manag.*, vol. 353, p. 121143, Apr. 2026, doi: 10.1016/j.enconman.2026.121143.

[65] L. Liu, C. Gong, B. Tian, and S. Shao, “Numerical investigation on thermal rate capability and Ragone plots of thermal energy storage device,” *Int. Commun. Heat Mass Transf.*, vol. 172, p. 110472, Mar. 2026, doi: 10.1016/j.icheatmasstransfer.2025.110472.

[66] P. J. Shamberger and T. S. Fisher, “Cooling power and characteristic times of composite heatsinks and insulants,” *Int. J. Heat Mass Transf.*, vol. 117, pp. 1205–1215, Feb. 2018, doi: 10.1016/j.ijheatmasstransfer.2017.10.085.

[67] I. Beyers, A. Bensmann, and R. Hanke-Rauschenbach, “Ragone plots revisited: A review of methodology and application across energy storage technologies,” *J. Energy Storage*, vol. 73, p. 109097, Dec. 2023, doi: 10.1016/j.est.2023.109097.

[68] M. Hamdi, M. Havet, O. Rouaud, and D. Tarlet, “Comparison of different tracers for PIV measurements in EHD airflow,” *Exp. Fluids*, vol. 55, no. 4, p. 1702, Apr. 2014, doi: 10.1007/s00348-014-1702-z.

[69] W. Thielicke and E. J. Stamhuis, “PIVlab – Towards User-friendly, Affordable and Accurate Digital Particle Image Velocimetry in MATLAB,” *J. Open Res. Softw.*, vol. 2, Oct. 2014, doi: 10.5334/jors.bl.

[70] A. D. Brent, V. R. Voller, and K. J. Reid, “ENTHALPY-POROSITY TECHNIQUE FOR MODELING CONVECTION-DIFFUSION PHASE CHANGE: APPLICATION TO THE MELTING OF A PURE METAL,” *Numer. Heat Transf.*, vol. 13, no. 3, pp. 297–318, Apr. 1988, doi: 10.1080/10407788808913615.

[71] N. R. Sgreva *et al.*, “Thermo-physical characterization of Hexadecane during the solid/liquid phase change,” *Thermochim. Acta*, vol. 710, p. 179180, 2022, doi: https://doi.org/10.1016/j.tca.2022.179180.

[72] X.-Q. Wang, C. Yap, and A. S. Mujumdar, “A parametric study of phase change material (PCM)-based heat sinks,” *Int. J. Therm. Sci.*, vol. 47, no. 8, pp. 1055–1068, Aug. 2008, doi: 10.1016/j.ijthermalsci.2007.07.016.

[73] A. Laouer, K. Al-Farhany, M. F. Al-Dawody, and A. L. Hashem, “A numerical study of phase change material melting enhancement in a horizontal rectangular enclosure with vertical triple fins,” *Int. Commun. Heat Mass Transf.*, vol. 137, p. 106223, Oct. 2022, doi: 10.1016/j.icheatmasstransfer.2022.106223.

[74] T. L. Bergman, A. S. Lavine, F. P. Incropera, and D. P. DeWitt, *Introduction to Heat Transfer*. Wiley, 2011. [Online]. Available: https://books.google.com/books?id=YBaNaLurTD4C

[75] U. N. Temel and F. Kilinc, “Experimental investigation of variable fin length on melting performance in a rectangular enclosure containing phase change material,” *Int. Commun. Heat Mass Transf.*, vol. 142, p. 106658, Mar. 2023, doi: 10.1016/j.icheatmasstransfer.2023.106658.

[76] M. H. Joneidi, M. Rahimi, R. Pakrouh, and R. Bahrampoury, “Experimental analysis of Transient melting process in a horizontal cavity with different configurations of fins,” *Renew. Energy*, vol. 145, pp. 2451–2462, Jan. 2020, doi: 10.1016/j.renene.2019.07.114.

[77] Z. Deng, C. Zhang, Q. Sun, L. Wu, F. Yao, and D. Xu, “Experimental study on melting performance of phase change material-based finned heat sinks by a comprehensive

evaluation," *J. Therm. Anal. Calorim.*, vol. 144, no. 3, pp. 869–882, May 2021, doi: 10.1007/s10973-020-09508-y.

[78] A. Diani, L. Moro, and L. Rossetto, "Melting of Paraffin Waxes Embedded in a Porous Matrix Made by Additive Manufacturing," *Appl. Sci.*, vol. 11, no. 12, p. 5396, Jun. 2021, doi: 10.3390/app11125396.

[79] A. Singh, S. Rangarajan, and B. Sammakia, "Utilizing Ragone framework for optimized phase change material-based heat sink design in electronic cooling applications," *Int. J. Heat Mass Transf.*, vol. 227, p. 125518, Aug. 2024, doi: 10.1016/j.ijheatmasstransfer.2024.125518.

[80] H. F. Abbasov, "The Effective Thermal Conductivity of Composite Phase Change Materials with Open-Cellular Metal Foams," *Int. J. Thermophys.*, vol. 41, no. 12, p. 164, Dec. 2020, doi: 10.1007/s10765-020-02747-z.

[81] "Intl J of Energy Research - 2022 - Saxena - A theoretical model for effective thermal conductivity of open-cell-coated.pdf."

APPENDIX A: EMA MODELING APPROACH

The EMA model employed the Euler approach to compute local enthalpy and temperature as functions of time. Energy balances for PCM composite nodes are provided in Eq. 30-32. Notably, Eq. 30 includes a fin contact resistance, which governs the temperature difference between the final base node and the first PCM composite node. Enthalpy values were then converted to temperature using an effective enthalpy-temperature relation that varies with HCM volume fraction. Examples of this relation for different fin pitches are shown in Fig. 36.

$$\frac{dh_1}{dt} = \frac{2k_{eff}}{\rho_{eff}\,\Delta x^2}(T_2 - T_1) + \frac{2A_{fin}}{\rho_{eff}\,A_{base}\,\Delta x\,R''_{c,fin}}(T_{base} - T_1) \tag{30}$$

$$\frac{dh_j}{dt} = \frac{k_{eff}}{\rho_{eff}\Delta x^2}\left(T_{j-1} + T_{j+1} - 2T_j\right) \tag{31}$$

$$\frac{dh_n}{dt} = \frac{2k_{eff}}{\rho_{eff}\,\Delta x^2}(T_{n-1} - T_n) \tag{32}$$

Energy balances for the base nodes are provided in Eq. 33-36. These equations do not use an enthalpy temperature relation but instead use a constant specific heat capacity of 900 J/kg-K for 6061 aluminum. Depending on the boundary condition type, either base temperature data or heat flux data is provided for each timestep in the simulation so that the following equations can be solved.

$$T_{bc} = T_{base,1} + \frac{\dot{q_{bc}} R''_{c,base}}{A_{base}} \tag{33}$$

$$\frac{dT_{base,1}}{dt} = \frac{2\dot{q_{bc}}}{\rho_{HCM}\Delta x c_{HCM} A_{base}} + \frac{2K_{HCM}\rho_{HCM}}{\Delta x^2 c_{HCM}}\left(T_{base,2} - T_{base,1}\right) \tag{34}$$

$$\frac{dT_{base,j}}{dt} = \frac{k_{HCM}}{\rho_{HCM}\Delta x^2 c_{HCM}}\left(T_{base,j-1} + T_{base,j+1} - 2T_{base,j}\right) \tag{35}$$

$$\frac{dh_n}{dt} = \frac{2k_{eff}}{\rho_{eff}\Delta x^2}(T_{n-1} - T_n) \tag{36}$$

A constant temperature boundary condition is enforced in Eq. 33, where T_{bc} represents the transient control plate temperature. The constant heat flux boundary condition is enforced in

Eq. 34, where $\dot{q}_{bc}$ represents the transient heat flux estimation. When running constant heat flux simulations, Eq. 33 is used to calculate the heater temperature considering the contact resistance. However, in constant temperature boundary condition simulations, Eq. 34 is not required to solve the energy balance because the temperature at the next step is already set by the boundary condition data. Also for constant temperature simulations, Eq. 34 is not used to calculate a performance metric since the heat flux was not directly measured. Instead, total melt time is used as the constant temperature performance metric.

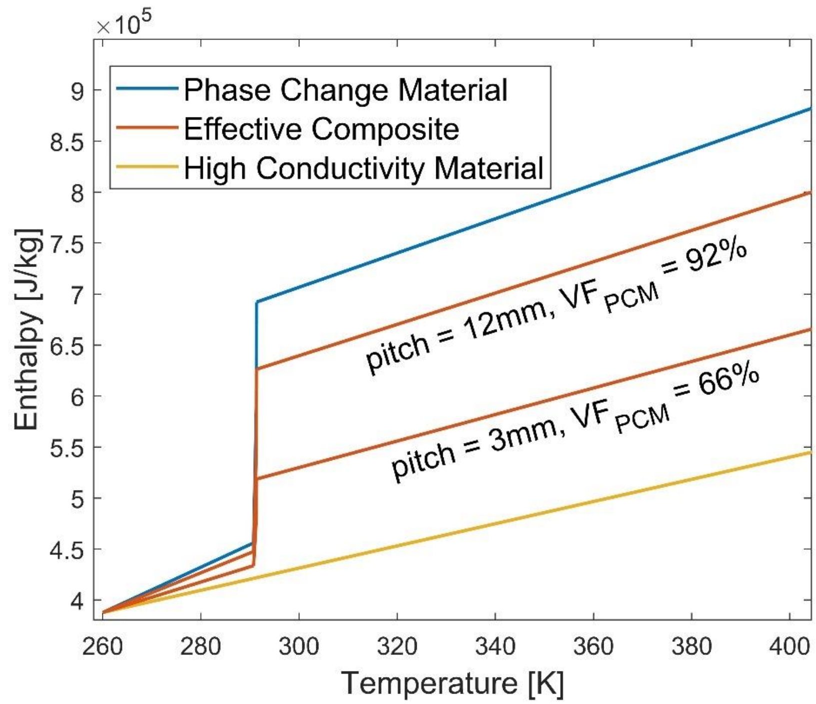

Figure 36: Effective enthalpy versus temperature relationship for the 3 mm and 12 mm fin pitch, bounded by the pure material profiles.

APPENDIX B: TRANSIENT BOUNDARY CONDITION ESTIMATION

A transient boundary condition was characterized for constant heat flux simulations by first estimating the resistive heater capacity. To do so, the heater was weighed, and then six 3-mm pitch tests were performed at varying powers with hexadecane filled to the standard fill height. The total estimated energy storage was calculated by summing the PCM latent capacity, the PCM and fin sensible storage, the HCM base sensible storage, and the heater sensible storage. The PCM sensible storage was estimated using the average temperature of the 8 thermocouples positioned in the PCM. The average temperature difference from the initial temperature was then converted into sensible heat storage with the PCM mass and liquid heat capacity. The sensible storage in the other materials was calculated using the same method. Four thermocouples were averaged along the fins to obtain the average temperature difference. The HCM base and the heater both used three equally spaced thermocouples to obtain the average temperature rise of the material. At c_{heater} = 450 J/kg·K, the error between the total estimated energy storage and the electrical power delivery is shown in Table 7.

Table 7: Heater Capacity Validation at the 3-mm fin pitch.

Test Power	40 W	60 W	80 W_1	80 W_2	120 W_1	120 W_2
Energy Storage Error [%]	-4.74	-1.59	2.05	1.20	0.71	-0.13

This allowed for the heater internal energy to be estimated with the thermocouple measurements and respective material heat capacities. The rate of heat storage in the resistive heater was used to calculate the transient heat delivery in Eq. 37.

$$\dot{q}_{delivered} = \dot{P}_e - m_h c_h \frac{dT_h}{dt} \tag{37}$$

$\dot{P}_e$ is the constant electrical power delivered via the DC power supply.

Two 12 mm pitch tests were performed at 120 W to determine if the device geometry impacted the heater temperature response. Fig. 37 shows a comparison of the 120-W tests at 3 mm and 12 mm. It shows that the steady state heat delivery to the TES is consistent across pitch. While there is a slower transient response in one of the 12-mm tests, it resulted in only a 3.58% difference in total heat delivery compared to the other tests throughout the transient period. After the transient period, differences in heat delivery were negligible. Since this testing condition was also the most extreme case, the difference was determined to be small enough to use the 3-mm transient power delivery profiles for all simulations.

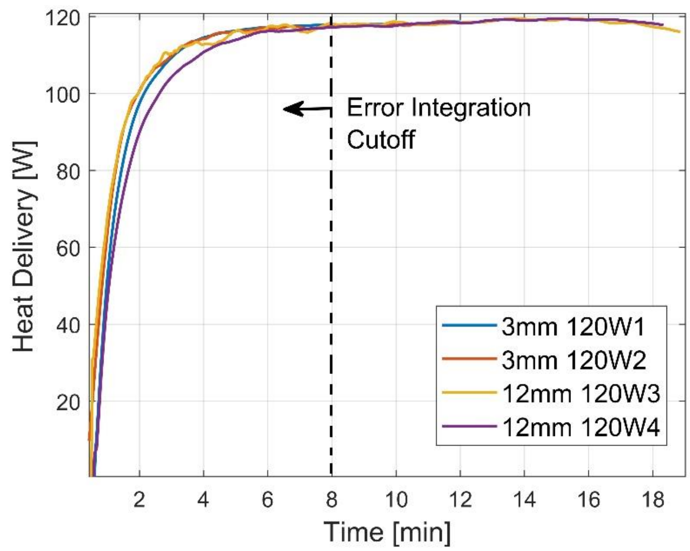

Figure 37: Estimated heat delivery profiles after applying the fitted heater capacity for two 12-mm and two 3-mm tests.

As in Fig. 13(b), heat delivery profiles show that the transient period lasted roughly 4 minutes for all power setpoints, followed by a steady state period where heat delivery to the test section remained with 3% of the power setpoint. The deviation in the estimated heat delivery between pitches was observed using an integrated difference in instantaneous heat delivery before the error integration cutoff. The maximum observed deviation in total heat delivery before the cutoff was 3.58% (between the 12mm 120W4 and the 3mm 120W3 tests).

APPENDIX C: CONTACT RESISTANCE ESTIMATION

Three potential contact resistances were estimated for this study: base to temperature-control plate ($R''_{c,1}$ in constant temperature tests), base to resistive heater ($R''_{c,2}$ in constant heat flux tests), and fin-base plate interface ($R''_{c,3}$ present in both tests). For constant temperature tests, three thermocouples were placed at the interface between the base and temperature-control plates (see Section 2.2.1). It was assumed that the thermocouple readings accurately represented the base temperature. This assumption effectively sets $R''_{c,1}$= 0 K·m^2/W, allowing Eq. 33 to simplify to $T_{bc} = T_{base,1}$ for constant temperature simulations.

Because $R''_{c,1}$was excluded from the EMA model, the fin-base contact resistance could be independently evaluated for constant temperature conditions. Ideally, the convection model would be used as it generally provides the most accurate estimate of base temperature. However, $R''_{c,3}$ could not be determined through post-processing, and iteratively running simulations for multiple resistance guesses was computationally prohibitive. To address this, $R''_{c,3}$ was estimated by aligning the total melt time of 1-D EMA simulations (at 3 mm fin pitch) with the experimental results reported in Table 8. While this approach is not ideal, the 3-mm pitch tests exhibited minimal natural convection and negligible two-dimensional effects, particularly at low power levels. These conditions suggest that even the simplified 1-D EMA model should reasonably predict discharge time. The resulting estimate for $R''_{c,3}$ was 5×10^{-6} K·m^2/W.

Table 8: Discharge times after fitting a fin contact resistance to the 3-mm fin pitch tests.

	40 W	**80 W**	**120 W**
EMA Model Melt Time [min]	3.99	5.28	10.99
Experimental Melt Time [min]	3.97	5.36	10.70

The base to heater contact resistance ($R_{c,2}^{``}$) was estimated by comparing the temperature plots between the experimental and convection model data at the 3-mm 120-W condition. The highest heat flux was chosen because it results in the highest temperature sensitivity to changes in thermal resistance. The contact resistance was estimated by aligning the convection model and experimental base temperature values at the time where PCM begins to melt, roughly coinciding with the highest curvature point of the temperature versus time profile. This instant in time was found for the two data sets and displayed in Fig. 38 as $t_{latent\text{-}transition}$. The resulting temperature difference at that point in time was used with the instantaneous heat input to calculate a required resistance that would force the convection model temperature to be equal to the experimental temperature. The base contact resistance was then calculated using Eq. 38, yielding a value for $R_{c,3}^{``}$ of 1.37 × 10^{-4} K·m^2/W.

$$R_{c,3}^{``} = A_{base}\left(\frac{T_{exp} - T_{conv}}{\dot{q_{bc}}} - \frac{R_{c,fin}^{``}}{A_{fin}}\right) \quad (38)$$

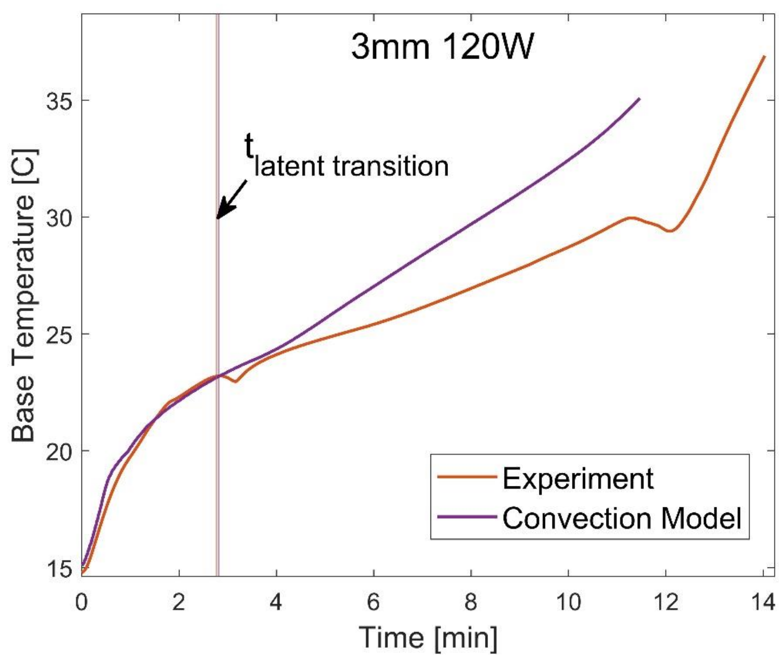

Figure 38: Base temperature profiles after applying the fitted contact resistances to the convection model.

This estimation method relies on assumptions that may introduce uncertainty, including perfect thermocouple accuracy, negligible $R''_{c,1}$, and the suitability of a 1-D model for evaluating the fin resistance. Future work should incorporate direct experimental validation of contact resistances to improve confidence in these estimates.

Attempts at experimentally measuring the contact resistance were performed for a single fin pressed into a slot. A resistive heater was adhered to the bottom side of an aluminum plate with the milled slot centered on the top side of the plate. Thermocouples were positioned at the plate-heater interface, at the plate's top surface, and at various positions along the fin length. The resistive heater heated the fins experiencing forced convection from a fan at a fixed volumetric flowrate. The thermocouple readings were recorded once the fin-heater system reached steady state for four different heater powers. An image of the testing setup is shown in Fig. 39.

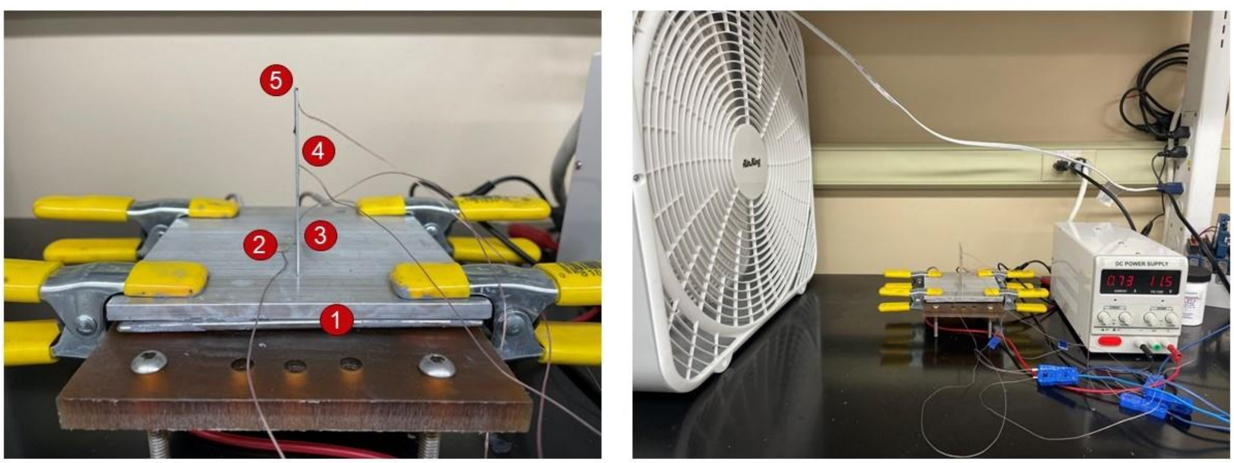

Figure 39: Experimental setup of the fin contact resistance measurement. (a) shows a closeup of the thermocouple positions and the heater-fin system. (b) shows the power supply and fan.

Two key parameters were needed to calculate the contact resistance: the heat transfer coefficient of air flowing over the fin, and the heat input into the fin. The heat transfer coefficient was determined by curve fitting the readings of thermocouples 3, 4, and 5 and solving for the dimensionless parameter m [1/m], as shown in Fig. 40. Once the fin parameter was determined, a heat rate into the fin was calculated using the temperature at the upper base surface (thermocouple 2) in Eq. 39. Finally, the fin contact resistance was calculated using Eq. 40.

$$\dot{q}_i = \left(T_{base,i} - T_{amb}\right) k_{fin} \, A_c \, m \, \tanh\left(m L_{fin}\right) \tag{39}$$

$$R''_{c,i} = \frac{T_{base,i} - T_{fin1,i}}{\dot{q}_i} \left(W_{fin} \, th_{fin}\right) \tag{40}$$

Values for contact resistance are plotted in Fig. 41 with uncertainty values propagating from a ±0.25 °C uncertainty on thermocouple temperature. This was included to reflect observed temperature fluctuations at steady state conditions. The average contact resistance from the four heat rates was calculated to be 6.32 × 10−5 K·m^2/W. This value is roughly one order of magnitude greater than the contact resistance of 5 × 10−6 K·m^2/W prescribed to our models, but there are reasonable explanations for why this difference may exist. First, the fin combs apply considerable pressure to the fin-base interface during PCM testing, but the single fin was freestanding during the steady state test. Pressure is understood to reduce contact resistance, although it is unclear what the exact pressure the fins experienced and how much that would reduce contact resistance. Second, during the contact resistance experiment, ambient air-filled gaps between the fin and base with a thermal conductivity of 0.025 W/m·K. During PCM testing, liquid PCM filled the gaps between the fin and base with a thermal conductivity of 0.145 W/m·K. This order of magnitude difference may also contribute to the measured contact resistance being higher than what was fitted to the PCM melting data. In all, an agreement roughly within one order of magnitude and two clear reasons to expect a higher resistance in the single-fin experiment provided confidence that the fitted contact resistance is a reasonable value.

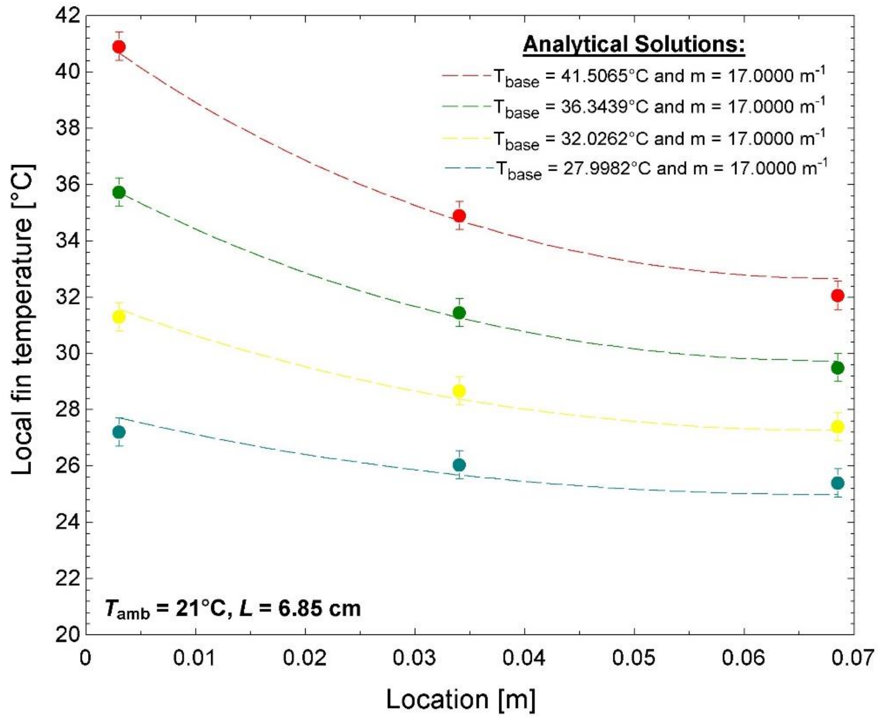

Figure 40: Curve fitting to characterize fin performance with experimentally measured temperature distributions.

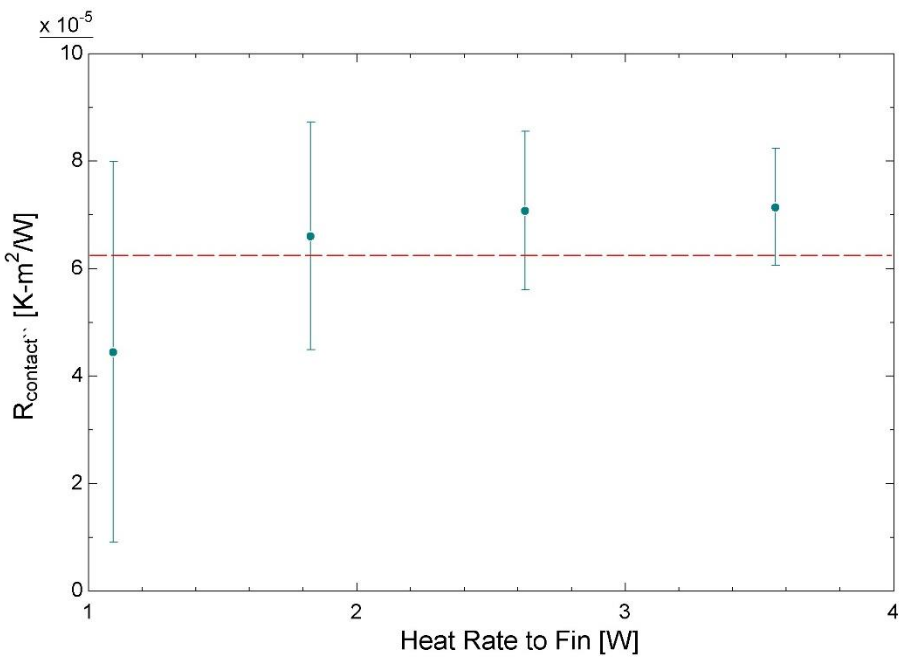

Figure 41: Estimated contact resistance from the single-fin experiment at four heat input rates.

APPENDIX D: DESCRIPTION OF UPPER BOUND ON 2-D MELTING

An idealized 2-D melting case was considered as an upper bound for comparing experimental melt dynamics. In this scenario, the fin temperature was assumed to be uniform and equal to the base temperature (η = 1). Under these assumptions, the melt front would moves away from all HCM at a uniform rate, as illustrated in Fig. 42(a), where Δx_l representing the melt front distance from the HCM. The region where the vertical and horizontal melt front overlap was assumed to not be affected by the combined heat input. This assumption keeps the melt front rectangular and simplifies the calculation of the 1-D deviation factor. The liquid fraction can then be expressed in terms of Δx_l and the channel dimensions in Eq. 41:

$$f_{liquid} = \frac{\Delta x_l W_{ch} + 2\Delta x_l (L_{ch} - \Delta x_l)}{W_{ch} L_{ch}} = \frac{\delta_l W_{ch} + 2\Delta x_l L_{ch} - 2\Delta x_l^2}{W_{ch} L_{ch}} \tag{41}$$

Where the fin thickness is subtracted from the fin pitch to get the channel width, W_{ch}, while the channel length is set to the solid PCM fill height.

The PCM aspect ratio was then calculated and normalized against the channel aspect ratio in Eq. 42:

$$AR_n = \frac{L_{ch} - \Delta x_l}{W_{ch} - 2\Delta x_l} \frac{W_{ch}}{L_{ch}} \tag{42}$$

Finally, the normalized 2-D isothermal fin aspect ratio can be converted to a deviation from the 1-D melting in the same way as with the experimental data (Eq. 25 from Section 4.1). This equation can be plotted at the channel widths and height of the test section in Fig. 42(b). The result has a slight dependence on fin pitch, but the differences are relatively small. The 12-mm pitch profile was used as the upper bound for the 2-D melting behavior shown in Fig. 15.

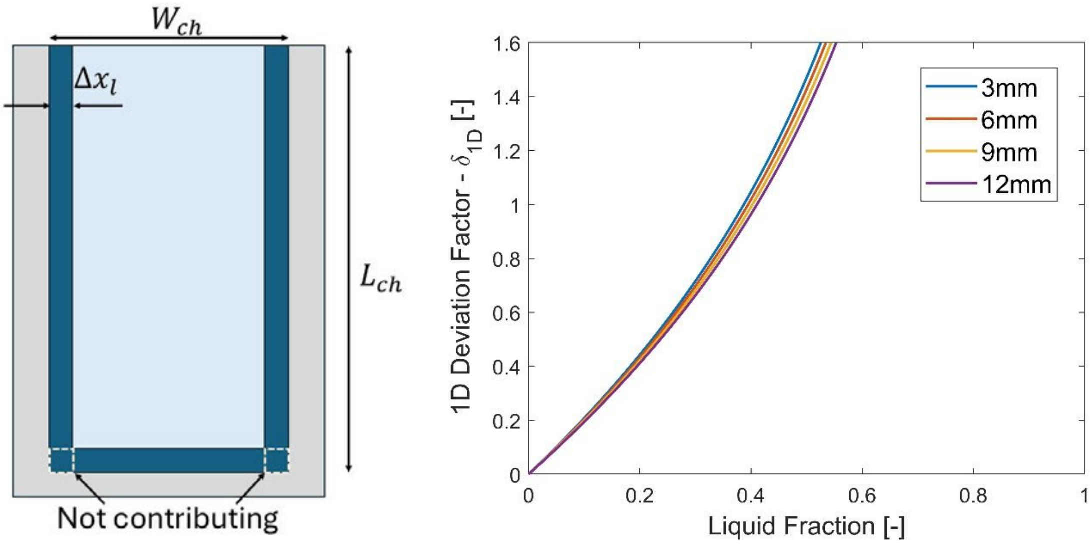

(a) Idealized melting diagram

(b) Idealized 2-D melting dynamics at the relevant fin pitches

Figure 42: Illustration of the upper bound in 2-D melt dynamics.

APPENDIX E: DESCRIPTION OF 3-D CIRCULATION PATTERNS

Section 4.4 of the main manuscript mentions the effects of 3-D natural convection and pressure driven flow as primary contributors to model error at the 3-mm and 6-mm fin pitch. Supplemental material has been provided to illustrate the two phenomena. Videos of the phase front are presented at the 3-mm 25℃, 3-mm 120-W, and 12-mm 35 ℃ testing conditions. They showcase pressure driven flow across various pitches and boundary conditions. In the videos, a crest of liquid PCM rises above the fill line at the center of the test section. This occurs when the first pathway for liquid PCM to flow through opens up and releases the built-up pressure below the solid PCM. When this happens, warm PCM from outer channels is sucked into the center and up through the open passage. Once the pressure is released and PCM can flow freely in all channels, the crest begins to equally distribute itself along the test section width.

The relevance of pressure driven flow on device performance can be approximated by a comparison of time scales between pressure driven flow and melt time. The total time where pressure driven flow affects the liquid PCM distribution was consistently between 2 and 4 minutes long. PIV videos indicate that the period this noticeably increases fluid velocities is shorter than the total time when liquid PCM is elevated. Consequently, tests with melt times far greater than the time scale for pressure driven flow will have unaffected performance metrics, whereas tests with melting times at a similar time scale as pressure driven flow may be significantly affected. While the degree of impact would gradually diminish, tests that are certainly within a similar time scale include the 3-mm tests at constant temperature boundary conditions and the 120 W tests at 3 mm and 6 mm.

PIV videos are presented at 3-mm 120-W at 9 minutes, 6-mm 120-W at 13 minutes, and 12-mm 35℃ at 13 minutes. The 3-mm 120-W test is representative of the maximum particle movement observed at the 3-mm fin pitch and can be compared with other videos to demonstrate the insignificance of convection-based fluid motion for the 3-mm pitch. The video of particle motion at 6-mm pitch highlights 3-D cellular circulation patterns, as visualized particles in the same x-y position moving in opposite directions.

APPENDIX F: LOCAL EVALUATION OF THE 2-D CONVECTION MODEL

Model validation in the main manuscript focuses on global performance metrics, such as the base temperature evolution and the total melt time. While these parameters are important for system-level analysis, they provide limited insight into the internal heat transfer mechanisms. To ensure that the model's accuracy is not the result of compensating errors, this section compares local temperature histories and phase-front progression for the 12-mm fin pitch case (45°C).

Fig. 43 shows local temperatures of the fins and within the PCM at four vertical locations (13 mm, 27 mm, 41 mm and 55 mm above the base). The 2-D convective model accurately predicts fin temperatures across all locations and times, and captures the influence of natural convection evidenced by the matching temperature plateaus at lower elevations. Additionally, the model precisely identifies the final melt time, indicated by the sharp rise in PCM temperature once the latent heat capacity is exhausted.

Despite strong qualitative agreement, noticeable differences in local PCM temperatures (recorded 3 mm and 6 mm from the fin centerline) provide insight into the system's complex fluid dynamics. These differences primarily stem from three factors: temperature glide in the PCM, differences in the phase front location, and the precise location of PCM convective cells.

First, there is a distinct difference in the thermal behavior of the solid-phase PCM. While the numerical model predicts nearly isothermal phase change (remaining at the melt temperature until local phase change is complete), the experiment shows a gradual temperature rise. A clear example of this temperature glide is seen at T9. Here, the model predicts a sharp temperature increase at approximately 11 minutes, while the experimental data shows a steady rise between 5 and 11 minutes. As corroborated by the phase-front information in Fig. 16 of the main manuscript, the PCM is still solid in the experiment during this interval. This observed glide may result from the simplified thermophysical properties in the model or local variations in the melt fraction in this region.

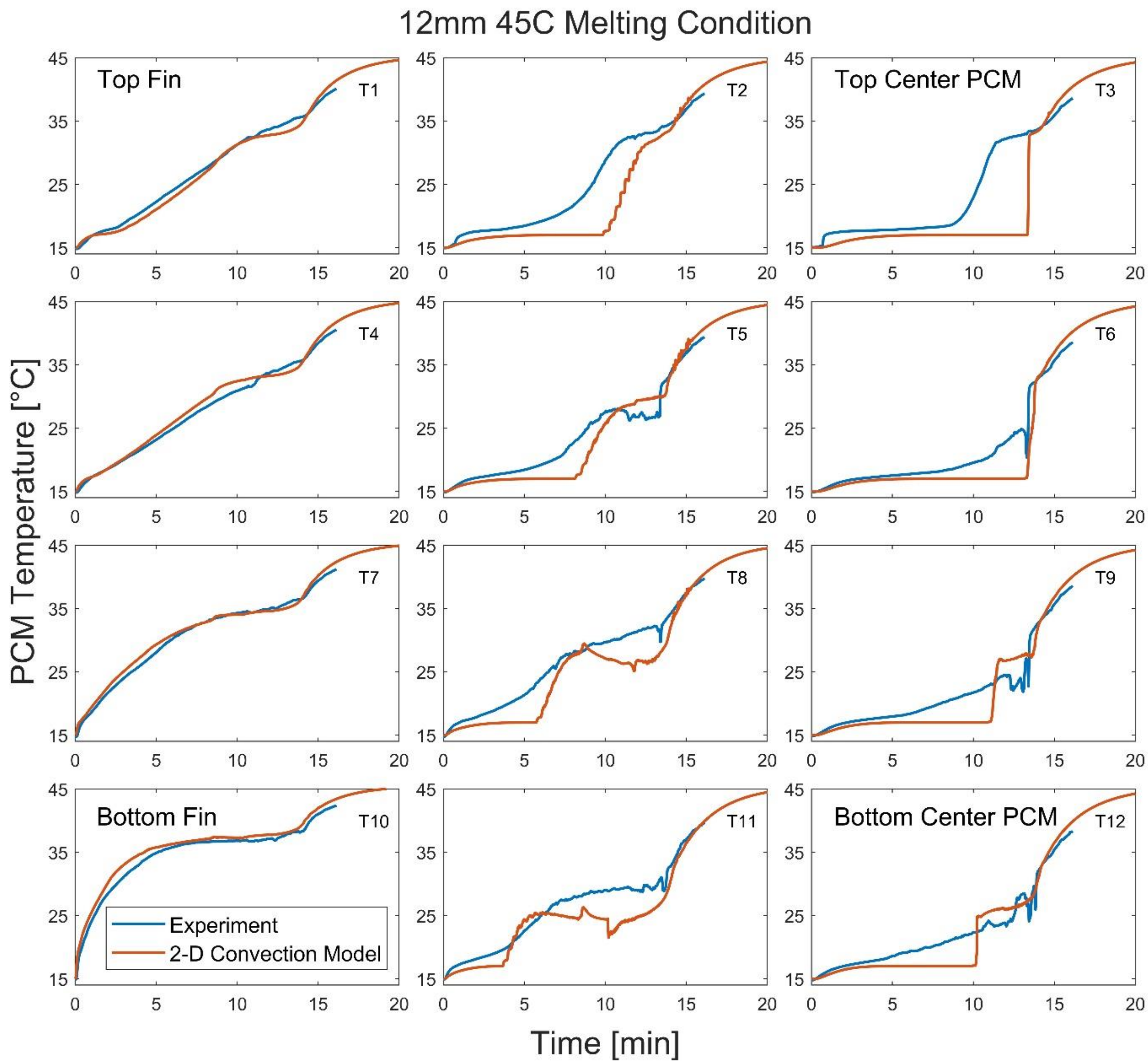

Figure 43: Local comparison of PCM composite temperatures between the experiment and the 2-D convection model. THe bottom row corresponds to thermocouples 13 mm from the base-PCM interface.

The initial temperature jump shows when local phase change is complete. While generally well-predicted, timing offsets occur near the top of the test section (at T2 and T3). These offsets are primarily attributed to volumetric expansion of the PCM upon melting, a factor not considered in the numerical simulations. In the experiment, the expanded warm liquid flows into the region above the solid PCM, melting the top region of the test section faster than the model predicts. This effect results in an earlier temperature rise observed in these locations.

Finally, the temperature plateaus during the melting process are governed by natural convection. These plateau temperatures are highly sensitive to the spatial locations of the measurements relative to the convective cells. For example, a thermocouple positioned within a downward convective plume will record a significantly lower temperature than one placed just a few millimeters away in a stagnant or upward-moving region. We attribute local differences (notably T8 and T11) to the precise positioning of the vortex structure and minor misalignments in experimental thermocouple placement. However, the excellent agreement in the fin temperature plateaus suggests that the 2-D convective model accurately captures the overall convective heat transfer coefficients along these heated surfaces.

Visual analysis of the phase front provides further context for the local temperature variations. Fig. 44 displays the experimental melt front at 3, 6, 9.5, and 12 minutes, with the 2-D numerical prediction overlaid in green. These images visually confirm volumetric expansion of the PCM during melting. While the model and experiment share the same total liquid height, the solid PCM height is lower in the experiment due to density changes. This displacement drives liquid PCM to the top of the test section, causing accelerated heating at T2 and T3, as discussed previously. This comparison demonstrates that local spatial discrepancies are largely a function of simplified volume assumptions rather than fundamental errors in heat transfer physics.

At the 12-minute mark, a local discrepancy in liquid fraction appears between the numerical model and the experimental image. While the global liquid fraction (87.5%) is closer to the model’s prediction (93.9%), the local channel in Fig. 44 appears to lag. This is due to PCM detachment, which occurred in uninstrumented channels but was absent in this specific test section.

This difference is critical for understanding the possibility of compensating errors. If the unmodeled effects of PCM detachment compensated for inherent errors in natural convection modeling, one would expect significant model errors in channels where PCM detachment does not occur (i.e. the instrumented channels). This was not demonstrated in the fin temperature profiles in Fig. 43, thereby supporting the assumption that the compensating mechanisms of natural convection and PCM detachment have a limited impact and that the global figures of merit reasonably reflect the local melting characteristics. For future studies, local predictive accuracy could be further refined by explicitly modeling PCM expansion during the phase-change process.

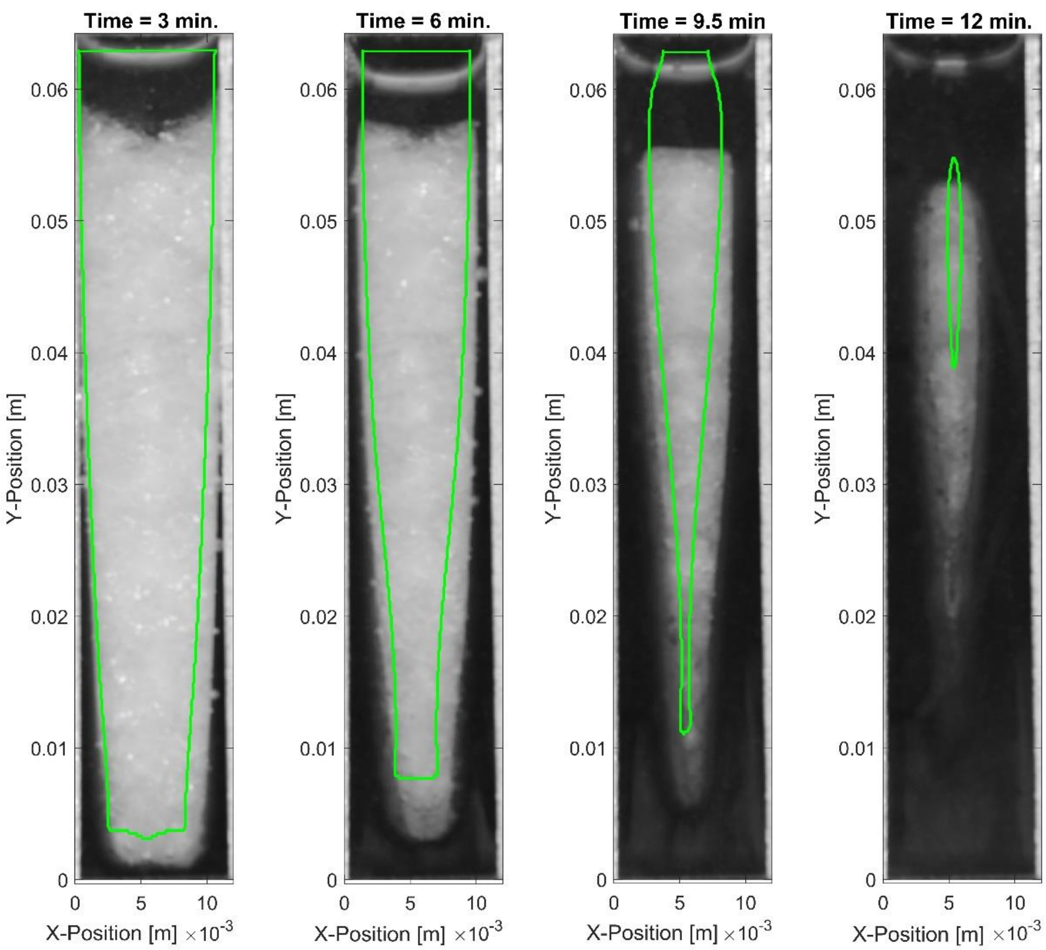

Figure 44: Local phase front at four instances in the time compared between the experiment and the 2-D convection model (shown in green).

APPENDIX G: PARALLEL FIN TEST PROCEDURE

Appendix G describes the test procedure for the constant temperature and constant heat flux tests, starting with pouring the PCM into the test section. It assumes that the appropriate fins have already been inserted into the test section with proper instrumentation and that the fin combs have been fastened to the acrylic walls.

Preparation and Freezing – All Tests

1. Determine the volume of PCM required based on the fin pitch using the Test_Section_Dimensions.m code.
2. Pour the required PCM volume into a marked measuring container.
3. Start LabVIEW and open Heater_control_v4. Go to the display window and set all the PID gains to the values listed in red. Run the LabVIEW code.
4. Turn on the chiller and set the temperature setpoint to 12 ºC. Turn on the pump switch and heater on the electrical control box.
5. In LabVIEW, turn on the pump and set the hardcode voltage control to 2V.
6. For constant heat flux tests, ensure that there is no thermal paste on the temperature control plate. Remove any layers that are still on. For constant temperature tests, ensure that there is a uniformly thick coating of thermal paste on the temperature control plate large enough to cover the full device footprint. Place the desired number of wire thermocouples on the thermal paste. These wires should come from terminals 13 and up in the NI-DAQ card.
7. Bring the test section to the flow loop table and connect all PCM thermocouples to their leads by matching the number labels on each wire.
8. Test the thermocouples by pressing the "Collect Data" button in the LabVIEW control panel. Collect data for at least 10 seconds and then unselect the "Collect Data" button.

Open the newly made excel document and check that all the thermocouples are reading correctly.

9. Place the test section on the temperature control plate. Have it centered with the device edges between the lines demarking the no-drill zone. If running a constant temperature test, insert the rod thermocouples into the base slots.
10. Clamp the device down with the 3 yellow clamps. There should be two clamps at the front of the test section, and one in the rear.
11. Repeat step 8 to test for base thermocouple malfunctions with pressure applied to the base.
12. Turn the pump voltage control to 3.5 volts.
13. Begin filling the test section with PCM. Pour PCM in between the two fin combs and move the container from left to right to ensure each channel is filling equally. The PCM should be filled in roughly four layers, with a small fifth layer to even any differences in fill height. Wait until the previous layer has fully frozen before pouring the next layer in. Place the insulation box around the TS after each pour.
14. Monitor the freezing process visually and with the thermocouple charts. Once the thermocouples have reached a temperature below 14 ºC, change the chiller setpoint to 14 ºC.
15. Let the thermocouples equilibrate to within 1 ºC of each other. Move on to the respective melting test procedures once the thermocouples equilibrate.

<u>Melting Procedure – Constant Temperature Tests</u>

1. Position the phase front camera in front of the test section. Turn on and focus the camera on the front acrylic wall with the 2x lens. Ensure that the right edge of the insulation box is against the 80/20 support bar on the far right of the flow loop table.
2. Position the phase-front flood lights on either side of the camera and turn them on. The lighting values should be preset, so adjust the position of the lights to remove glare coming from the insulation.
3. If running PIV, Position the PIV table so that the four legs are inside the marked rings on the floor. There are two sets of rings; constant heat flux tests should be using the right-most set.
    a. Use a personal laptop to connect an HDMI to the PIV camera.
    b. Turn on the PIV DC power supply. Adjust knobs to supply a power of 80 W each.
    c. Open PIV_BaslerTriggering_Script.py on the personal laptop and prepare the code with the correct test name. The file name should follow this format: “V”*mm* “W”*C*“X” *PIV*“Y”*_min*“Z”. Where

        “V” = pitch value

        “W” = temperature setpoint

        “X” = Test iteration. 1 if this is the first test at that condition

        “Y” = PIV measurement count

        “Z” = minute timestamp when measurement occurs.
    d. Make sure the PIV table is set so that it is out of the line of sight of the phase front camera.

e. Plan out the times when PIV will be taken. Use the 1-D EMA model to estimate the melt time, and then select times to have at least seven PIV measurements. Try to avoid taking PIV measurements before the liquid fraction has reached 35%.

4. Clear any existing photos from the phase front camera. Go to the menu tab and find the timelapse feature. Prepare the settings to take up to 200 photos every 30 seconds.
5. Stop the LabVIEW code briefly to allow the data writing system to reset. This ensures that LabVIEW knows what file to write to and prevents it from throwing an error early in the test. Turn the LabVIEW code back on after a couple of seconds.
6. Set the pump voltage control to 4 Volts.
7. Turn the bypass valve to divert chilled water flow to the bypass loop.
8. In the LabVIEW window, turn on the heater control and the PID "Control Water Temperature" buttons. Set both temperature setpoints to the desired setpoint temperature.
9. Once the water temperature at the outlet of the resistive heater has reached the setpoint temperature, select the "Control Plate Temperature" button and the "Collect Data" button. This officially starts the test. Quickly press "OK" on the phase front camera to start the imaging sequence.
10. Observe the temperature charts and the test section to ensure that the boundary condition is being properly enforced. There will be a transient settling time required to get the base plate temperature to the setpoint.
11. If Taking PIV data:
    a. In between phase front images, move the PIV camera rig in front of the test section. Use your hand to stabilize the table for about 8 seconds. Turn on the LED lights.

b. Run PIV_BaslerTriggering_Script.py.

c. Return the PIV camera rig to be out of the phase front camera line of sight.

d. Increase the PIV measurement count after the data had been recorded.

12. Repeat step 11 at the designated PIV measurement times.
13. Periodically observe the test section for signs of significant leakage. If the PCM is visibly draining from the test section. Stop the test and move to the clean-up procedure.
14. Stop taking image data and thermocouple data once the PCM has fully melted. Turn off the heater and its control buttons. Reduce the pump voltage control to 2 volts.
15. Rename the thermocouple data excel doc to match the form:
“Pitch”*mm* “temperature-setpoint”*C*“Test-count”
16. Use a personal laptop to transfer the images. Only keep the .jpg images from the transfer.

Melting Procedure – Constant Heat Flux Tests

1. Set up the DC power supply with wire leads to the resistive heater.
2. While freezing, tune the power supply to the correct voltage and amperage for the power level you require with the resistive heater attached. If the resistive heater gets hot, cool it down next to a fan for the remainder of the freezing process.
3. Apply a layer of thermal paste to the resistive heater surface. Attach the desired number of wired thermocouples to the base by pressing them into the thermal paste.
4. With the PCM temperatures at 14 ºC, remove the insulation box and yellow clamps and attach the TS to the resistive heater. Align the heater to the PCM region of the TS.
5. Secure the heater by placing four bolts through the TS and the acrylic support block. Lightly screw the bolts up to the support block face.

6. Insert any rod thermocouples between the TS and the heater.
7. Use an Allen key and a wrench to fasten the bolts to the acrylic support block. This sandwiches the heater to apply pressure at the TS-heater interface. Fastening the bolts is easiest if the TS is placed on top of the temperature control plate.
8. Ensure that the base thermocouples are not malfunctioning on the LabVIEW charts.
9. Move the bottom half of the constant heat flux insulation box on to the flow loop table. It should be placed so that its left edge is against the 80/20 support bar on the left side of the table. An acrylic sheet is kept on the floor of the insulation box to use as a hard surface for the heater bolts to stand on.
10. Move the heater-TS assembly on to the bottom half of the insulation box and then set the top half of the insulation in place. The acrylic window should fit into a slot in the insulation. Turn off the chiller and pump.
11. Position the phase front camera in front of the test section. Turn on and focus the camera on the front acrylic wall with the 2x lens.
12. Position the phase-front flood lights on either side of the camera and turn them on. The lighting values should be preset, so adjust the position of the lights to remove glare coming from the insulation.
13. If running PIV, Position the PIV table so that the four legs are inside the marked rings on the floor. There are two sets of rings; constant temperature tests should be using the left-most set.
    a. Use a personal laptop to connect an HDMI to the PIV camera.
    b. Turn on the PIV DC power supply. Adjust knobs to supply a power of 80 W each.

c. Open PIV_BaslerTriggering_Script.py on the personal laptop and prepare the code with the correct test name. The file name should follow this format: “A”*mm* “B”*W*“C” *PIV*“D”*_min*“E”. Where

“A” = pitch value

“B” = power level

“C” = test iteration. Set to 1 if this is the first test at that condition

“D” = PIV measurement count

“E” = minute timestamp when measurement occurs.

d. Make sure the PIV table is set so that it is out of the line of sight of the phase front camera.

e. Plan out the times when PIV will be taken. Use the 1-D EMA model to estimate the melt time, and then select times to have at least seven PIV measurements. Try to avoid taking PIV measurements before the liquid fraction has reached 35%.

14. Clear any existing photos from the phase front camera. Go to the menu tab and find the timelapse feature. Prepare the settings to take up to 200 photos every 30 seconds.
15. Stop the LabVIEW code briefly to allow the data writing system to reset. This ensures that LabVIEW knows what file to write to and prevents it from throwing an error early in the test. Turn the LabVIEW code back on after a couple of seconds.
16. Turn on the DC power supply. Press the “Collect Data” button on the LabVIEW control window and begin the imaging sequence on the phase front camera. This officially starts the test.
17. If Taking PIV data:

a. In between phase front images, move the PIV camera rig in front of the test section. Use your hand to stabilize the table for about 8 seconds. Turn on the LED lights.

b. Run PIV_BaslerTriggering_Script.py.

c. Return the PIV camera rig to be out of the phase front camera line of sight.

d. Increase the PIV measurement count after the data had been recorded.

18. Periodically observe the test section for signs of significant leakage. If the PCM is visibly draining from the test section. Stop the test and move to the clean-up procedure.
19. Stop taking image data and thermocouple data once the PCM has fully melted. Turn off the heater and its control buttons.
20. Rename the thermocouple data excel doc to match the form:

    "Pitch"*mm* "power"*W*"Test-count"
21. Use a personal laptop to transfer the images. Only keep the .jpg images from the transfer.

Clean-up Procedure

1. Remove the insulation box to access the TS. Wipe away any PCM on the surface on the test section.
2. Prepare a 60-ml syringe with a nyloc tube and set the stopper to be at 30 ml.
3. Extract PCM from the TS and into a measured container with the nyloc tube. Keep the stopper above the 35 ml mark to make sure that hexadecane does not wet the stopper.
4. Detach the thermocouple connections from each other to allow the TS to be moved.
5. Once at least half of the PCM is removed from the TS, detach the TS from the heating element and pour the remaining PCM into the measured container using a funnel.

6. Measure the volume of PCM lost by comparing the container fill level to the starting fill level. Then pour the PCM from the container into the sealed PCM bottle.

APPENDIX H: PIV DATA ANALYSIS AND RESULTS

The PIV analysis was performed using the open-source software PIVLab. The integrated MATLAB toolbox was used to preprocess, analyze, and postprocess the image data collected from the PIV camera. Appendix H outlines the procedure used for PIV image analysis.

PIV is an optical flow measurement technique that extracts velocity information from the displacement of tracer particles in a fluid. In this work, the experimental setup consisted of flow seeded with neutrally buoyant particles and illuminated by two high power LEDs. A Basler acA2440-35uc camera was positioned in front of the 2-D melt front to acquire 60 image frames at a specified time delay. To discern a velocity, the analyzed field is split into interrogation windows. In each window two consecutive frames are cross correlated by their particle intensity patterns, identifying a mean particle displacement in that window. Dividing that displacement by the time delay yields the mean velocity in an interrogation window, which is then performed across the full field. Appropriately choosing a constant time delay is important for ensuring that particles remain well within their interrogation windows between frames, but also that there is enough movement for the cross-correlation to detect a noticeable displacement.

Achieving a consistent interframe delay was a non-trivial aspect of the PIV setup. Initial attempts at using the Basler Pylon software for image acquisition showed that the interframe time could not be controlled while images were being saved. Fig. 45 shows the bulk velocity average – the mean of all interrogation windows in quasi-steady flow analyzed by PIVLab – for a set of frames taken with the Pylon software.

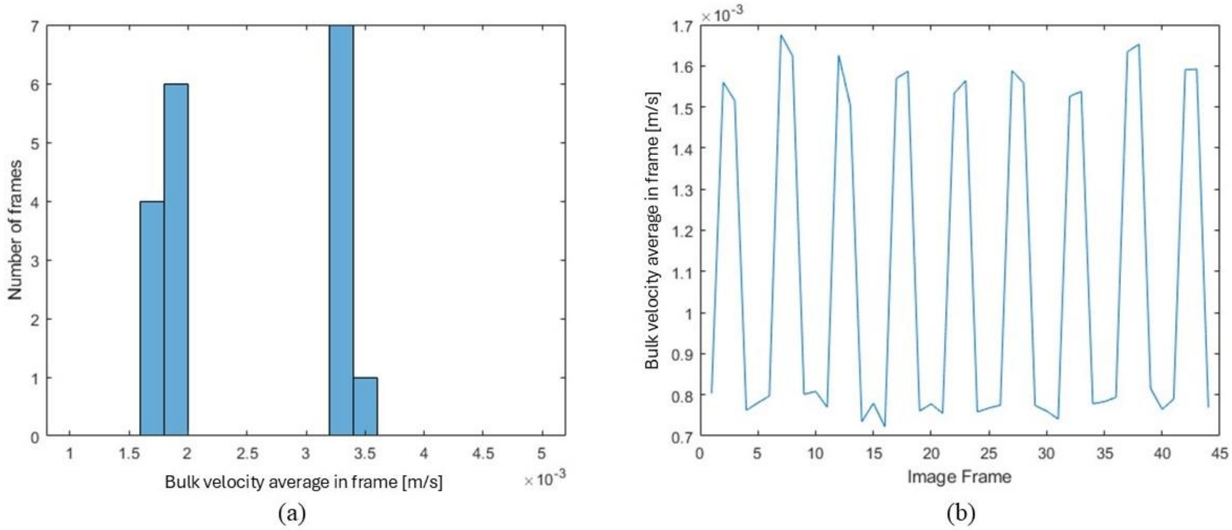

Figure 45: Imaging rate, proxied by average particle motion, for a set of image frames taken with the Basler Pylon software. **(a)** shows a histogram of the number of frames grouped by mean velocity. **(b)** shows a frame-by-frame history of the calculated mean velocity

The bulk velocity of a particle is coupled directly to the interframe rate because PIVLab assumes a constant time delay, meaning that if the actual delay is twice as long than expected, the calculated velocity will be twice as fast. From Fig. 45 it is obvious that the software was struggling to maintain the interframe rate set by the user. The bimodal distribution in Fig. 45(a) of velocity where one grouping is double the other suggested that frames were being skipped. Furthermore, the regularly repeating pattern in Fig. 45(b) indicated that this skipping occurred when the camera could not transmit the image file to the computer before the next image was meant to be taken. To fix this, a python script was developed to simultaneously trigger the camera, save it locally, and then transfer it to the computer all in parallel steps. Fig. 46 plots the framerate (1/s) by frame pair for a 60-image set taken at an exposure of 20000 μs and a framerate of 26 frames per second using the parallel-processed python script.

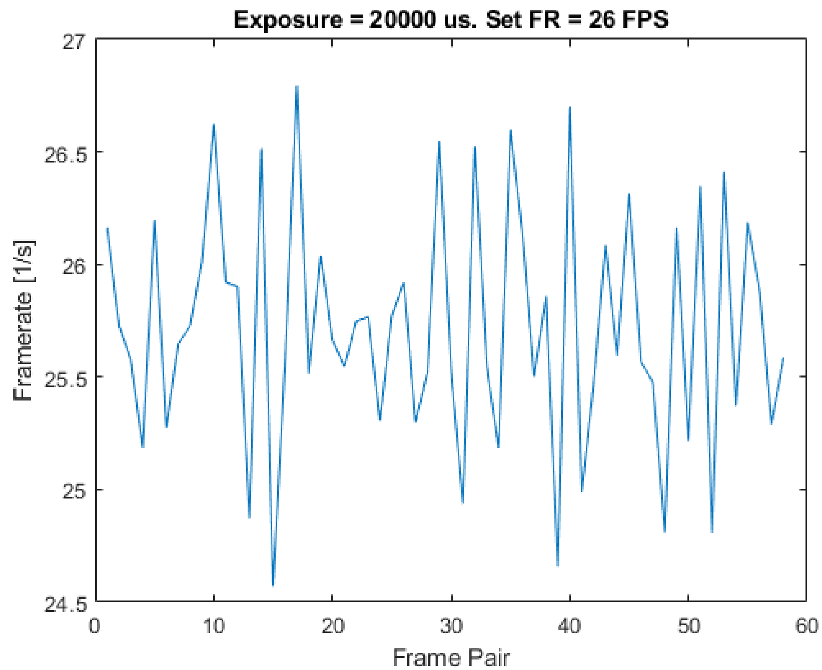

Figure 46: Frame rate between images for a group of 60 images taken with the parallel-processed python script.

Fig. 46 demonstrates a substantial improvement in image triggering and saving. Previously the framerates would oscillate by a factor of 2, but here they remain within 2.5 hz of each other. For a particle travelling at 3 mm/s, a difference of 2.5 hz in interframe delay taken at 30 frames per second would correspond to an uncertainty of ±4.2%. This was taken into consideration with other uncertainty factors with the error bars in Fig. 18.

Once the uncertainty in image triggering was deemed within usable limits, melting tests were performed with PIV data collection. After a test, the PIV image data was uploaded into the PIVLab software for analysis. The following text outlines a procedure for the PIV analysis.

<u>PIVLab Data Processing Steps:</u>

1. Import images using the “Time Resolved” option. Choose the folder you would like to take data from, then select all images in that folder except for the last. Press the “Add” then the “Import” buttons.

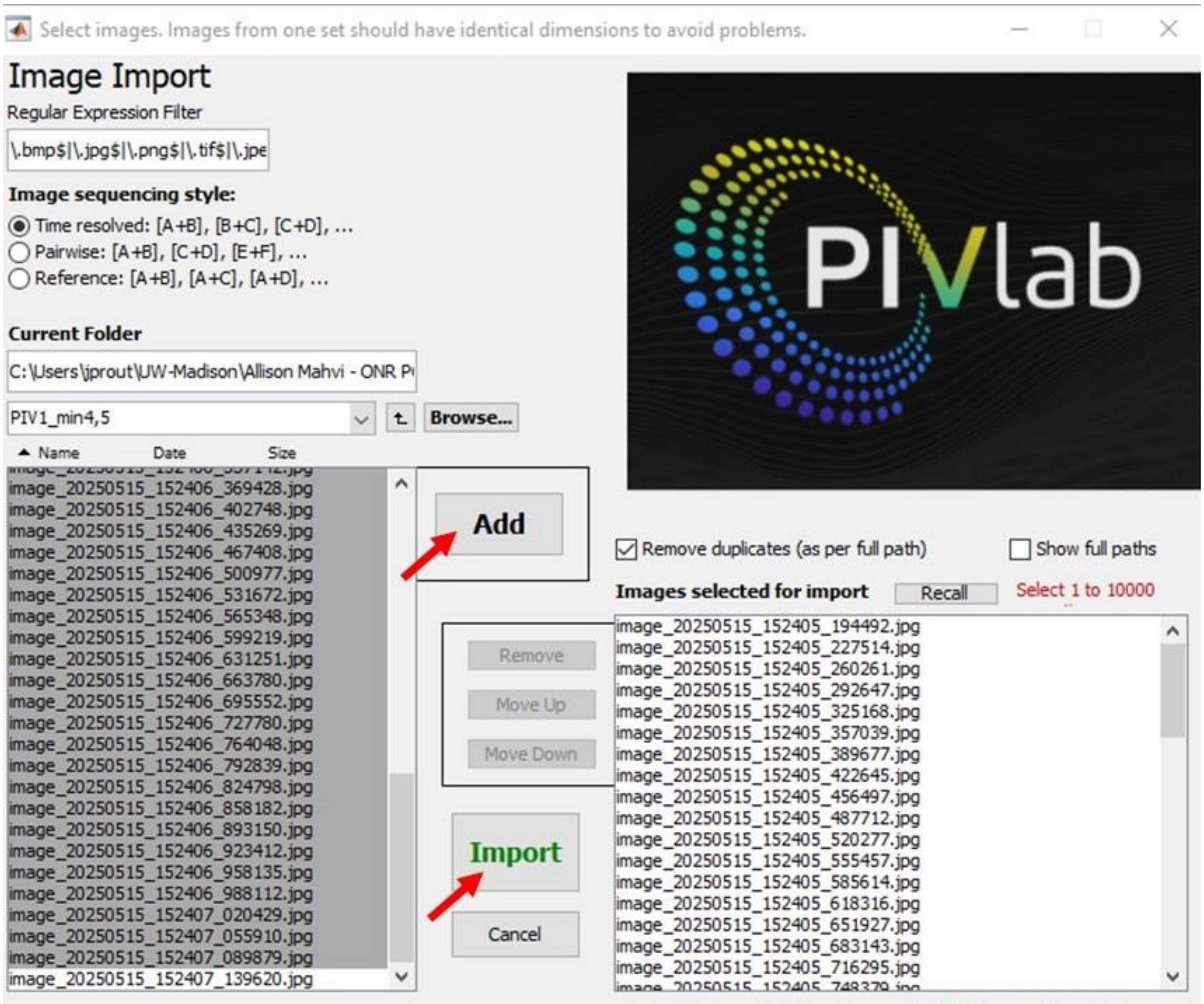

Figure 47: Image Selection and Import

2. Select region of interest. This should be one channel with clear visibility of the tracer particles. The region of interest should extend from the base to the top of the liquid melt height.

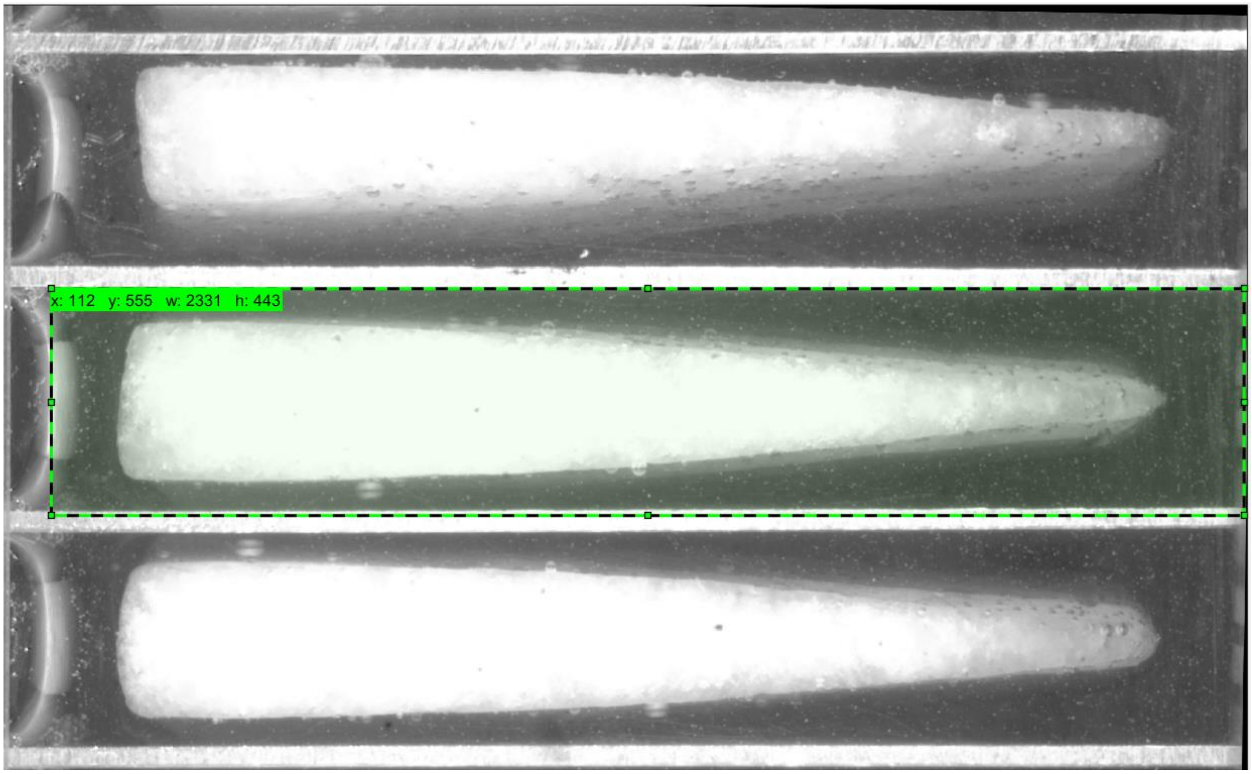

Figure 48: Selecting a region of interest using the example of the 12 mm 120 W test.

3. Image Masking: Draw a mask around the solid PCM body. Use the “Free hand” feature to create a curved shape. Waypoints can be added by left-clicking the mask to edit the shape after the initial drawing is finished. Once the mask matches the solid PCM shape, click “Copy mask to all frames”. You can save a mask and reupload it using the “Save all masks button”. This generally was not done if the analysis for a set of frames was finished in one sitting.

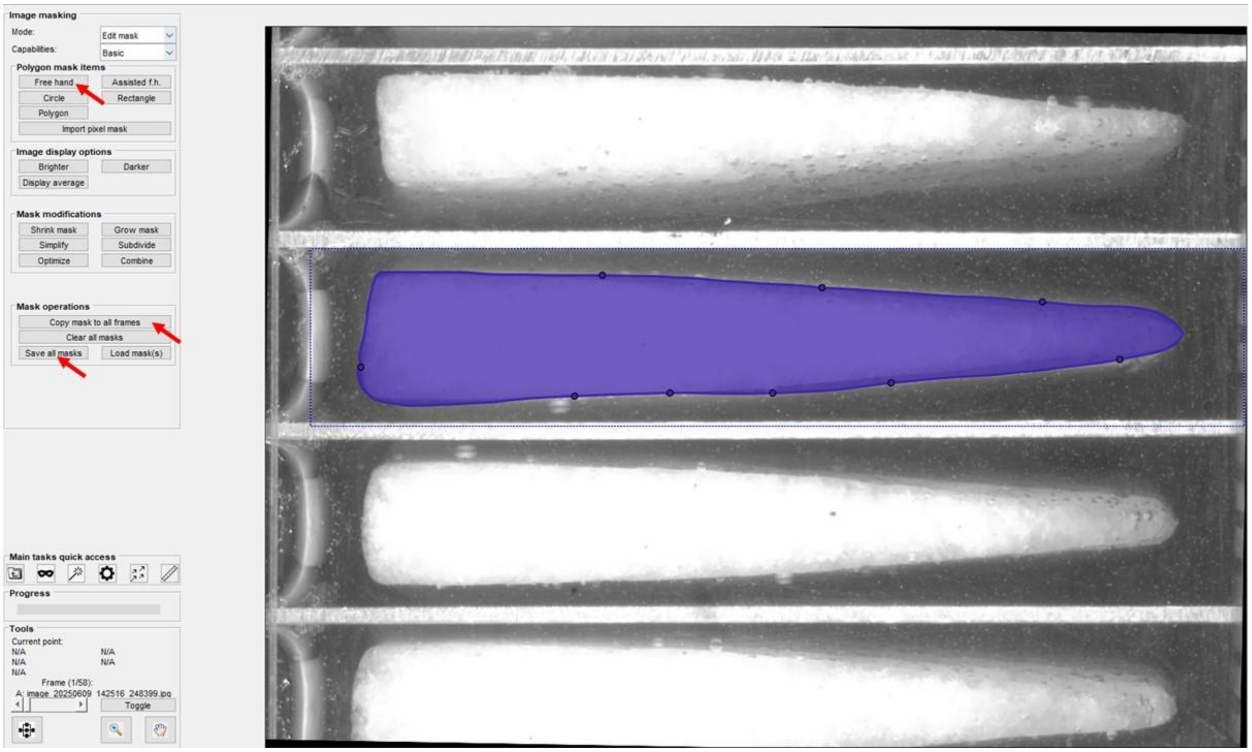

Figure 49: Image masking to occlude the solid PCM from PIV analysis.

4. Image Preprocessing: Go to image preprocessing by selecting the wand icon. Enable highpass Kernal size [px] at 15. Make sure that CLAHE is enabled at a window size of 64 pixels and that Auto contrast stretch is enabled. Then press the "Apply and preview current frame"

5. PIV Settings: Go to the PIV settings by selecting the gear icon. If analyzing a 12-mm test, set Pass 1 interrogation area of 128 pixels with a step size of 64 pixels. Enable Pass 2 and Pass 3, and set the Pass 2 interrogation window to 64 pixels and the Pass 3 interrogation window to 32 pixels. Use the Gauss 2x3-point pixel estimator with a correlation robustness set to "High". If analyzing a pitch below 12 mm, only use Pass 1 and Pass 2, using interrogation areas of 64 and 32 pixels. Press the "Analyze current frame" to get a preview of the analysis.

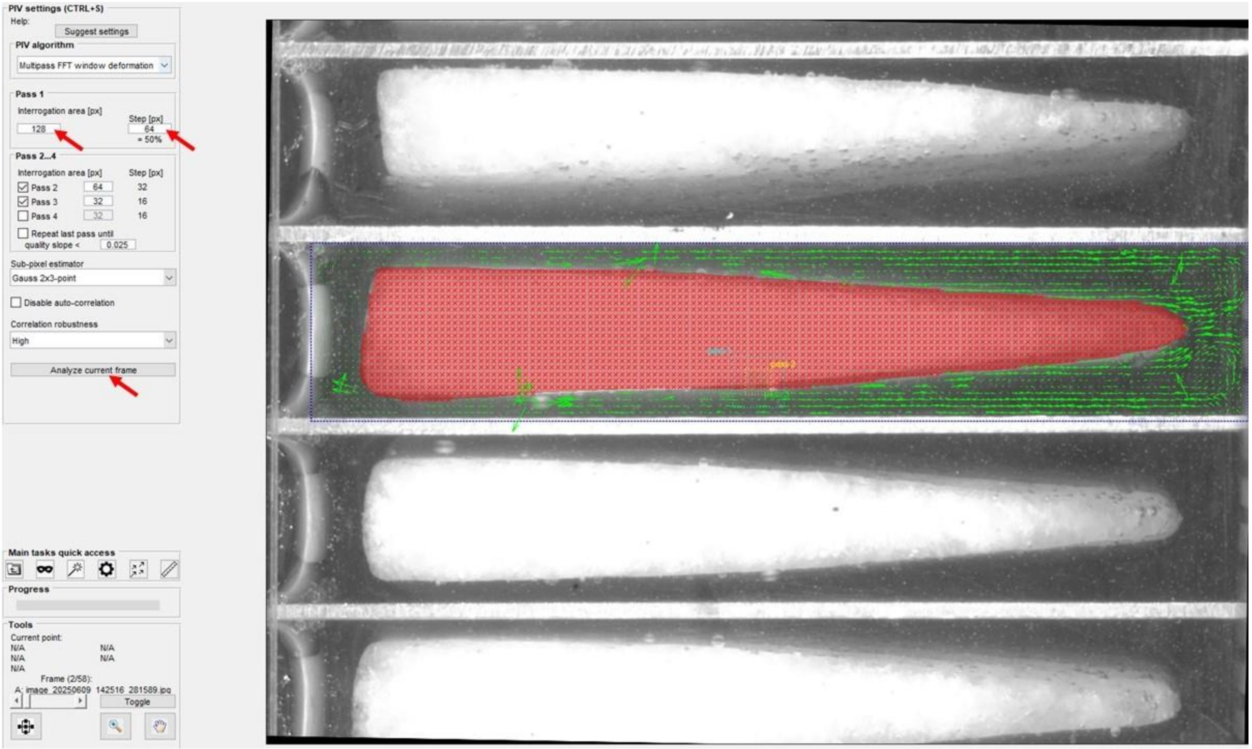

Figure 50: Select PIV analysis settings and preview the analysis on the current frame.

6. Analyze all frames by selecting the vector icon and pressing the “Analyze all frames” button. This can take longer than a minute to run, so only do this step once you know your PIV settings are correct.
7. Calibrate images: Calibrate the velocity vectors using an external image by selecting the dropdown menu and loading a calibration image. There should be a calibration image for every experiment. Draw a line from the 1 cm to the 5 cm line on the ruler. Set the special distance in mm to 50. Set the time step in milliseconds to 33. Press the “Apply calibration” button. Then change the Setup Offsets to x increasing towards the left, and y increasing towards the top. Press the “Apply calibration” button again.

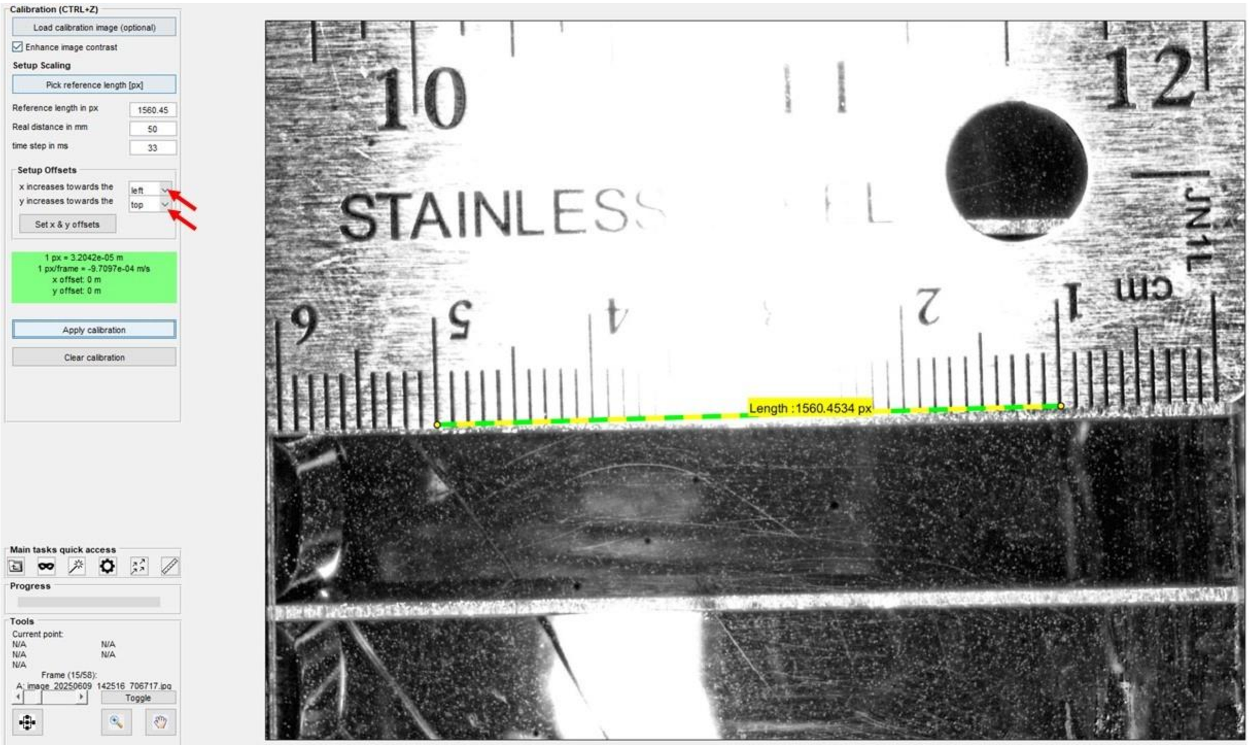

Figure 51: Calibrate the velocity vectors using an image taken for the specified test.

8. Vector Validation: Select velocity limits to remove outlier vectors. These are commonly caused by air bubbles rising up from the solid PCM. Press the select velocity limits and then draw a box around the main area of data. Set the standard deviation filter threshold to 8 and the local median filter threshold to 5. Unselect the "Interpolate missing data" option. Some fine tuning might be needed of the velocity limits and median filter threshold to achieve a valid particle density above 95% without clear outliers. Once that is the case, apply the limits to all frames.
9. Save the data: Go to file, export, MAT file. Then press the "Export all frames" and save the .mat file to the folder corresponding to the test name in the PIV folder. Data visualization is done using the MATLAB script PIV_Plotter.m.

PIV Analysis Results:

Local PCM velocity estimations are shown for the tests above 3-mm fin pitch. Liquid fractions were selected to range from 45% to 100%. The 12-mm constant temperature tests were visualized in channels that had solid PCM suspended by thermocouples. The suspended thermocouples did not influence the measurement results because they were farther into the test section that the illuminated particles. The following figures will be kept to Fig. 52 and marked by letters for brevity. Note the difference in color scales for the PCM velocity across plots.

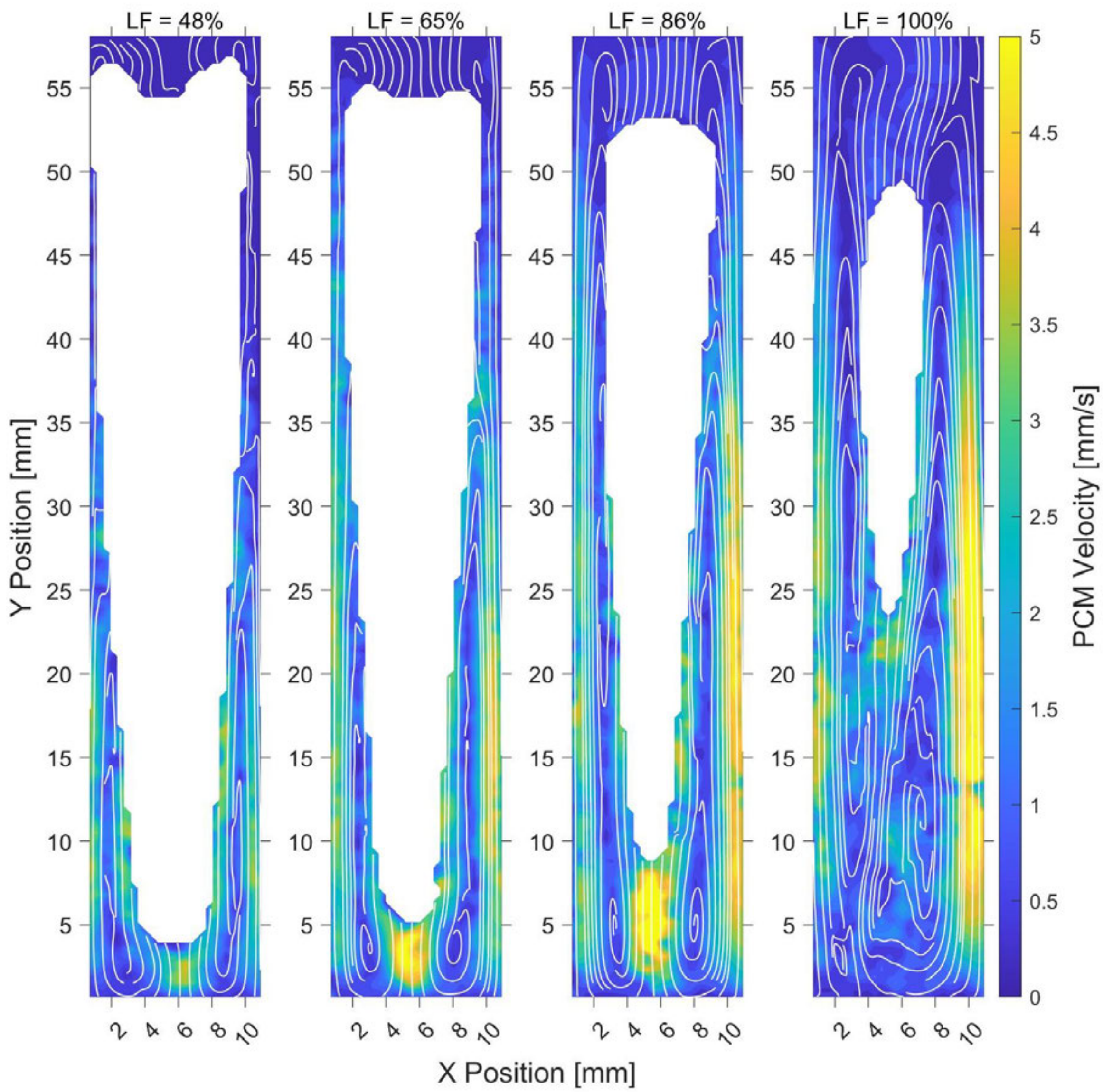

(a) 12mm 55C

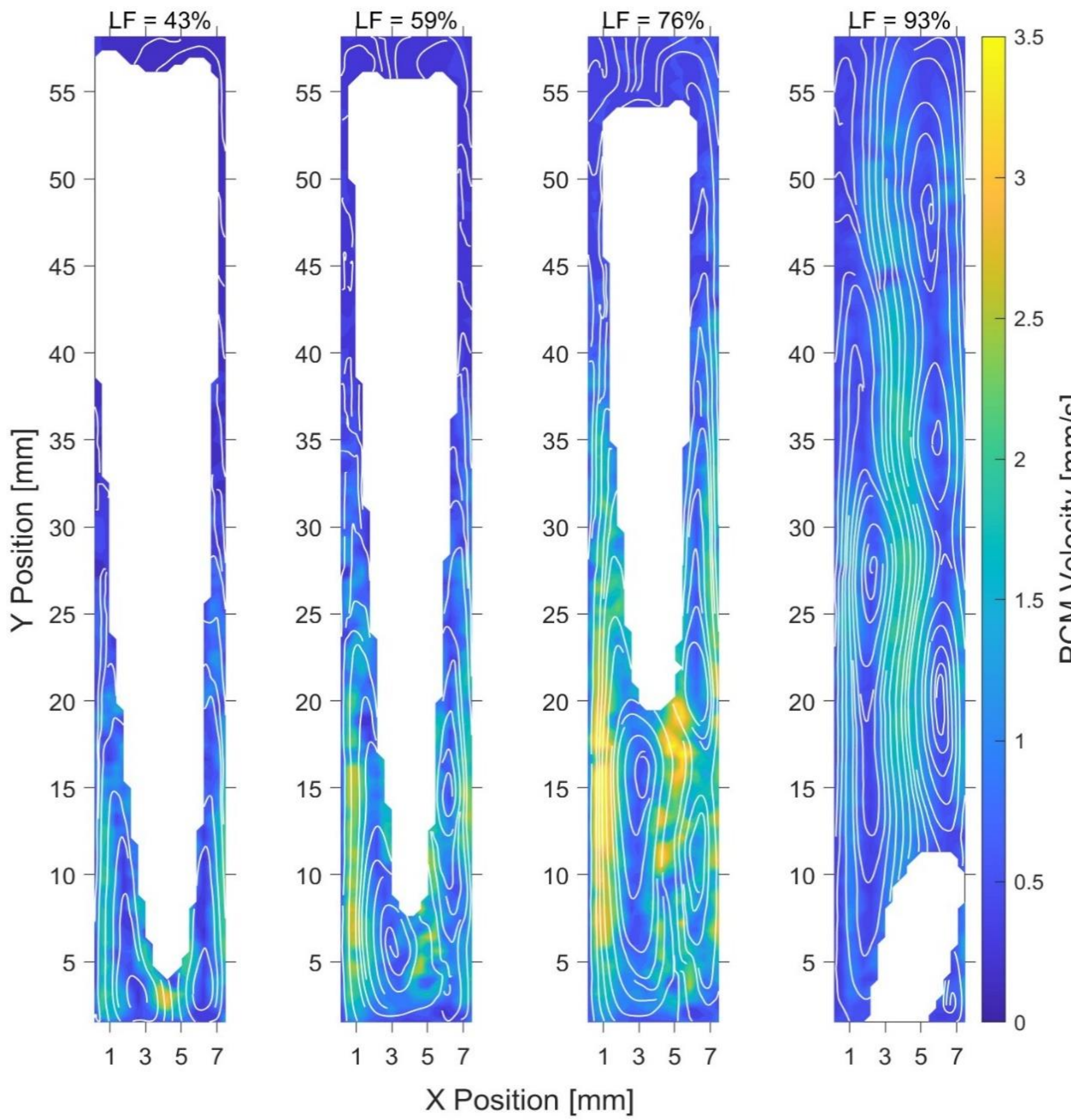

LF = 43%
LF = 59%
LF = 76%
LF = 93%
Y Position [mm]
X Position [mm]
PCM Velocity [mm/s]

(b) 12mm 45C

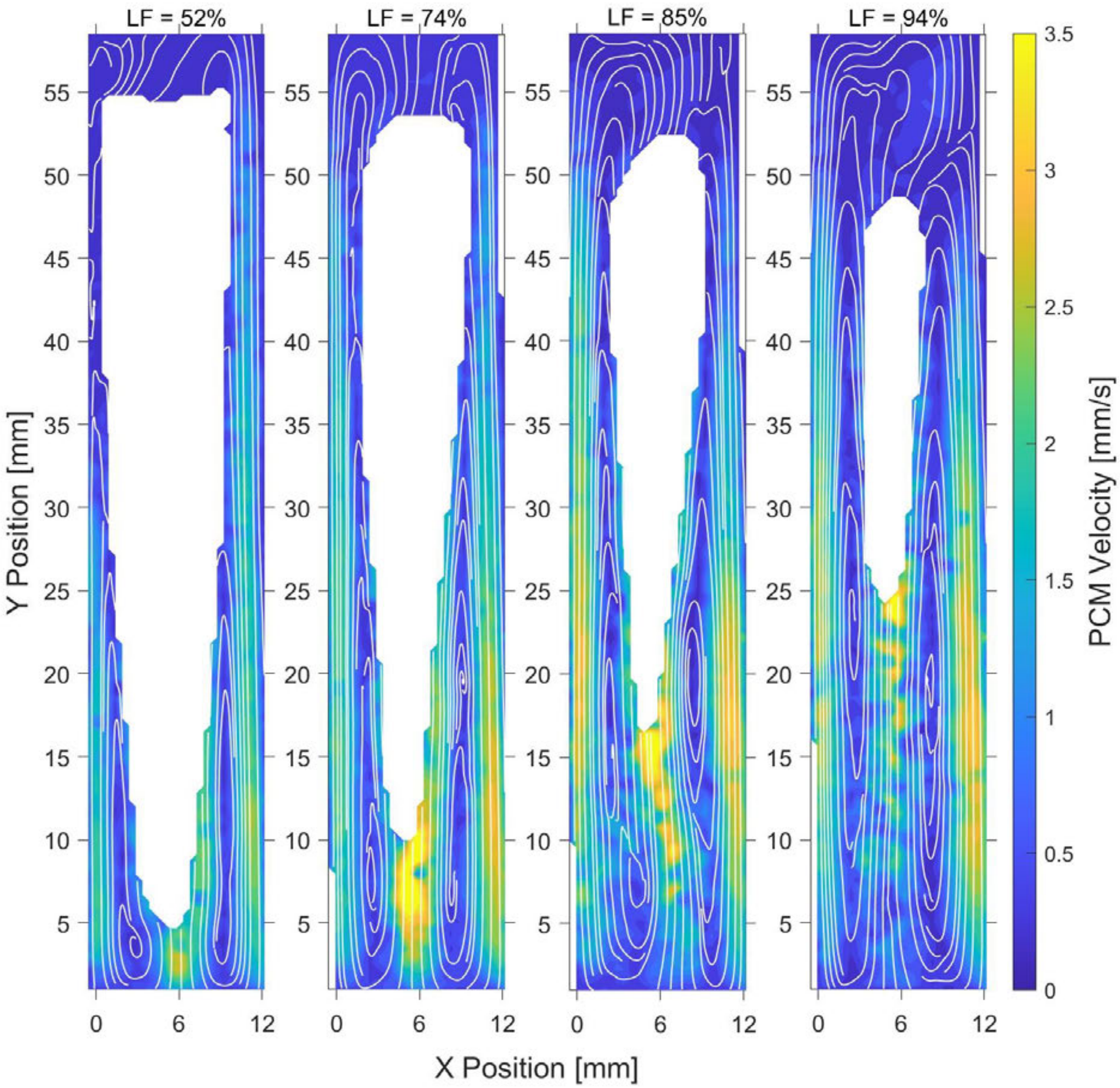

LF = 52%
LF = 74%
LF = 85%
LF = 94%
Y Position [mm]
X Position [mm]
PCM Velocity [mm/s]
0
6
12
5
10
15
20
25
30
35
40
45
50
55
0
0.5
1
1.5
2
2.5
3
3.5

(c) 12mm 35C

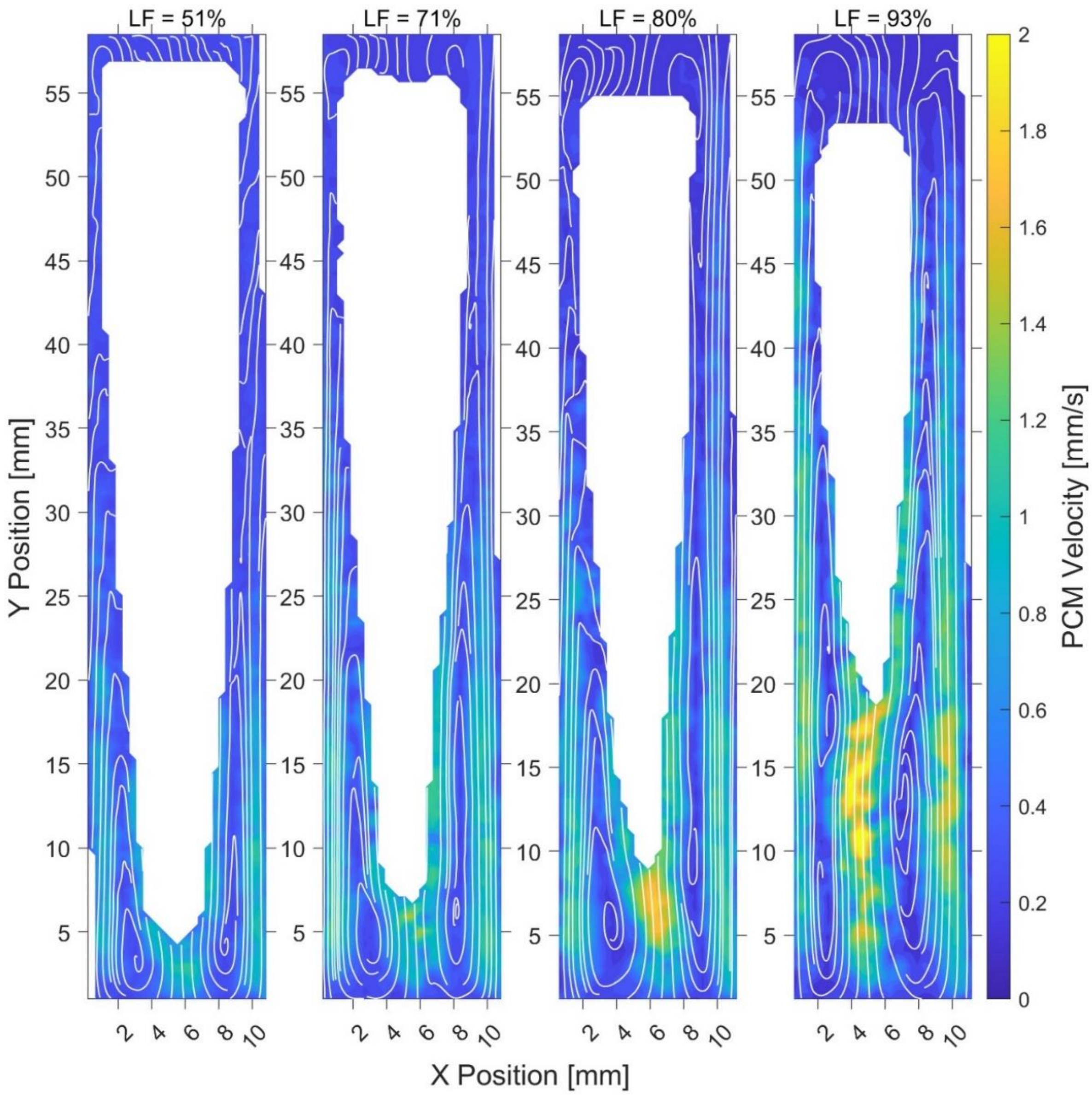
LF = 51%
LF = 71%
LF = 80%
LF = 93%
Y Position [mm]
X Position [mm]
PCM Velocity [mm/s]

(d) 12mm 25C

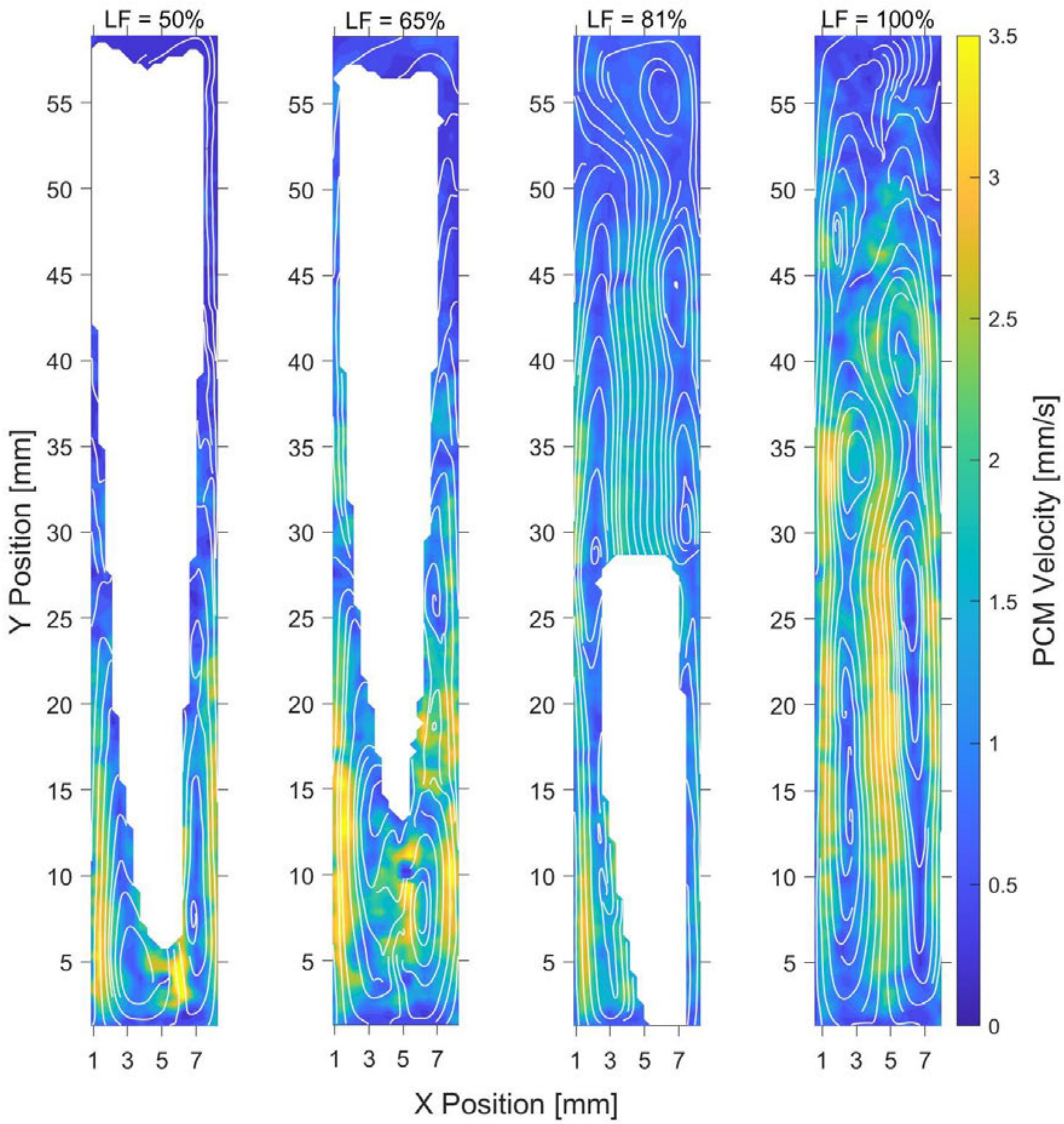
LF = 50%
LF = 65%
LF = 81%
LF = 100%
Y Position [mm]
X Position [mm]
PCM Velocity [mm/s]
55
50
45
40
35
30
25
20
15
10
5
1 3 5 7
3.5
3
2.5
2
1.5
1
0.5
0

(e) 9mm 55C

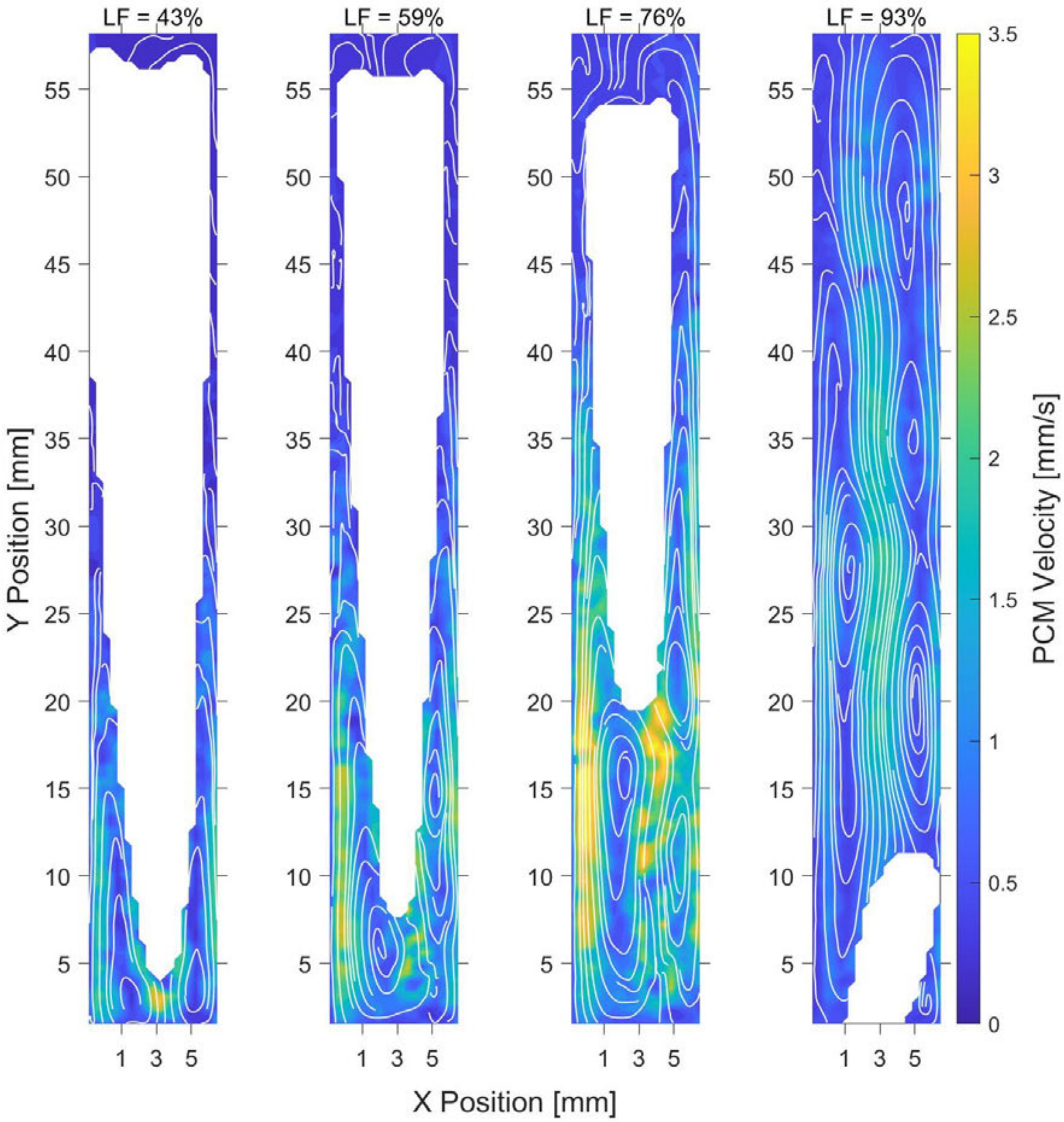
LF = 43%
LF = 59%
LF = 76%
LF = 93%
Y Position [mm]
X Position [mm]
PCM Velocity [mm/s]
55
50
45
40
35
30
25
20
15
10
5
1 3 5
3.5
3
2.5
2
1.5
1
0.5
0

(f) 9mm 45C

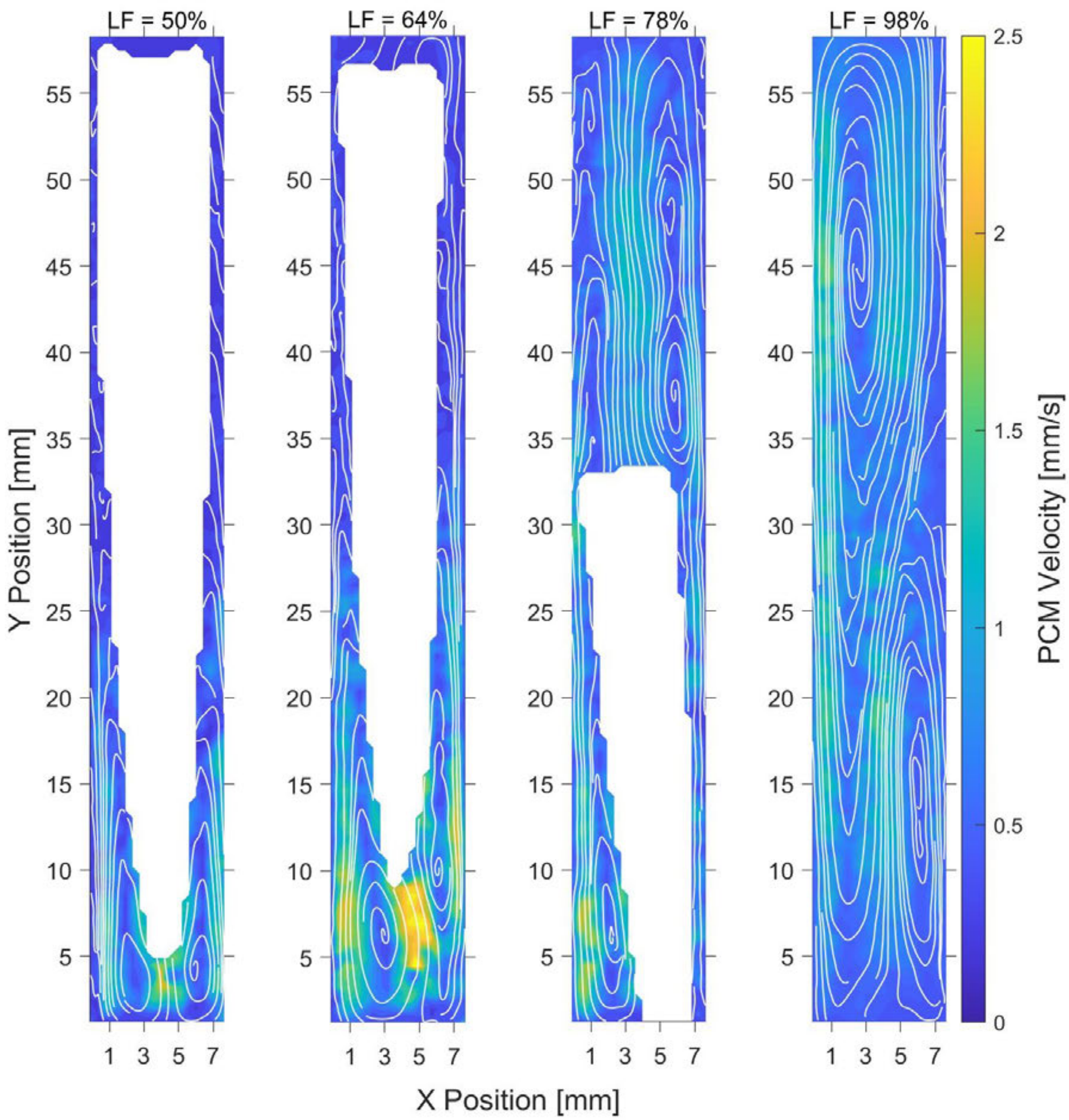

LF = 50%
LF = 64%
LF = 78%
LF = 98%
Y Position [mm]
X Position [mm]
PCM Velocity [mm/s]

(g) 9mm 35C

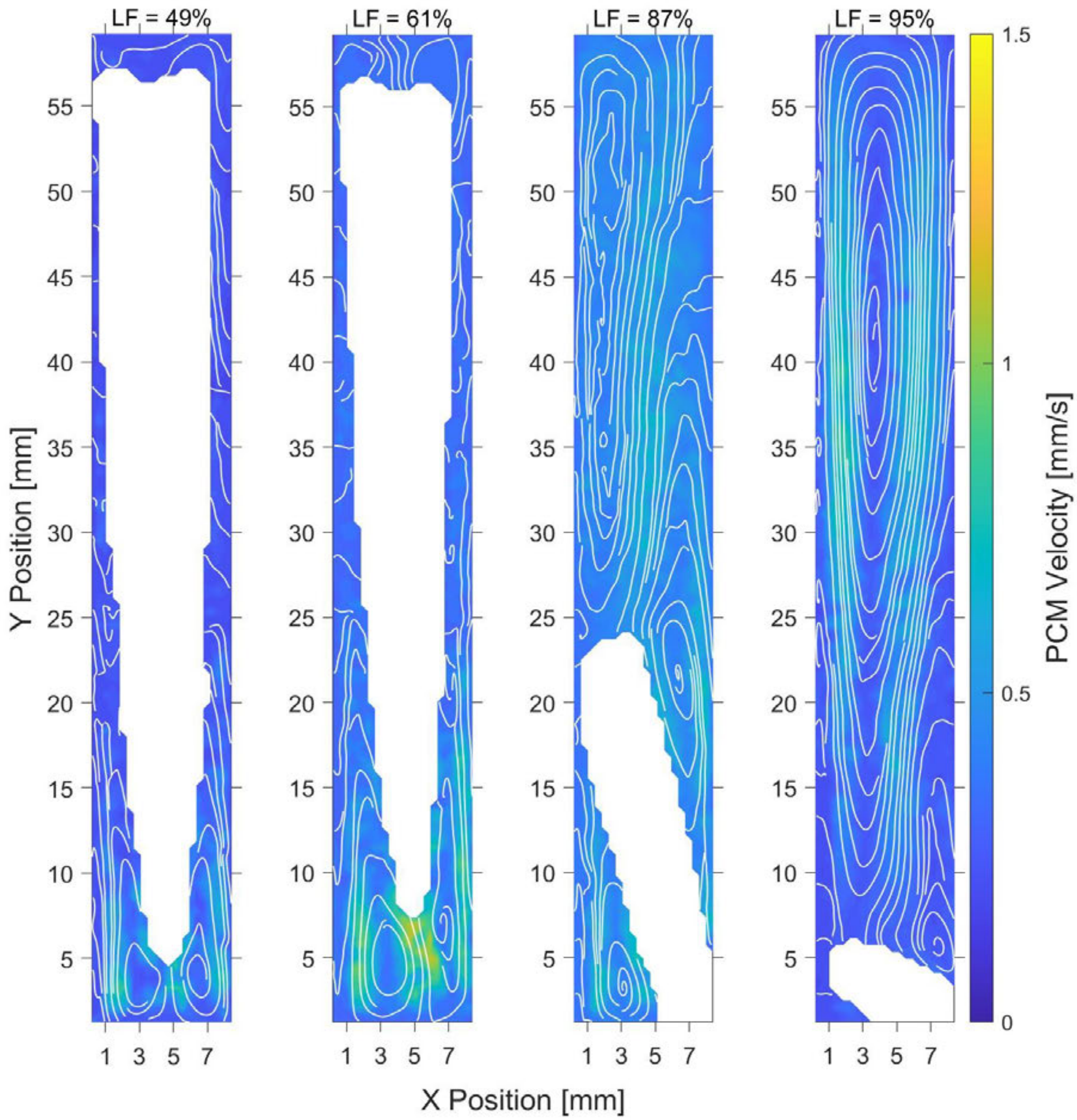

LF = 49%
LF = 61%
LF = 87%
LF = 95%
Y Position [mm]
X Position [mm]
PCM Velocity [mm/s]

(h) 9mm 25C

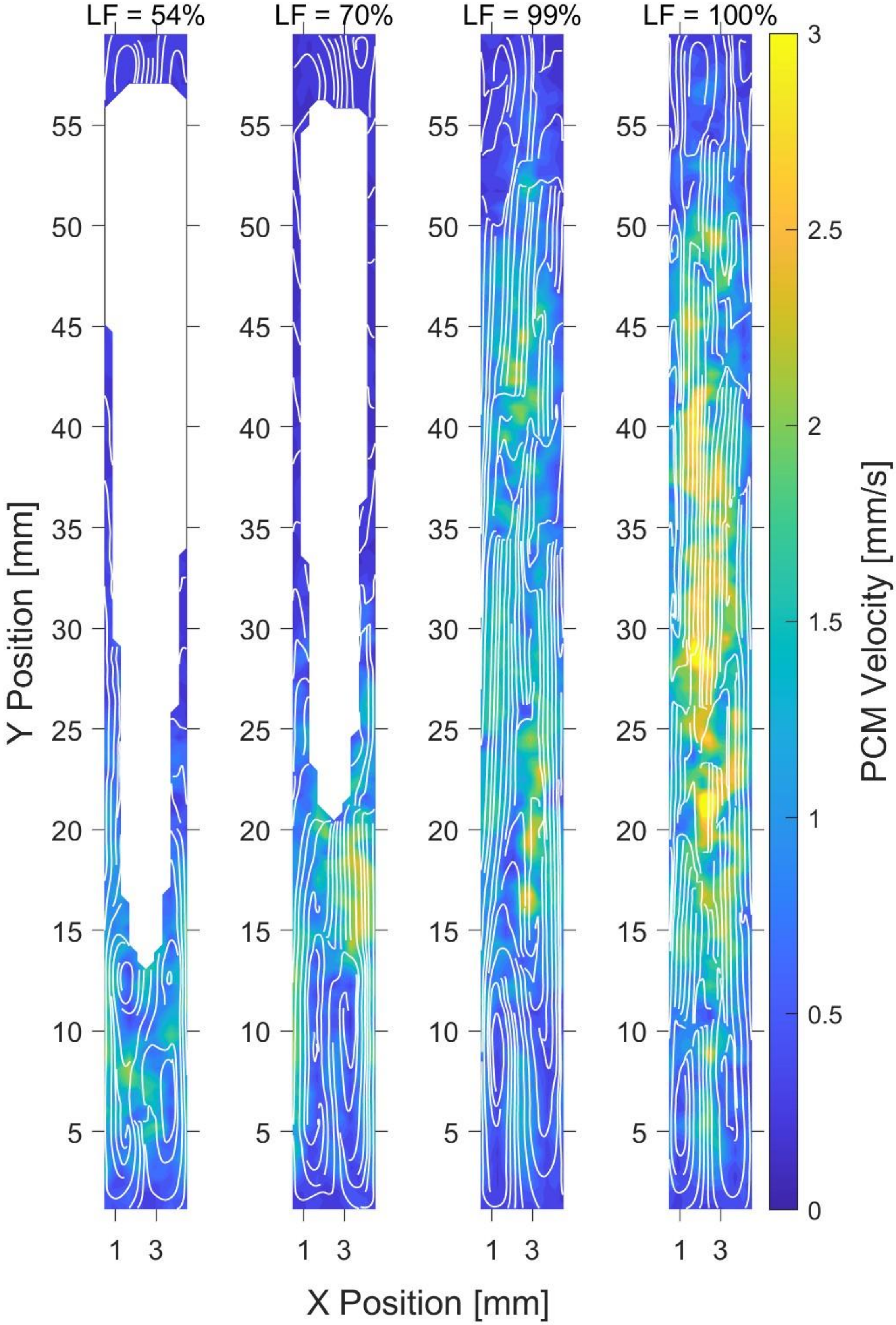

LF = 54%
LF = 70%
LF = 99%
LF = 100%
Y Position [mm]
X Position [mm]
PCM Velocity [mm/s]

(i) 6mm 45C

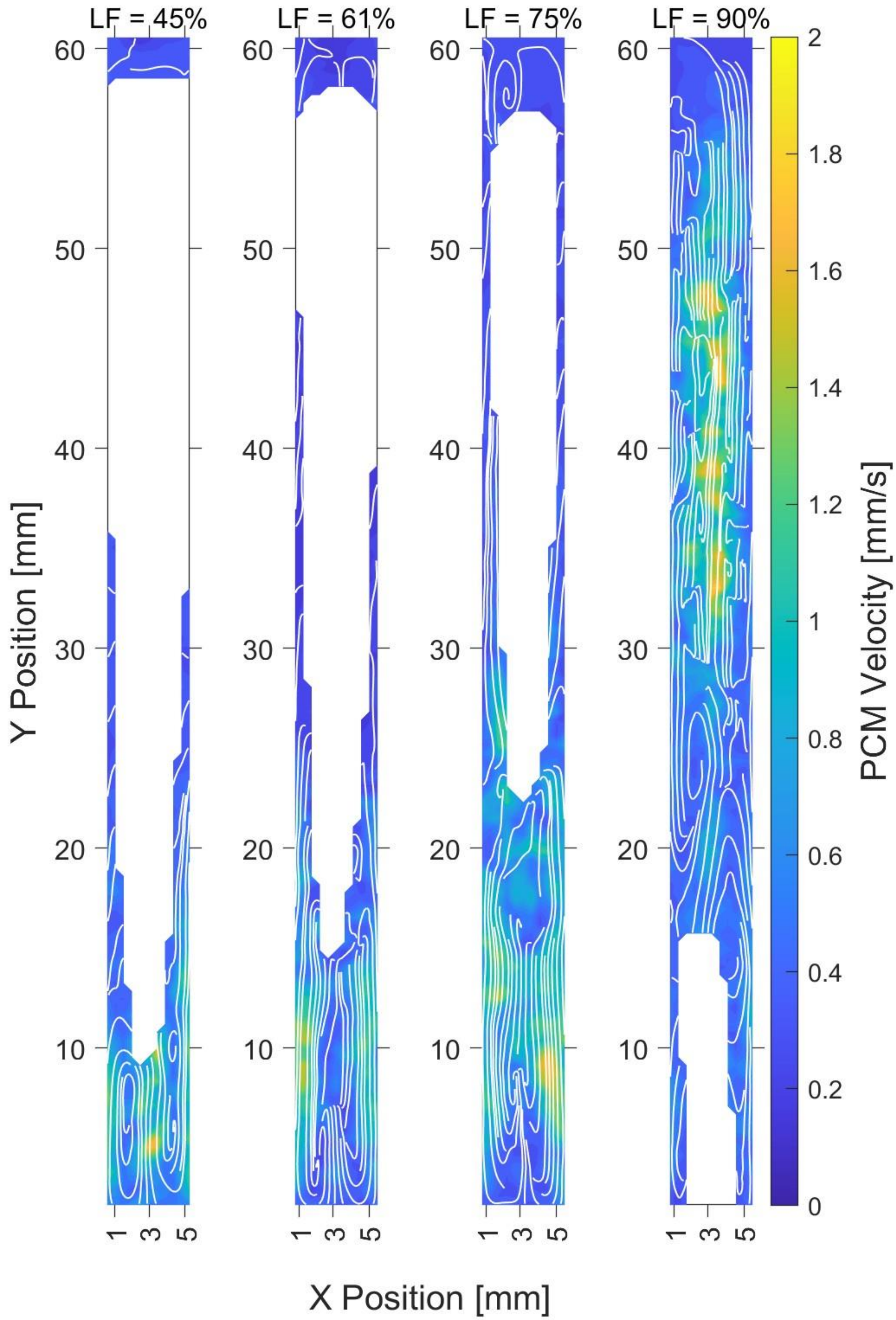
LF = 45%
LF = 61%
LF = 75%
LF = 90%
Y Position [mm]
X Position [mm]
PCM Velocity [mm/s]
60
50
40
30
20
10
1
3
5
2
1.8
1.6
1.4
1.2
1
0.8
0.6
0.4
0.2
0

(j) 6mm 35C

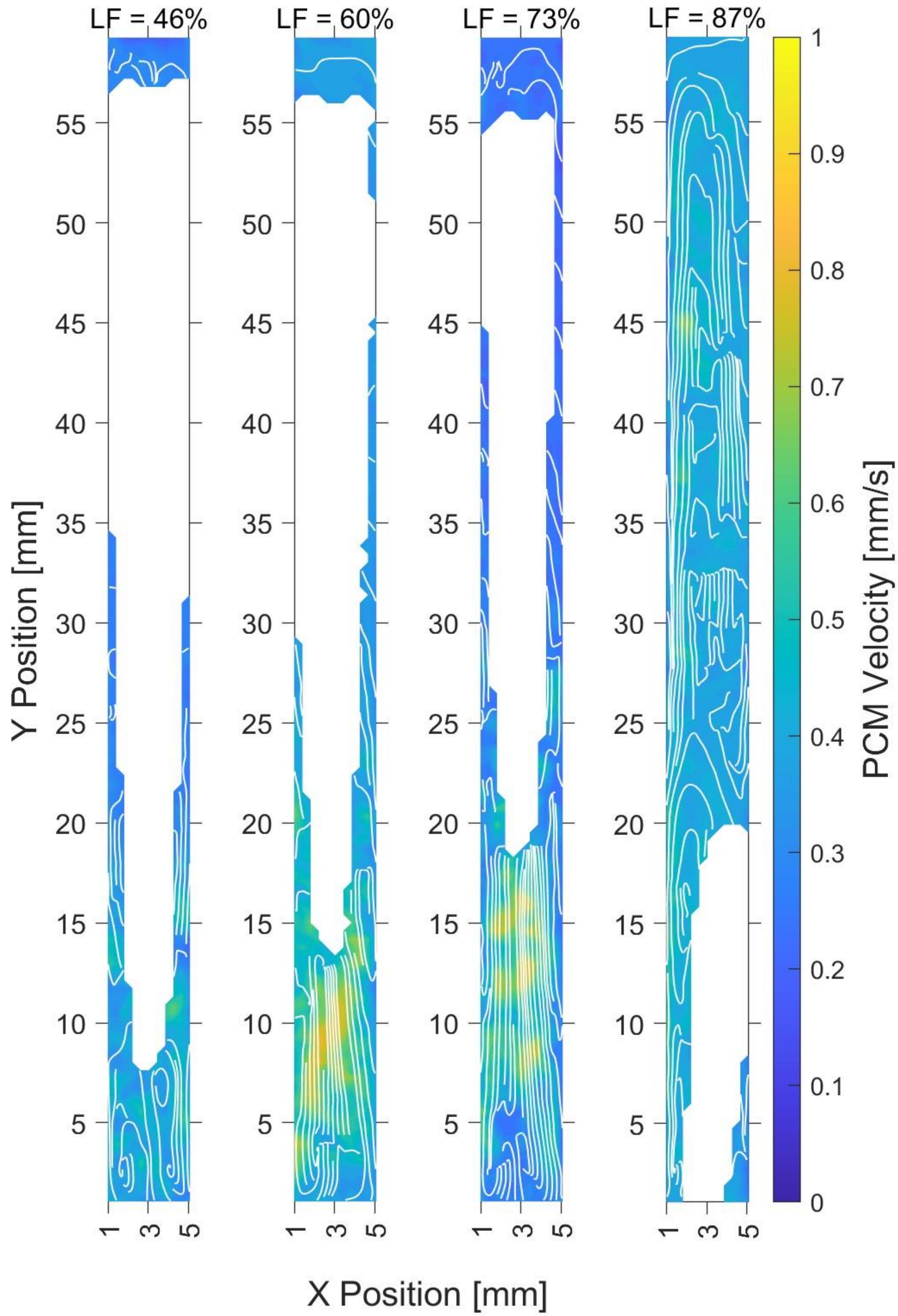

LF = 46%
LF = 60%
LF = 73%
LF = 87%
Y Position [mm]
X Position [mm]
PCM Velocity [mm/s]
55
50
45
40
35
30
25
20
15
10
5
1
3
5
0
0.1
0.2
0.3
0.4
0.5
0.6
0.7
0.8
0.9
1

(k) 6mm 25C

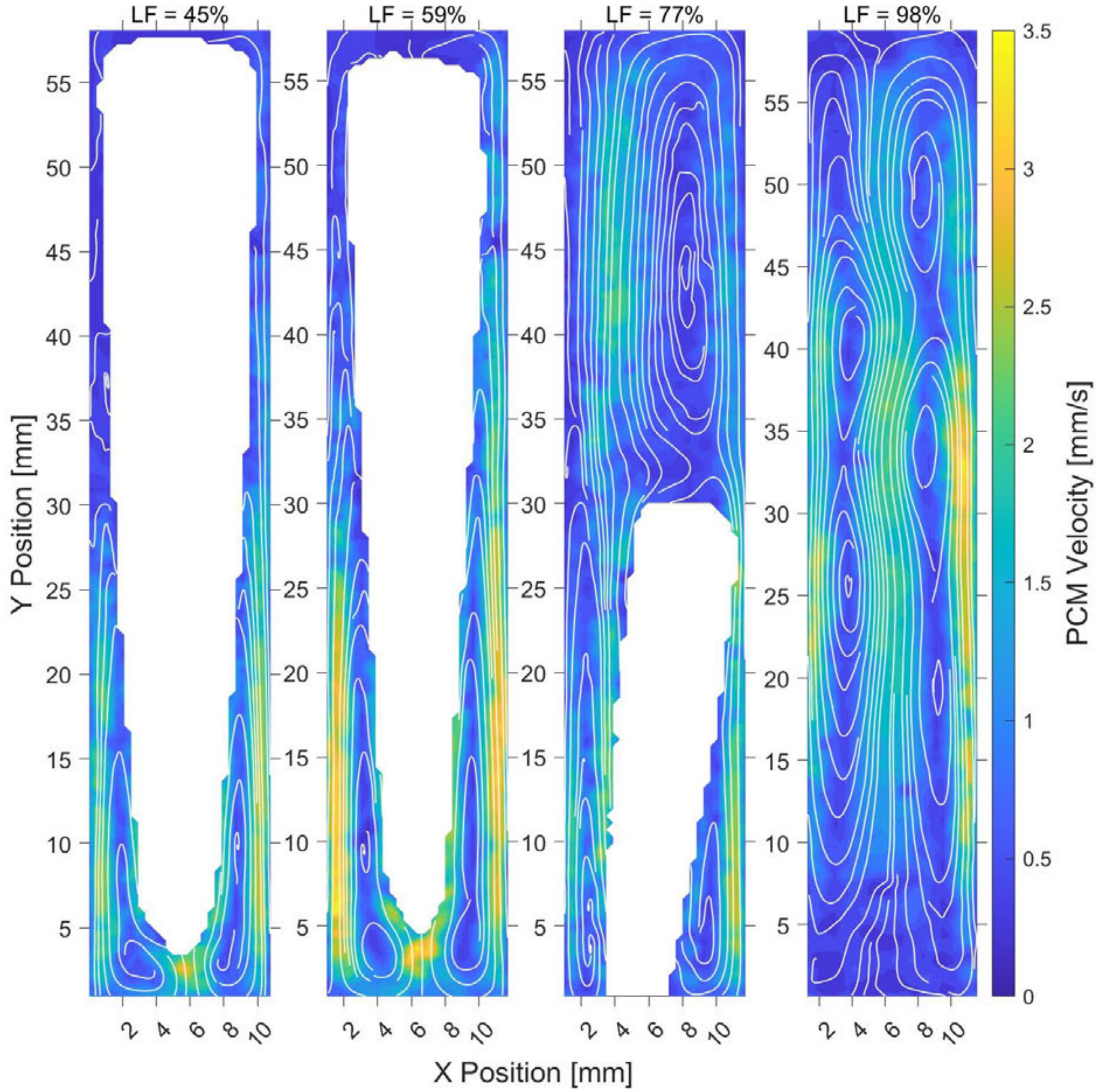

LF = 45%
LF = 59%
LF = 77%
LF = 98%
Y Position [mm]
X Position [mm]
PCM Velocity [mm/s]

(l) 12mm 120W

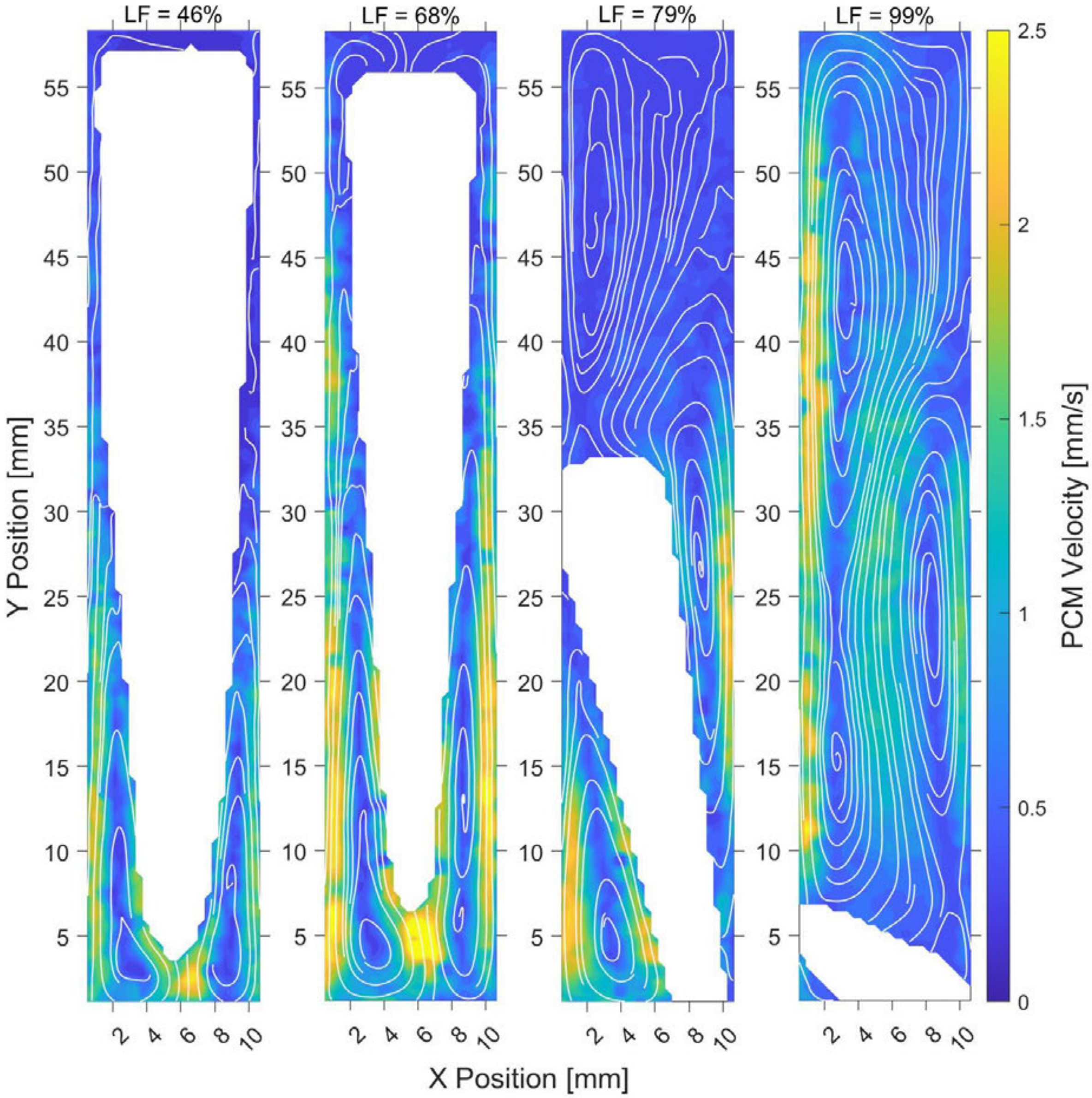
LF = 46%
LF = 68%
LF = 79%
LF = 99%
Y Position [mm]
X Position [mm]
PCM Velocity [mm/s]

(m) 12mm 80W

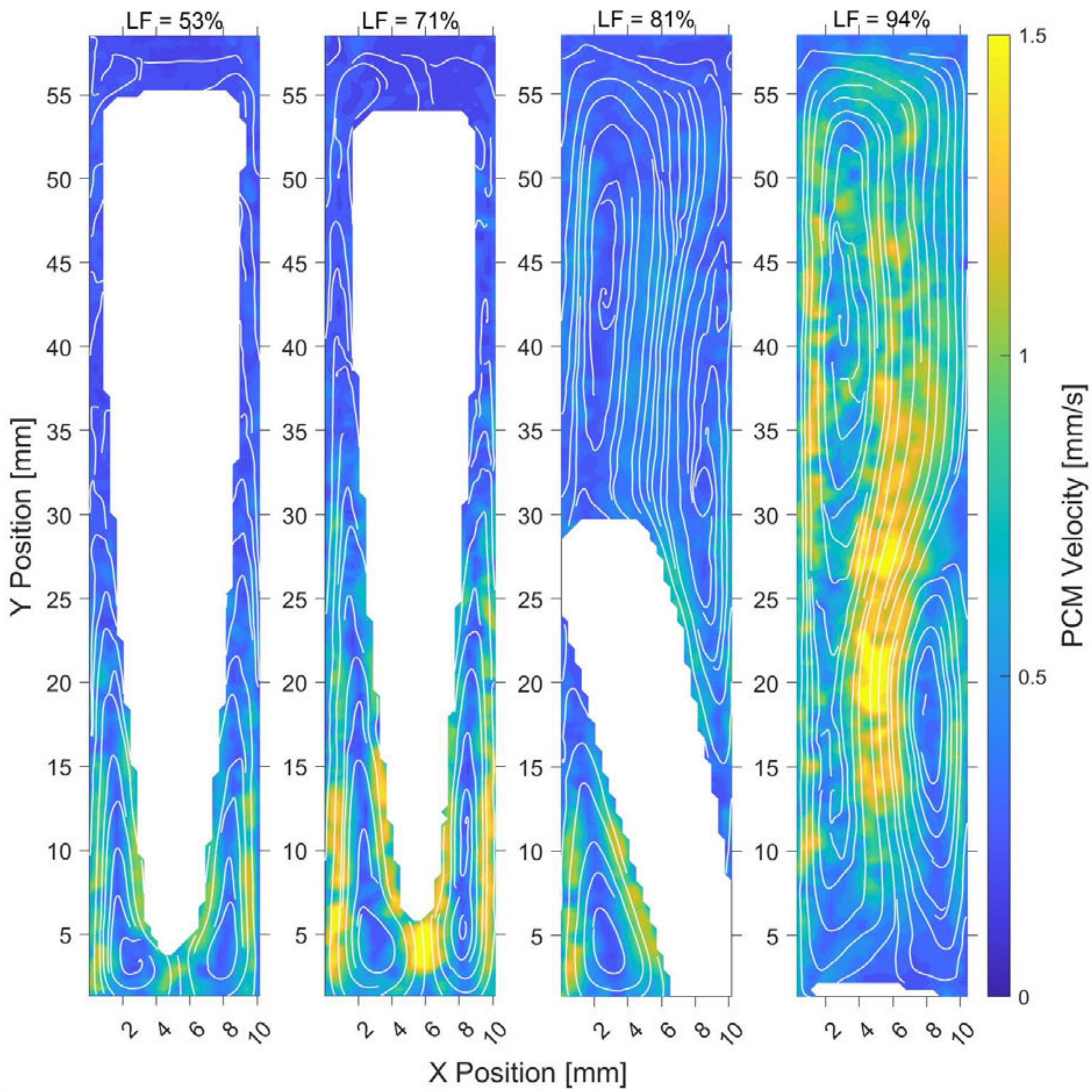
LF = 53%
LF = 71%
LF = 81%
LF = 94%
Y Position [mm]
X Position [mm]
PCM Velocity [mm/s]
1.5
1
0.5
0

(n) 12mm 40W

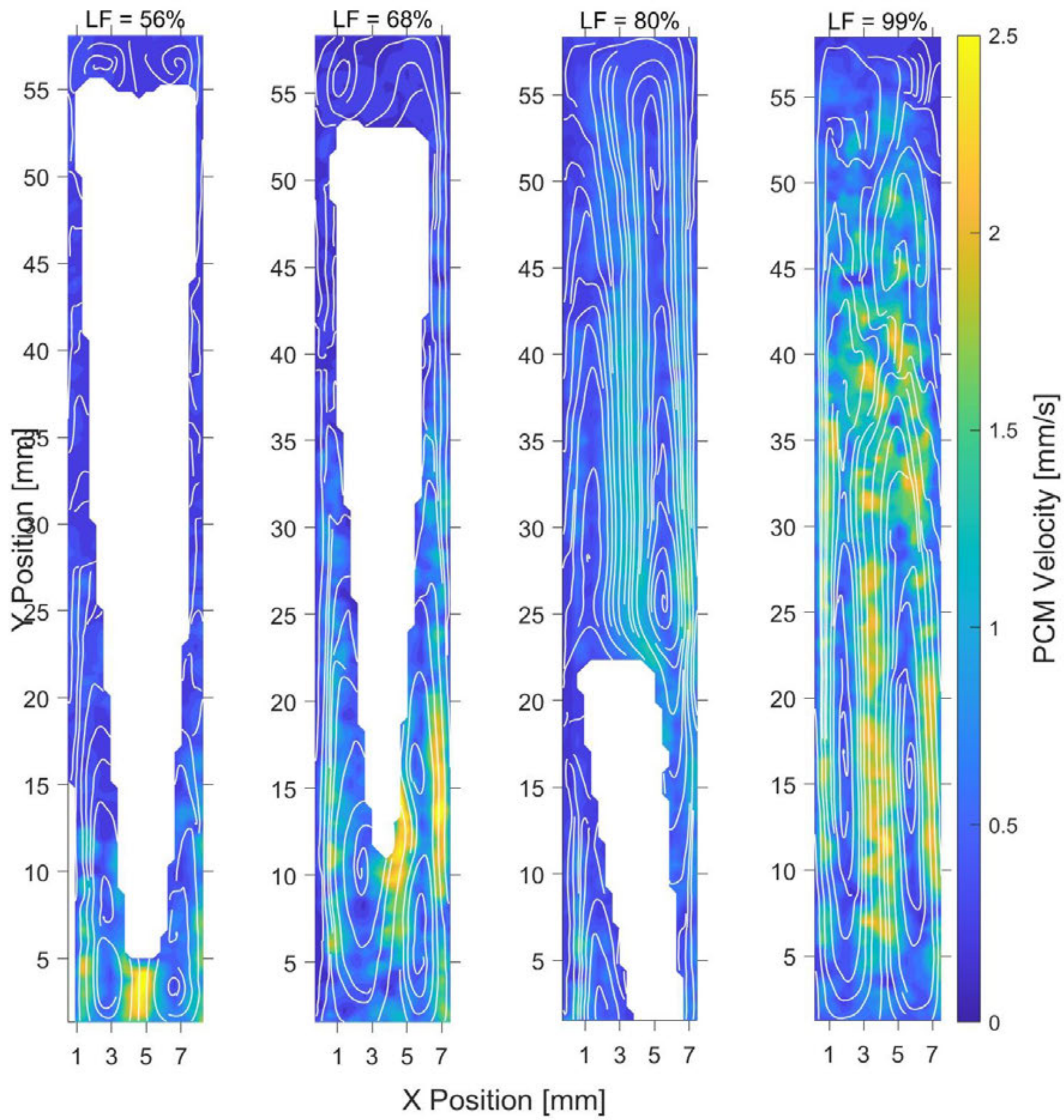
LF = 56%
LF = 68%
LF = 80%
LF = 99%
Y Position [mm]
X Position [mm]
PCM Velocity [mm/s]
55
50
45
40
35
30
25
20
15
10
5
1 3 5 7
0
0.5
1
1.5
2
2.5

(o) 9mm 120W

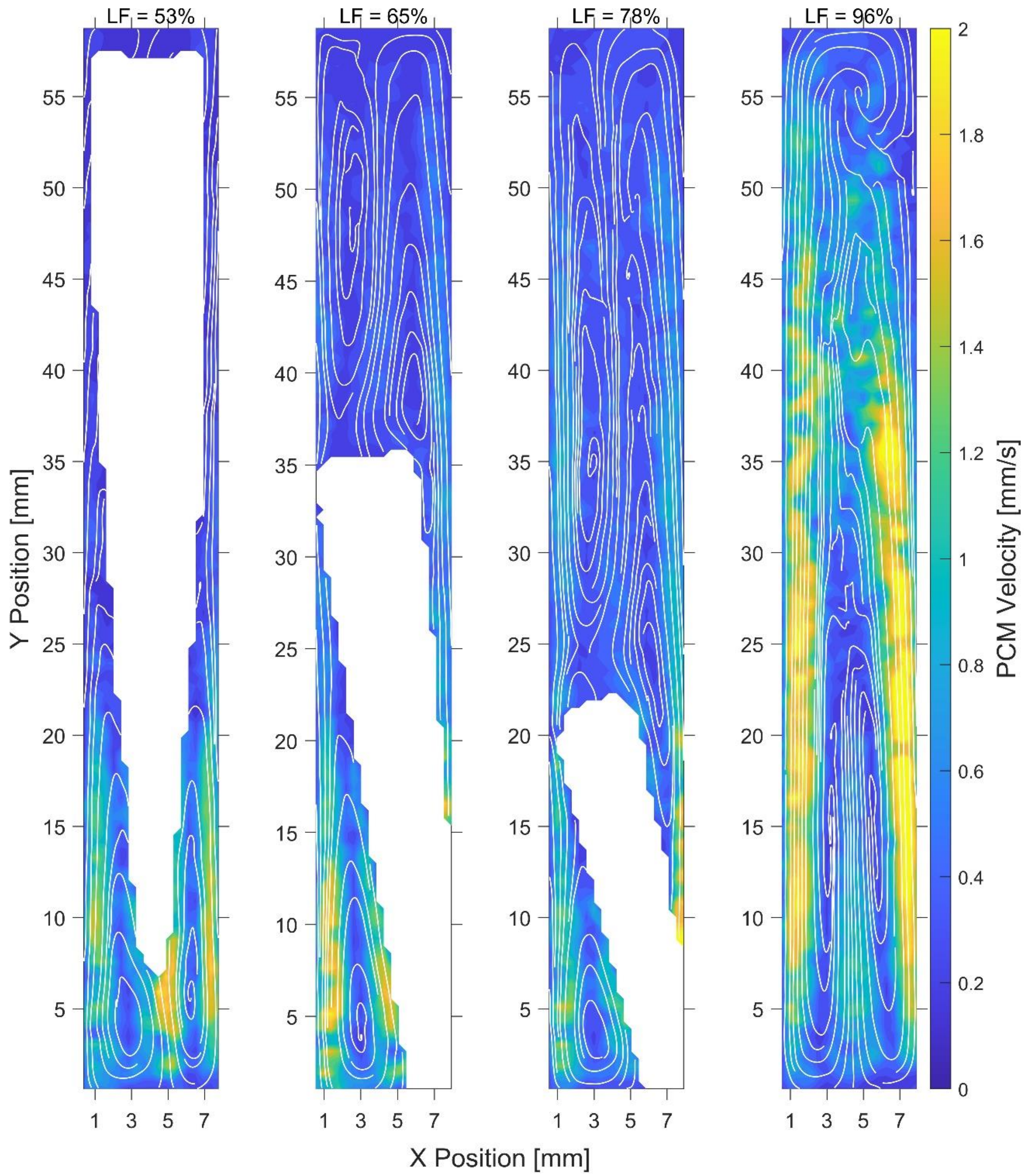

LF = 53%
LF = 65%
LF = 78%
LF = 96%
Y Position [mm]
X Position [mm]
PCM Velocity [mm/s]

(p) 9mm 80W

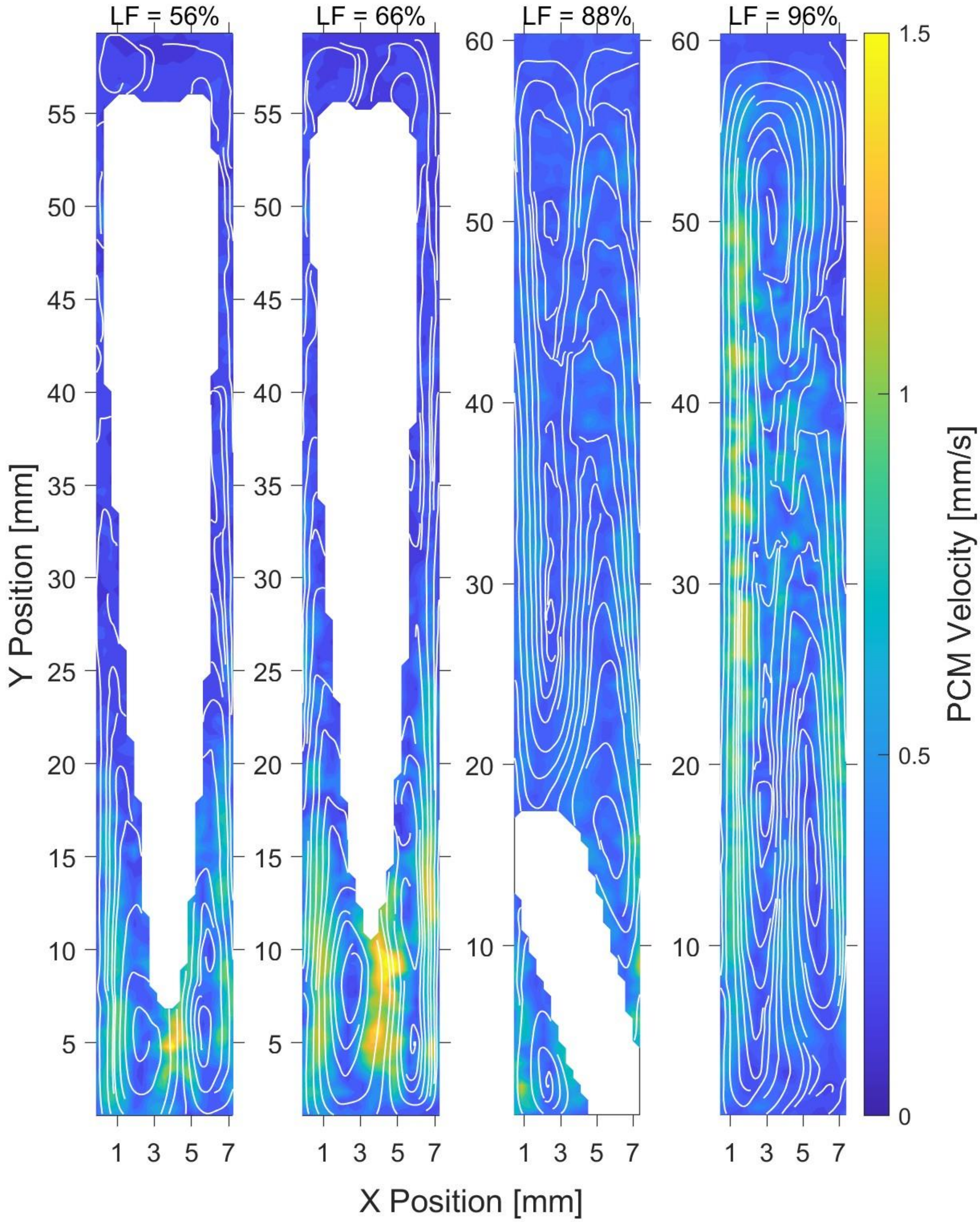

LF = 56%
LF = 66%
LF = 88%
LF = 96%
Y Position [mm]
X Position [mm]
PCM Velocity [mm/s]
0
0.5
1
1.5
5
10
15
20
25
30
35
40
45
50
55
60
1 3 5 7

(q) 9mm 40W

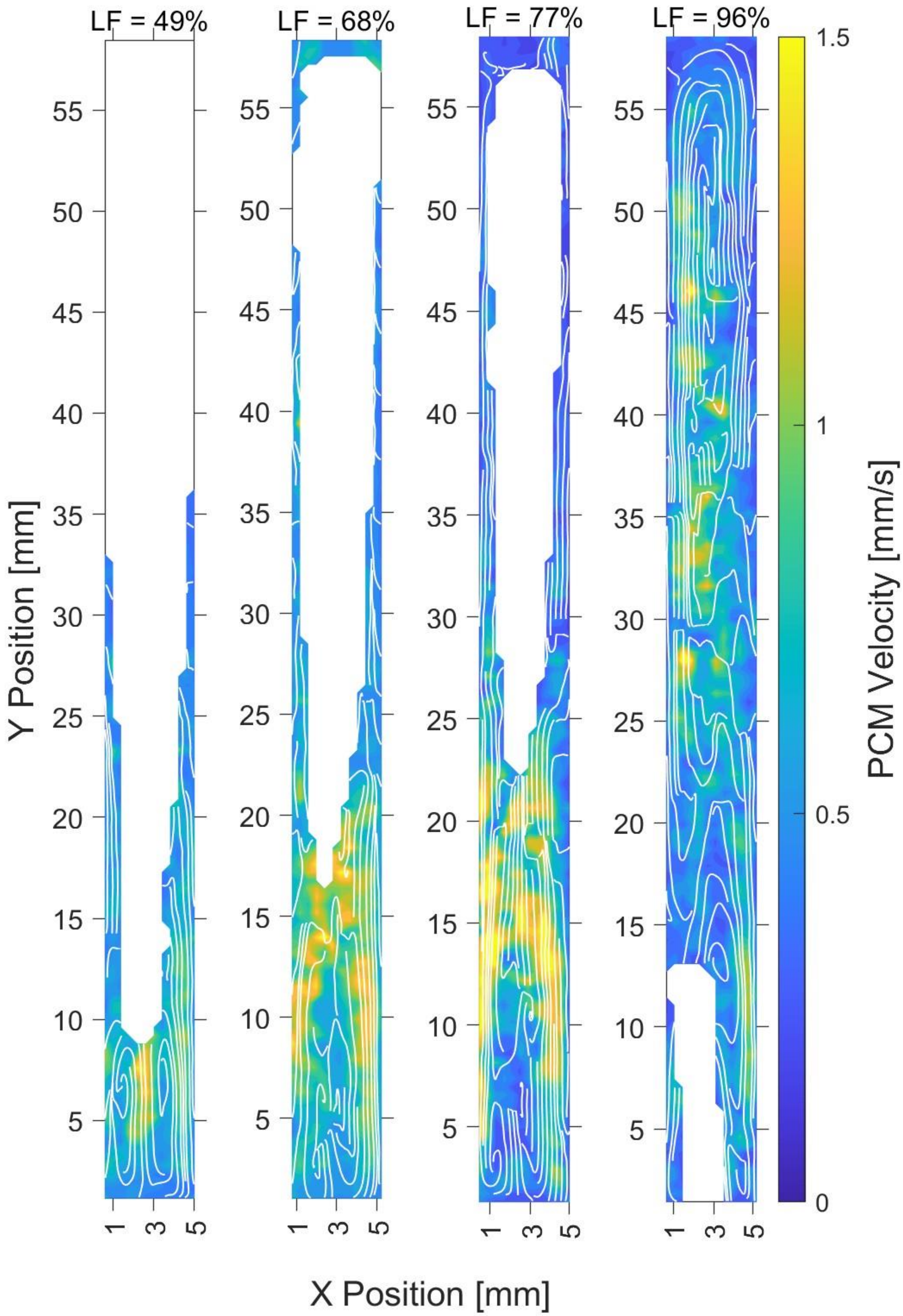
LF = 49%
LF = 68%
LF = 77%
LF = 96%
Y Position [mm]
X Position [mm]
PCM Velocity [mm/s]
1.5
1
0.5
0

(r) 6mm 120W

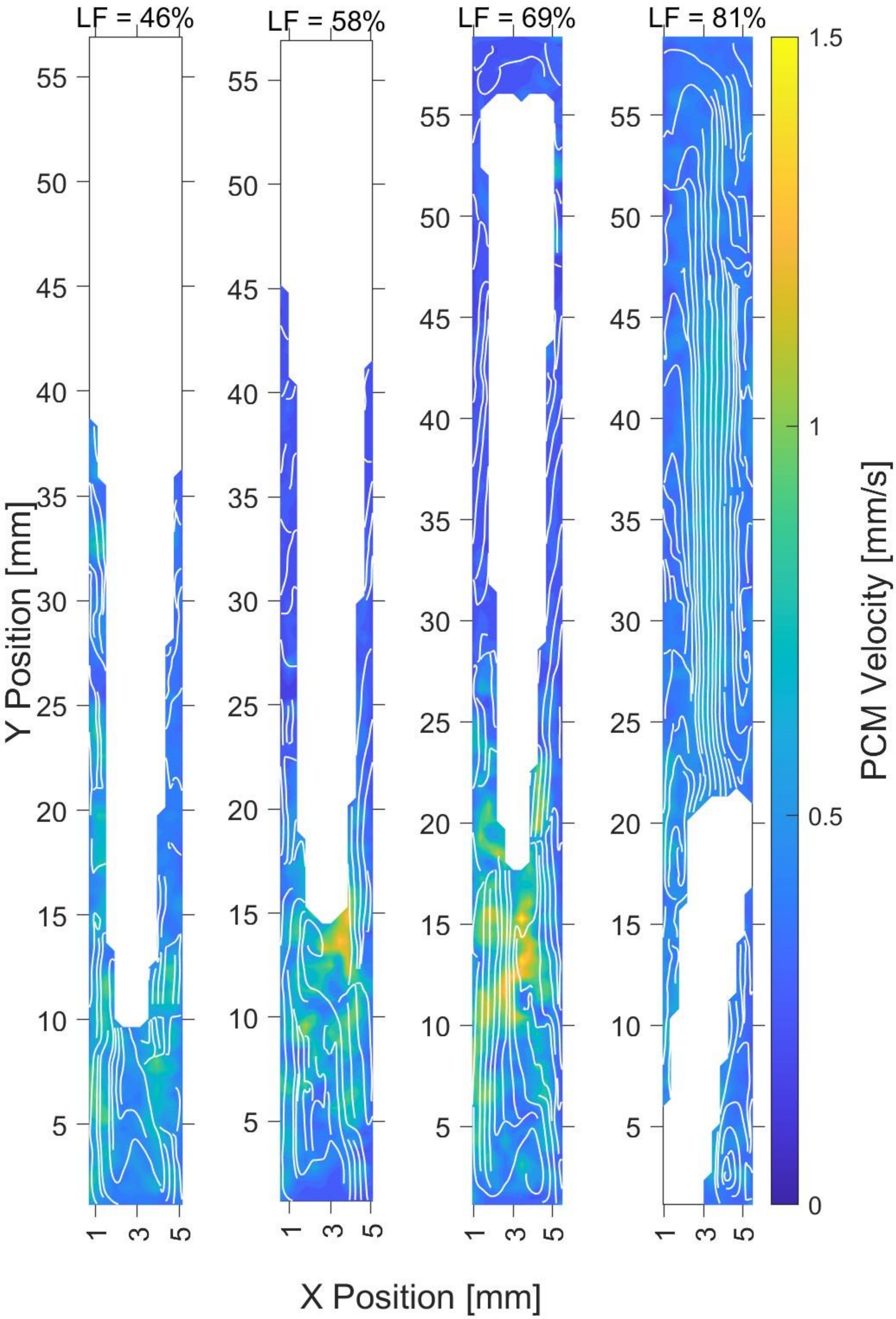

LF = 46%
LF = 58%
LF = 69%
LF = 81%
Y Position [mm]
X Position [mm]
PCM Velocity [mm/s]

(s) 6mm 80W

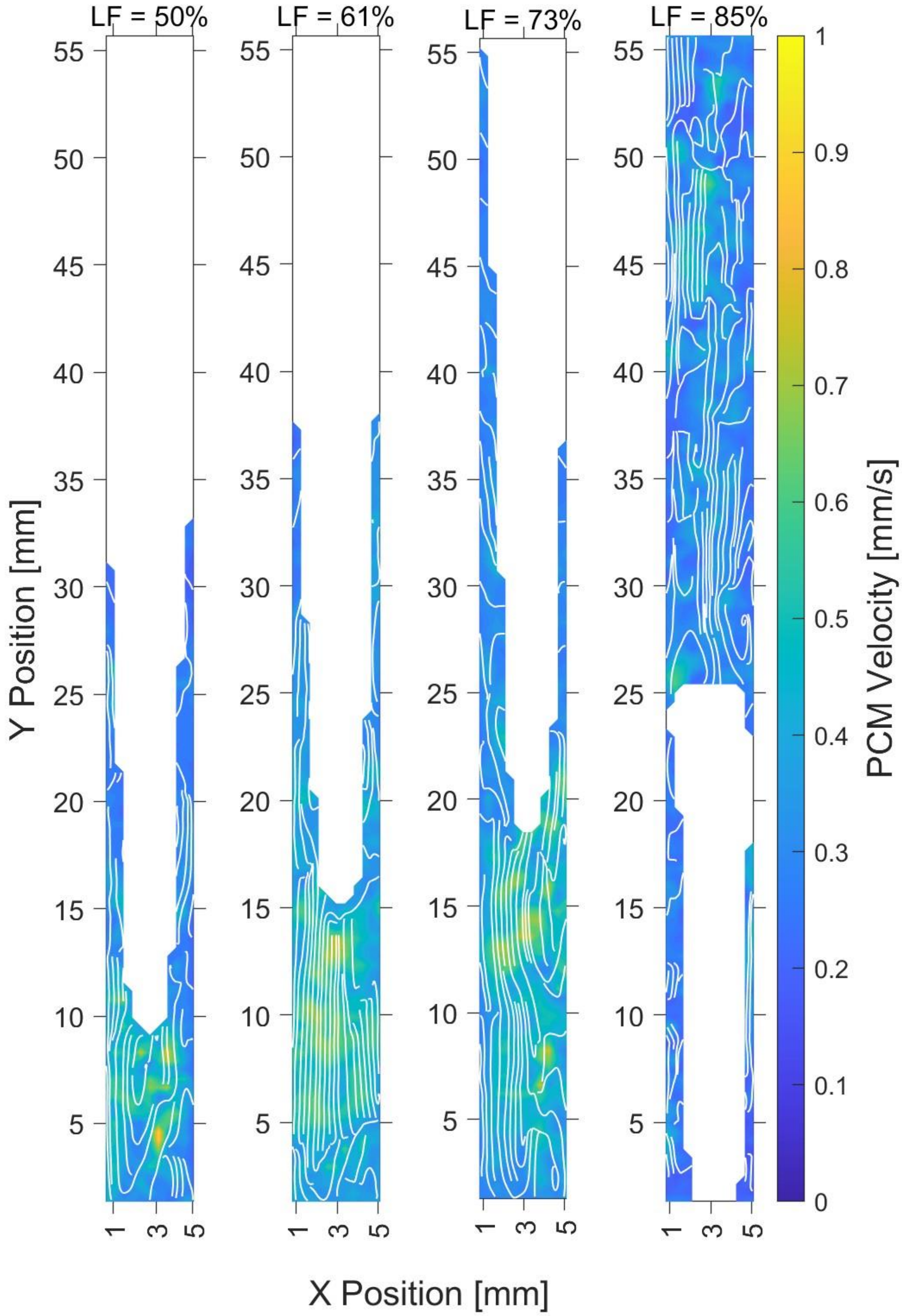

(t) 6mm 40W

Figure 52(t): Local velocity estimates taken with PIV. Note the changing scale in the color bar.